Civil Engineering and Applied Solutions

Research Article

journal homepage: ceas.journals.umz.ac.ir

CEAS Civil Engineering and Applied Solutions

Seismic Hazard Assessment and Building Vulnerability in Qom City

Mahdi Moradi [a*], Mohammad Sadegh Torkaman [b], Seyed Mohammad Reza Hasani [c]

[a] *Department of Civil Engineering, Qo.C., Islamic Azad University, Qom, Iran*
[b] *Faculty of Management and Accounting, Qazvin Branch, Islamic Azad University, Qazvin, Iran*
[c] *Department of Civil Engineering, Faculty of Civil Engineering, Babol Noshirvani University of Technology, Babol, Mazandaran, Iran*

ARTICLE INFO

Keywords:
Seismic hazard
Building vulnerability
Earthquake potential index
Qom city

Article history:
Received 22 December 2025
Accepted 23 April 2026
Available online 01 October 2026

ABSTRACT

Qom city, owing to its location on several active faults, is a sensitive area exposed to seismic hazards. Therefore, damage reduction, crisis management, and enhancement of the city's resilience are essential. The aim of this study is to evaluate Qom's resilience against earthquakes. This objective includes producing practical maps such as seismic soil classification, peak ground acceleration (PGA) for 475 and 2475 year return period earthquakes, and assessing building performance under these seismic scenarios. To this end, soil data from previous studies were collected and analyzed using ArcGIS. PGA values for the 475 and 2475 year return period earthquakes were obtained using OpenQuake software. Finally, the results were compiled using Excel and ArcGIS. The assessments showed that the mean probability of building failure in Qom under earthquakes with 475 and 2475 year return periods is 66.5% and 80.5%, respectively, which is mainly due to the prevalence of masonry buildings lacking adequate lateral load resisting systems. These findings highlight the necessity of retrofitting and renewing deteriorated buildings, improving construction standards, and prioritizing urban resilience enhancement.

1. Introduction

Qom city holds great religious significance as the site of Iran's largest seminary and the shrine of Hazrat Masoumeh, making it the country's second most important pilgrimage city. It also serves as a major transportation corridor connecting the northern, southern, eastern, and western provinces. The population of Qom has increased markedly over the past two decades and currently stands at approximately 1,292,283 people [1]. Seddighi and Seddighi [2], through a statistical review of natural hazards over the past 100 years, reported the frequency of these hazards. According to their analysis, floods, earthquakes, and droughts were the most frequent hazards in Qom, respectively. Among these, earthquakes can be considered one of the most hazardous natural disasters. Qom is located close to several extensive active faults. The principal faults affecting the city include the Indes, Koushk Nosrat, Kashan, and Alborz faults, which confirm the high seismic hazard potential in the region [3]. Most buildings in Qom are old and structurally vulnerable, and past earthquakes have produced extensive damage in the city [4]. In 1386, an earthquake of approximately magnitude 5 on the Richter scale occurred in the town of Kahak, causing public alarm, damage to the Valiasr metro tunnel, and harm to residential units. The event resulted in several fatalities and injuries. Damage to provincial infrastructure and 156 residential units was reported at approximately sixty billion rials [5].

Seismic risk assessment requires accurate data on seismicity, the location and distribution of buildings, and the resident population. In addition, exposure models and the structural characteristics of buildings play a fundamental role in estimating their vulnerability. However, at large scales, particularly in developing countries, such data may not be readily available [6]. Seismic vulnerability of structures is commonly estimated using damage curves that relate ground-motion intensity to the probability of loss [7]. These curves are constructed from parameters such as earthquake peak ground intensity, acceleration, or velocity (PGA/PGV),

* Corresponding author.
E-mail addresses: mahdi.moradi@iau.ac.ir (M. Moradi).

https://doi.org/10.22080/ceas.2026.30879.1068
ISSN: 3092-7749/
How to cite this article: Moradi, M., Torkaman, M., Hasani, S. M. R. Seismic Hazard Assessment and Building Vulnerability in Qom City. Civil Engineering and Applied Solutions. 2026; 2(4): 1–14. doi:10.22080/ceas.2026.30879.1068.

among which, peak ground acceleration (PGA) is more widely used [8]. Fragility curves are also employed to estimate the probability of exceeding specified damage states for buildings based on seismic intensity measures [9]. These curves are typically developed using empirical, analytical, and structural simulation approaches [9]. Empirical methods rely on past damage data and are particularly practical in regions where structural information is limited [10]. Numerous studies have advanced these methodologies, including analytical investigations of industrial structures in Italy [11] and numerical simulations of reinforced-concrete buildings in Turkey [12]. In Iran, despite the occurrence of destructive earthquakes, comprehensive records of damage and associated seismic parameters have often not been documented [7]. Initiatives such as JICA [13] and GEM EMME [14] have sought to improve these assessments. In this context, Fallah Tafti et al. [9] employed an Analytic Hierarchy Process (AHP)–based analytical approach to develop fragility curves for 19 different building typologies in Iran. They combined domestic and international data, using 39 local fragility curves and 481 curves from other countries. This methodology forms the primary basis for the seismic-hazard assessment in the present study.

Few studies have addressed the seismic resilience of Qom city. Kamalian et al. [15] took an important step toward assessing Qom's seismic vulnerability by collecting and analyzing data from 160 boreholes at 60 stations to conduct a detailed soil microzonation study for the city. They also presented a seismic hazard analysis for a 475-year return period and produced a peak ground acceleration (PGA) map for Qom based on those results. It should be noted that these studies were not based on local fault earthquakes and fault behavior, and no study has been conducted to quantify the vulnerability of Qom's buildings. Ghafoori et al. [16] applied an optimization-based probabilistic seismic scenario method to determine the minimum number of scenarios required to estimate urban losses. Using prior seismological and geological data, they evaluated and analyzed seismic hazards, although their work was limited to optimizing a methodology for seismic assessment and did not produce PGA maps or estimates of potential earthquake losses for Qom. Khorasani Zadeh et al. [5] examined Qom's seismic vulnerability based on a scenario for the Alborz fault. They derived fragility curves from the fault's seismic activity and calculated the probability of building failure in Qom accordingly. Their results indicated that the northeastern blocks and the southern Qomrud area sustain the greatest damage, with an estimated complete collapse of about 25%. However, this study was confined to only one of the multiple faults surrounding Qom. Therefore, more comprehensive studies that account for the effects of all faults around Qom appear necessary. Vaseghi et al. [17] investigated the seismic resilience of Districts 3 and 4 in Qom, using the Analytic Hierarchy Process (AHP) to weight resilience indicators. Their study showed that District 3 exhibits high vulnerability due to factors such as narrow passages, weak urban infrastructure, and low occupant awareness of building safety, whereas District 4 demonstrated better resilience indicators. Shirvani Harandi et al. [18] assessed the physical and social vulnerability of District 4 of Qom County under a 475 year return period earthquake scenario, employing the PGA values reported by Kamalian et al. [15]. Their results indicated that the northern half of District 4 is more vulnerable owing to higher building density, poorer construction quality, larger population, and narrower streets, while the southern half, characterized by newer buildings, lower density, and wider streets, would experience fewer losses and casualties. It should be noted that these studies do not cover the entire city of Qom, addressing only one of its seven districts, and the PGA used was based on Kamalian et al. [15]. Previous geotechnical studies of Qom and its soil classification were based on the work of Kamalian et al. [15]. Maghami et al. [19] demonstrated that earlier velocity measurements had errors of approximately 10-15%, with the $\bar{V}_{S30}$ velocity being overestimated in deeper deposits. Maghami et al. [19] presented a shear-wave velocity distribution map to bedrock in their study. However, a dedicated $\bar{V}_{S30}$ map and soil classification for Qom, which are crucial for seismic analysis, were not provided in their research.

Recognizing significant data gaps in Qom's seismic assessment, this research introduces a novel integrated framework. The study begins by introducing the Earthquake Potential Index (EPI) for Qom, followed by the development of a new explicit $\bar{V}_{S30}$ map and soil classification for the city derived to correct known overestimations in prior literature. Subsequently, the analysis proceeds to compute site-specific Peak Ground Acceleration (PGA) for critical return periods (475 and 2475 years). Finally, by employing regionally calibrated fragility curves for 19 Iranian building types, the percentage probability of building failure in Qom is produced and subjected to statistical analysis.

2. Earthquake potential index (EPI)

Earthquakes are inherently unpredictable and may occur without significant prior warning. The likelihood of an earthquake depends on multiple factors, including proximity to tectonic plate boundaries, historical seismic activity, the nature of existing geological formations, and others. To assess the seismicity of a region and to enable comparison of the resulting values, it is necessary to employ a model that proportionally accounts for the influence of each factor and defines an index accordingly. Ahmad et al. [20], aiming to identify key factors in spatial data analysis through Geographic Information Systems (GIS), introduced a method for determining the Earthquake Potential Index (EPI). Their approach consists of the following steps.

- Selection of variables influencing earthquake occurrence
- Generation of information layers within the GIS environment
- Numerical weighting of variables
- Integration of layers
- Calculation of the Earthquake Potential Index
- Zonation of the region based on earthquake potential

- Preparation of a seismic hazard map

For determining the EPI of Qom Province, the effects of influential factors within a radius of 150 km from the city center were considered. Fig. 1 illustrates the faults located within this 150 km radius relative to the center of Qom. Additionally, the seismic moment magnitudes of historical earthquakes around Qom were obtained from the Institute of Geophysics, University of Tehran [21]. These data are presented in Fig. 2.

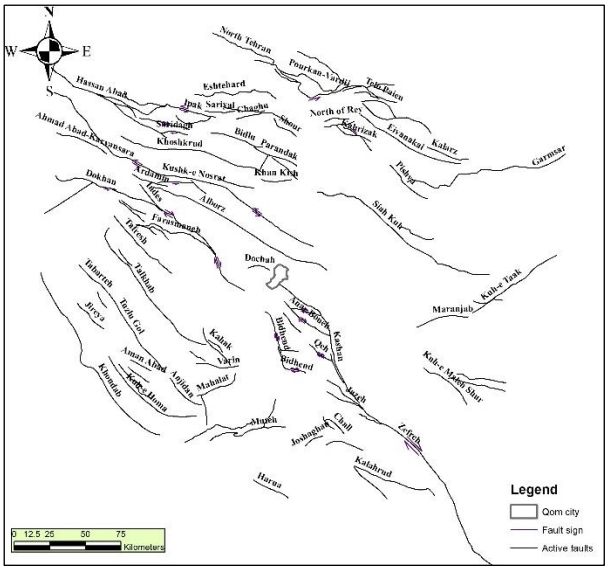

Fig. 1. Faults within a 150 km radius around Qom (adapted from the findings of Mirzaei et al. [21]).

The principal variables of the model proposed by Ahmad et al. [20] include the Digital Elevation Model (DEM), slope angle in degrees (SLOP), density of active faults (Den_F), earthquake epicenter density map (Den_{Ev}), earthquake magnitude in the region (M_L), distance from the city center to active faults (Dis_F), and distance from the city center to earthquake epicenters (Dis_{epi_ev}). For the preparation of the digital model, a map of Iran with 30-meter resolution was employed, while fault data and the earthquake catalog of the region were obtained from the Geophysics Center of the University of Tehran [21]. Ultimately, based on Eq. 1, the Earthquake Potential Index (EPI) map was generated, as illustrated in Fig. 3.

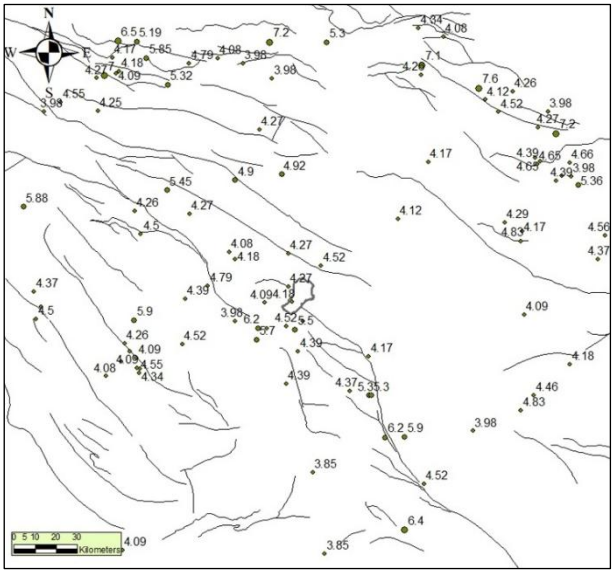

Fig. 2. Moment magnitude of earthquakes around the city of Qom (adapted from the findings of Mirzaei et al. [21]).

$$EPI = 0.1DEM + 0.1Slop + 0.15Den_F + 0.2M_L + 0.15Dis_{epi\_ev} + 0.15Den_{Ev} + 0.15Dis_F \quad (1)$$

In Fig. 3, the EPI index map is depicted within a 150 km radius around Qom. According to this map, the city of Qom exhibits high seismicity and is among the most seismically active areas within the delineated region. With an EPI index of 3.5, Qom requires special consideration in seismic design of buildings. This issue has also been addressed in Standard 2800 [22], which classifies Qom as a high-seismicity zone. It is noteworthy that the absence of a historical record of major earthquakes in Qom has somewhat reduced attention to this matter. Nevertheless, the high density of faults in this area indicates significant earthquake hazard potential. The lack of a major historical earthquake, in fact, serves as a warning signal, suggesting the accumulation of seismic energy in this region.

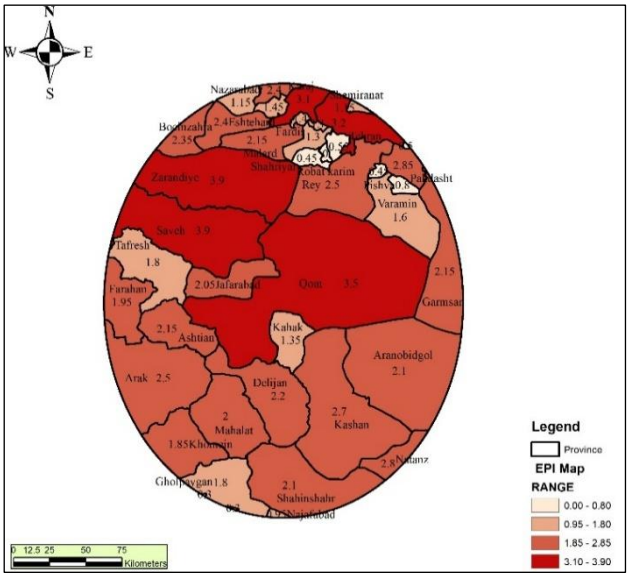

Fig. 3. Earthquake Potential Index (EPI) map of Qom Province.

3. Geology and geotechnical engineering in the city of Qom

Buildings in Iran are designed against earthquakes in accordance with Standard 2800 [22]. According to this standard, soils are classified based on the average shear-wave velocity to a depth of 30 meters ($\bar{V}_{S30}$). The standard divides soils into four types. Type I with shear-wave velocity greater than 750 m/s (most suitable for construction), Type II with shear-wave velocity between 375 and 750 m/s (moderate quality), Type III with shear-wave velocity between 175 and 375 m/s (medium density), and Type IV with shear-wave velocity less than 175 m/s (weak and requiring improvement).

In 2002, Ramazi [23] conducted a seismic hazard zoning study of Qom Province. He estimated the peak horizontal acceleration of bedrock without considering soil types, based on the tectonics and seismicity of Qom Province, using Cornell's approach. His findings indicated that the seismicity of Qom is influenced not only by the major known faults between Tehran and Kashan but also by smaller, yet active or potentially active faults beneath the city itself. As a significant step toward assessing the seismic vulnerability of Qom, Kamalian et al. [15] carried out a microzonation study of Qom soils by analyzing data from 160 boreholes across 60 stations. They also performed seismic hazard analysis for a return period of 475 years and presented a map of peak ground acceleration across the city. To complement these results, Maghami et al. [19] constructed a three-dimensional model of the Qom sedimentary basin based on shear-wave velocity using Refraction Microtremor (ReMi) surveys. Their findings revealed new evidence of several potential faults, including the Qomrud Fault. Moreover, the analyses showed that for relatively shallow bedrock, previously obtained velocities had errors of about 10–15%, while in deeper sediments, $\bar{V}_{S30}$ values were overestimated [19]. However, most existing geotechnical reports prepared by local companies in Qom are limited to shallow depths (generally less than 30 meters) and rely on descriptive methods rather than direct use of $\bar{V}_{S30}$ [19].

Maghami et al. [19] presented shear-wave velocity distribution profiles down to bedrock in their study (Fig. 4). However, neither the $\bar{V}_{S30}$ map nor the soil classification of Qom based on it was provided. Accordingly, the results of Maghami et al. [19] were utilized to prepare a map of average shear-wave velocity to a depth of 30 meters for Qom soils ($\bar{V}_{S30}$), which is shown in Fig. 5. This map indicates that most urban areas fall within soil Types II and III, while some zones even belong to Type IV, reflecting the seismic weakness of Qom soils. A comparison of these results with the study of Kamalian et al. [15] suggests that earlier investigations may have overestimated soil conditions.

4. Seismic hazard assessment and zoning of Qom

In this study, the OpenQuake software was employed for seismic hazard assessment and zoning of the city of Qom. OpenQuake is an open-source software designed for earthquake hazard evaluation. It has been developed by the Global Earthquake Model (GEM) Foundation. The software is widely used for conducting seismic analyses and assessing earthquake hazards. Acting as a comprehensive tool, OpenQuake provides capabilities for Probabilistic Seismic Hazard Analysis (PSHA), Deterministic Seismic Hazard Analysis (DSHA), and overall seismic hazard evaluation [11].

To initiate the process, OpenQuake relies on a set of input data. These data include identification of seismic sources, earthquake Ground-Motion Prediction Equations (GMPEs), target points for output results, the type of response of interest (peak ground acceleration (PGA), spectral acceleration (SA) for different probabilities), and average shear-wave velocity at 30 m depth ($\bar{V}_{s30}$), and selection of Ground Motion Prediction Equations (GMPEs) to define ground motion hazard. Seismic hazard analysis and earthquake zoning with this software involve four stages. These stages include identification of seismic sources, determination of the controlling earthquake (the largest probable earthquake for each source), selection of an appropriate GMPE for strong ground motion, and calculation of strong ground-motion parameters and seismic hazard estimation [24].

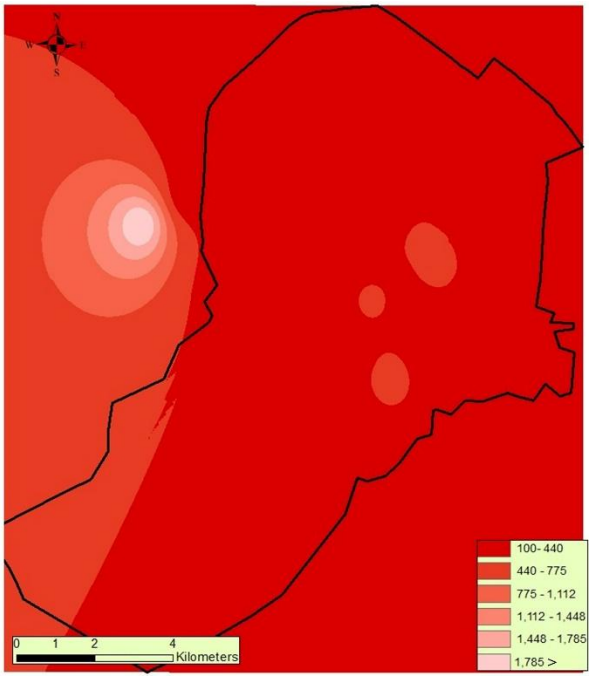

Fig. 4. $\overline{V}_{S30}$ in the soils of Qom (in meters per second) (adapted from the study of Maghami et al. [19]).

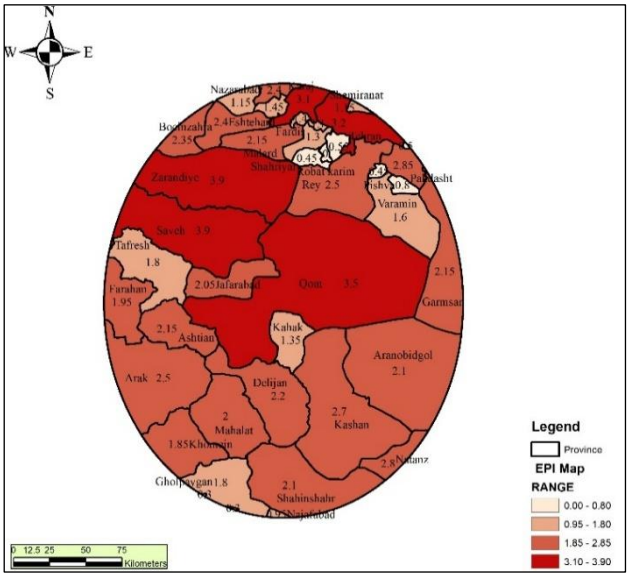

Fig. 5. Oil classification map of Qom province.

In this study, faults affecting the city of Qom within a radius of 100 km from the city center were considered. Information on these faults (including geographic location, length, moment magnitude scale, orientation, and type) was obtained from the Geophysics Institute of the University of Tehran [21]. The moment magnitude (M_w) of these faults was estimated using Eqs. 2-4, based on subsurface rupture length. In these equations, (L) and (M_w) represent the subsurface rupture length (in kilometers) and the moment magnitude of the fault, respectively. Eq. 2 applies to strike-slip faults, Eq. 3 to reverse faults, and Eq. 4 to normal faults [25].

$$M_w = 4.33 + 1.49Log(L) \quad (2)$$

$$M_w = 4.49 + 1.49Log(L) \quad (3)$$

$$M_w = 4.34 + 1.54Log(L) \quad (4)$$

The faults influencing Qom within a 100 km radius, along with their calculated (M_w) values, are compiled in Table 1. It should be noted that for unspecified fault types, Eq. 3 was applied.

Table 1. Faults affecting the city of Qom within a 100 km radius.

Fault Name	Fault Type	Wells–Coppersmith [25] Relation Eqs. 2-4	Distance to Qom City Center (km)	Fault Length (km)
Kashan	Approximate / Concealed / Inferred	6.86	3.93	39.01
Dochah	Reverse or Thrust Fault	6.32	7.52	16.79
Alborz	Reverse or Thrust Fault	7.67	15.53	136.77
Anar Boneh	Left-lateral Strike-slip	6.90	17.59	41.36
Mehrabad	Reverse and Right-lateral Fault	6.49	24.49	21.91
Indes	Reverse and Right-lateral Fault	7.53	25.63	109.36
Myam	Unspecified	6.37	26.18	18.38
Bidehend	Right-lateral Fault	6.73	26.40	31.68
Kushk Nosrat	Reverse and Left-lateral Fault	7.82	29.12	221.01
Kashan	Reverse or Thrust Fault	7.26	38.05	71.78
Farasmaneh	Reverse or Thrust Fault	7.18	47.24	64.06
Bidehand	Reverse and Right-lateral Fault	6.72	49.42	31.38
Rahagh	Unspecified	6.14	51.28	12.72
Gheh	Right-lateral Fault	6.44	52.43	20.26
Khoreh	Reverse or Thrust Fault	6.77	64.07	33.77
Kahak	Reverse or Thrust Fault	6.18	64.30	13.68
Zard Rang	Unspecified	6.61	64.35	26.45
Siah Kouh	Reverse or Thrust Fault	7.69	65.14	140.91
Ravand	Unspecified	6.50	65.78	22.42
Khan Kish	Unspecified	6.49	66.48	21.83
Varin	Reverse or Thrust Fault	6.69	68.80	29.95
Nazarabad	Approximate / Concealed / Inferred	6.53	69.39	23.50
Talkhab	Reverse or Thrust Fault	7.56	69.87	114.23
Khoshk Rud	Approximate / Concealed / Inferred	7.33	73.46	80.26
Mahallat	Unspecified	6.76	74.46	33.60
Tafresh	Reverse or Thrust Fault	7.12	74.87	58.00
Payvand	Unspecified	6.14	75.24	12.81
Ghermez Aghash	Right-lateral Fault	6.21	77.14	14.17
Sang Khorideh	Reverse or Thrust Fault	6.16	78.43	13.12
Parandak	Approximate / Concealed / Inferred	6.77	78.53	33.80
Jaze	Reverse or Thrust Fault	6.73	80.35	31.83
Zorjin	Reverse or Thrust Fault	6.36	81.38	17.90
Goujar	Unspecified	6.66	87.74	28.66
Nashveh	Reverse and Left-lateral Fault	6.62	88.57	26.72
Azdin	Reverse or Thrust Fault	6.27	90.51	15.58
Bidlou	Unspecified	6.85	91.43	38.13
Dozdeh Emam	Reverse or Thrust Fault	6.62	91.49	27.00
Nobaran	Approximate / Concealed / Inferred	6.88	92.94	40.43
Shour	Unspecified	6.46	99.25	21.11

A crucial element in seismic hazard evaluation is the selection of appropriate ground-motion prediction equations (GMPEs), which model the variation in peak ground motion (such as acceleration) based on magnitude and distance. To address the epistemic uncertainty associated with using a single GMPE, this study employs a logic tree approach incorporating three widely used horizontal ground-motion models supported in OpenQuake [26-28]. The Campbell and Bozorgnia [26] model is a comprehensive NGA-West2 equation with high sensitivity to site conditions and near-fault effects, making it suitable for shallow crustal earthquakes like those in Qom. The Chiou and Youngs [27] model complements it by emphasizing near-fault behavior and soil-dependent amplification, improving accuracy in areas with soft soils. The Akkar and Bommer [28] model, developed from European and Middle Eastern data, provides a more regionally appropriate representation of seismic behavior in Iran, offering a better fit for the local tectonic regime compared to North American models. This combination ensures robust coverage of key physical phenomena and regional applicability, while the weighting reflects the relative confidence in each model's performance for the study area. The GMPEs were weighted as 40, 30, and 30% for Campbell and Bozorgnia [26], Chiou and Youngs [27], and Akkar and Bommer [28],

respectively. This weighting reflects their relative reliability and applicability to the regional seismic context. This weighting scheme adheres to standard PSHA practices and enhances the robustness of the hazard assessment.

In probabilistic seismic hazard assessment (PSHA), analyses are conducted based on all possible scenarios of earthquake magnitudes from seismic sources within the study area and across all possible distances from the site under investigation. In this research, the latest version of the OpenQuake software was utilized. The objective of this type of analysis is to evaluate the probability that an intensity measure type (IMT) will exceed a specified intensity measure level (IML). The software inputs are defined in such a way that they encompass all possible rupture scenarios for the identified sources. The principal equation used in OpenQuake is expressed as follows (Eq. 5).

$$Prob(IMT \geq IML|site.Forecast) = 1 - \prod_{i=1}^{I}(1 - \sum_{n=1}^{N(i)} Prob(IMT \geq IML|site.Rup_{n.i})Prob(Rup_{n.i}) \quad (5)$$

The Forecast module of the software computes earthquake rupture predictions. In this approach, probabilities are directly incorporated, unlike earlier methods that relied on the summation of average annual rates. As shown in Fig. 6, the study area was discretized into 1296 grid points (36×36) with a 0.5 km spacing to enable probabilistic modeling of seismic hazard using OpenQuake, allowing for a more accurate spatial representation of ground motion across the region. The soil classification results from previous sections were assigned to these grid points. The OpenQuake software was then executed based on the defined settings to calculate peak ground acceleration (PGA) for return periods of 475 years (10% probability of exceedance in 50 years) and 2475 years (2% probability of exceedance in 50 years). Fig. 7 presents the output of this software for the 475-year PGA. Based on these results, seismic hazard zoning maps were generated. To enhance visualization, these maps for Qom's buildings were prepared using ArcGIS and are presented in Figs. 8 and 9. According to these maps, the eastern and northern parts of Qom are more strongly affected by seismic activity.

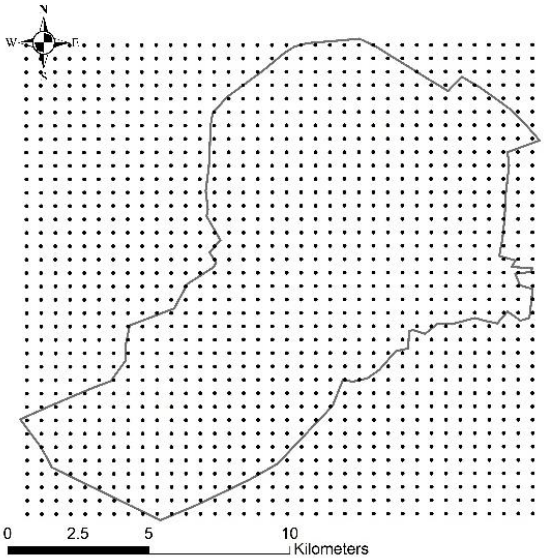

Fig. 6. Spatial discretization of the study area for OpenQuake modelling.

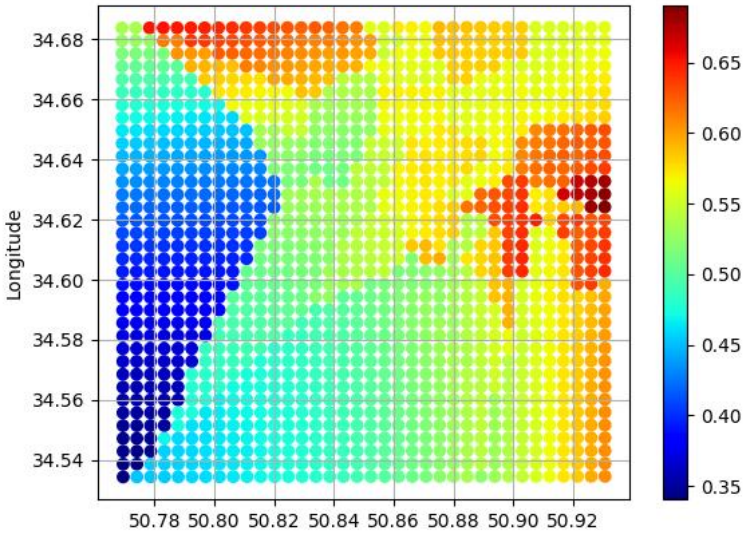

Fig. 7. PGA map for a 475-year return period (OpenQuake).

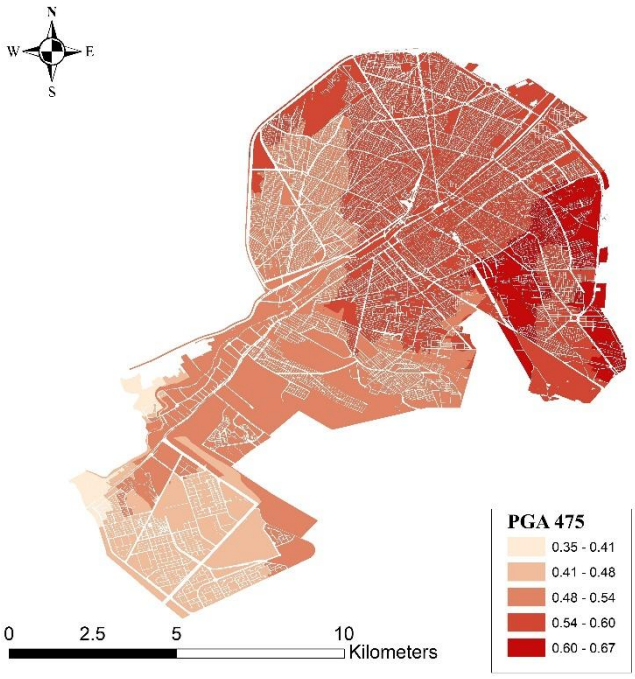

Fig. 8. PGA map for a return period of 475 years (equivalent to a 10% probability of exceedance in 50 years of structural life).

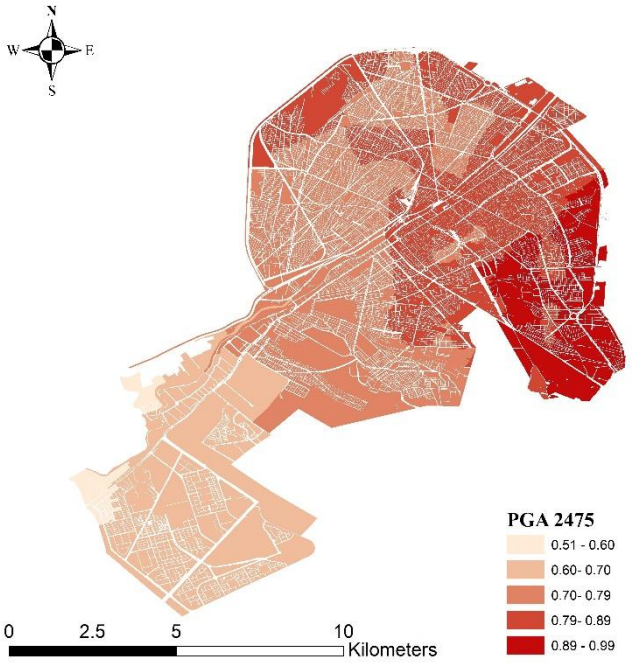

Fig. 9. PGA map for a return period of 2475 years (equivalent to a 2% probability of exceedance in 50 years of structural life).

5. Building vulnerability and probability of damage in Qom

As noted earlier, in this study the fragility curves developed by Fallah Tafti et al. [9] were employed. They prepared fragility curves for 19 building types in Iran, with their classification presented in Table 2. The fragility curves based on PGA are shown in Fig. 10. It should be emphasized that the building classification of Qom used in this study is consistent with the classification adopted by Fallah Tafti et al. [9], which ensures greater accuracy in the evaluation.

Table 2. Building classification according to the criteria of Fallah Tafti et al. [9].

Building Type	Structural Type	Building Height	Construction Quality (Year of Construction)	Building Type Code
1	Masonry	Low-rise (1–3 stories)	Low quality	MA_LR_LQ
2	Reinforced Concrete	Low-rise (1–3 stories)	Low quality (before 1987)	RC_LR_LQ
3	Reinforced Concrete	Low-rise (1–3 stories)	Medium quality (1987–2007)	RC_LR_MQ
4	Reinforced Concrete	Low-rise (1–3 stories)	High quality (after 2007)	RC_LR_HQ
5	Reinforced Concrete	Mid-rise (4–7 stories)	Low quality (before 1987)	RC_MR_LQ
6	Reinforced Concrete	Mid-rise (4–7 stories)	Medium quality (1987–2007)	RC_MR_MQ

7	Reinforced Concrete	Mid-rise (4–7 stories)	High quality (after 2007)	RC_MR_HQ
8	Reinforced Concrete	High-rise (>7 stories)	Low quality (before 1987)	RC_HR_LQ
9	Reinforced Concrete	High-rise (>7 stories)	Medium quality (1987–2007)	RC_HR_MQ
10	Reinforced Concrete	High-rise (>7 stories)	High quality (after 2007)	RC_HR_HQ
11	Steel Structure	Low-rise (1–3 stories)	Low quality (before 1987)	ST_LR_LQ
12	Steel Structure	Low-rise (1–3 stories)	Medium quality (1987–2007)	ST_LR_MQ
13	Steel Structure	Low-rise (1–3 stories)	High quality (after 2007)	ST_LR_HQ
14	Steel Structure	Mid-rise (4–7 stories)	Low quality (before 1987)	ST_MR_LQ
15	Steel Structure	Mid-rise (4–7 stories)	Medium quality (1987–2007)	ST_MR_MQ
16	Steel Structure	Mid-rise (4–7 stories)	High quality (after 2007)	ST_MR_HQ
17	Steel Structure	High-rise (>7 stories)	Low quality (before 1987)	ST_HR_LQ
18	Steel Structure	High-rise (>7 stories)	Medium quality (1987–2007)	ST_HR_MQ
19	Steel Structure	High-rise (>7 stories)	High quality (after 2007)	ST_HR_HQ

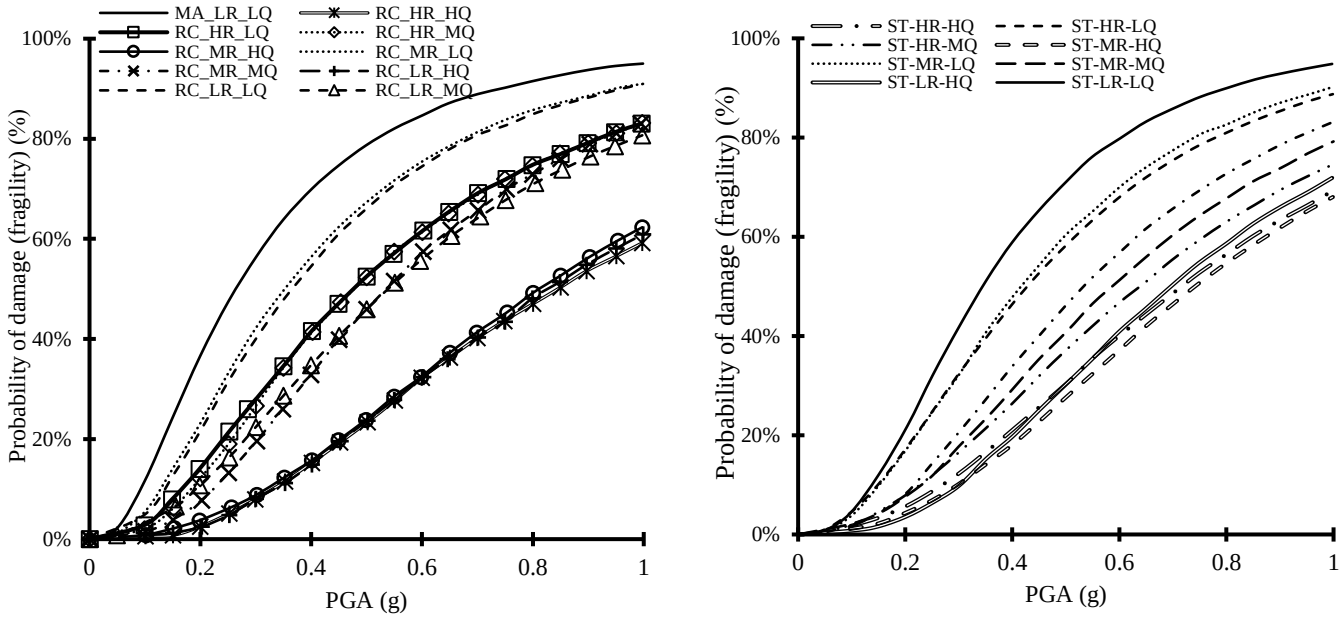

Fig. 10. Fragility curves against PGA, adapted from Fallah Tafti et al. [9] (a) Curves for reinforced concrete and masonry buildings (b) Curves for steel buildings.

For damage assessment of Qom's buildings, a database of buildings was compiled based on data provided by the Municipality of Qom. Subsequently, the buildings of Qom were classified according to the criteria of Fallah Tafti et al. [9]. Fig. 11 illustrates the classification of building types in Qom. Certain land uses (including vacant lots, parks and green spaces, agricultural lands, and similar categories) were considered as "type 0" and excluded from the evaluation. Interpretation of results is facilitated by numerical values. Accordingly, the statistical outcomes of this classification are presented in Table 3.

Table 3. Statistical assessment of existing buildings in Qom.

Building Type	Number	Percentage	Building Type	Number	Percentage
Dilapidated buildings (over 50 years old)	32,894	14.76%	Type 9 buildings	0	0.00%
Masonry buildings	182,289	81.80%	Type 10 buildings	1,088	0.49%
Reinforced concrete structures	18,686	8.39%	Type 11 buildings	369	0.17%
Steel structures	21,865	9.81%	Type 12 buildings	5,653	2.54%
Type 1 buildings	182,289	81.80%	Type 13 buildings	13,462	6.04%
Type 2 buildings	25	0.01%	Type 14 buildings	13	0.01%
Type 3 buildings	561	0.25%	Type 15 buildings	182	0.08%
Type 4 buildings	8,980	4.03%	Type 16 buildings	2,043	0.92%
Type 5 buildings	1	0.00%	Type 17 buildings	0	0.00%
Type 6 buildings	37	0.02%	Type 18 buildings	1	0.00%
Type 7 buildings	7,994	3.59%	Type 19 buildings	142	0.06%
Type 8 buildings	0	0.00%			

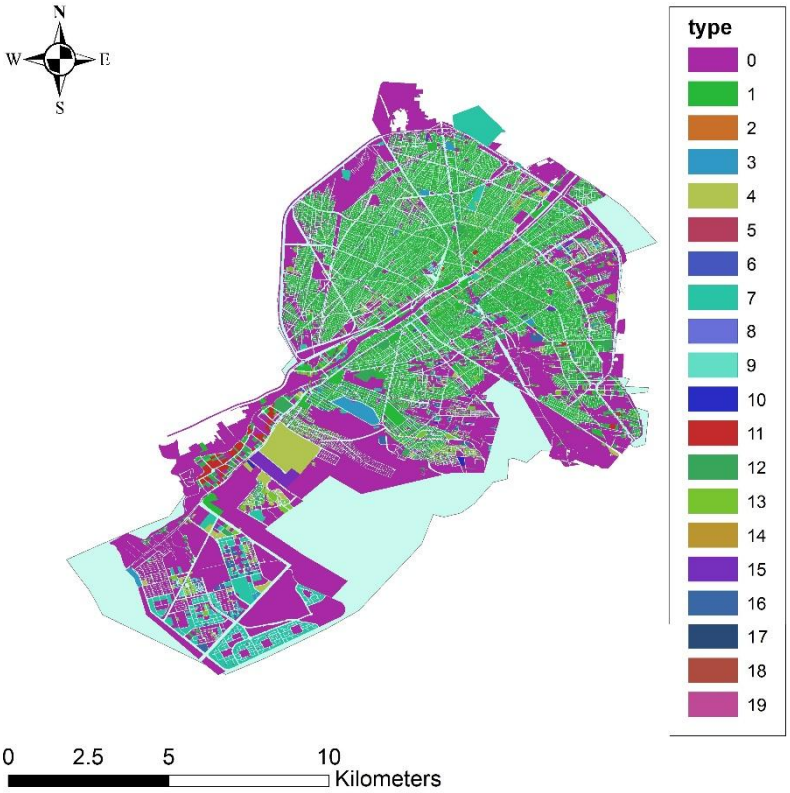

Fig. 11. Classification of building types in Qom.

The results indicate that 14.76% of Qom's buildings are over 50 years old and have reached the end of their service life (Table 3). Furthermore, 81.80% of Qom's buildings are masonry structures (including vaulted brickwork, adobe, and brick buildings). These structures lack adequate lateral load-bearing systems and are highly vulnerable to earthquakes. Based on these findings, it can be concluded that the primary challenge for Qom in terms of seismic resilience lies in the building stock, highlighting an urgent need for renovation and retrofitting.

For each building, PGA values corresponding to earthquakes with return periods of 475 and 2475 years were extracted using ArcGIS (Figs. 8 and 9). To estimate damage probabilities, the fragility curves developed by Fallah Tafti et al. [9] were parameterized through nonlinear regression. Building usage data for the city of Qom were exported into Microsoft Excel, where the buildings were classified according to Table 2. The equations were then applied to the classified building types in Excel, and the probability of damage was calculated. Table 4 presents the mean probability of damage for buildings under 475 and 2475 year return period earthquakes. For a more accurate evaluation of mean building damage, the number of units within each building was considered as an important indicator. Each floor was treated as one building unit (since the significance of a 10-story building is not equivalent to that of a single-story building when calculating mean damage). Table 4 shows the number of reinforced concrete, steel, and masonry buildings, along with the product of their counts and corresponding number of floors.

Table 4. Mean probability of building damage under earthquakes.

Category	Total Buildings	Reinforced Concrete	Steel Structures	Masonry Buildings
Number of buildings	222,840	18,686	21,865	182,289
Number of building units	276,567	65865	28268	182,434
Mean probability of damage (%) – 475 years	66.5	32.2	39.6	83.1

The mean probability of damage for building units in Qom under 475 and 2475 year return period earthquakes was estimated at 66.5% and 80.5%, respectively. These results are alarming. The primary reason lies in the prevalent building type in Qom, which is masonry construction with poor seismic performance. The mean probability of damage for masonry buildings under the 475 year earthquake was calculated at 83.1%, while steel and reinforced concrete buildings had mean probabilities of 39.6% and 32.2%, respectively (Table 4). Although the performance of framed buildings is not ideal, it is significantly better than that of masonry structures. As noted earlier, certain land uses) including vacant lots, parks, and agricultural lands(were excluded from the analysis. Figs. 12 and 13 illustrate the mean probability of building damage in Qom under 475 and 2475 year return period earthquakes. These figures show that the northern and central areas of Qom are in poor condition, whereas Pardisan and, more broadly, the western part of Qom Province exhibit better seismic performance. This is attributed to the newer construction in these areas and the use of earthquake-resistant structural systems. Furthermore, PGA values in western Qom were lower, consistent with the observed results.

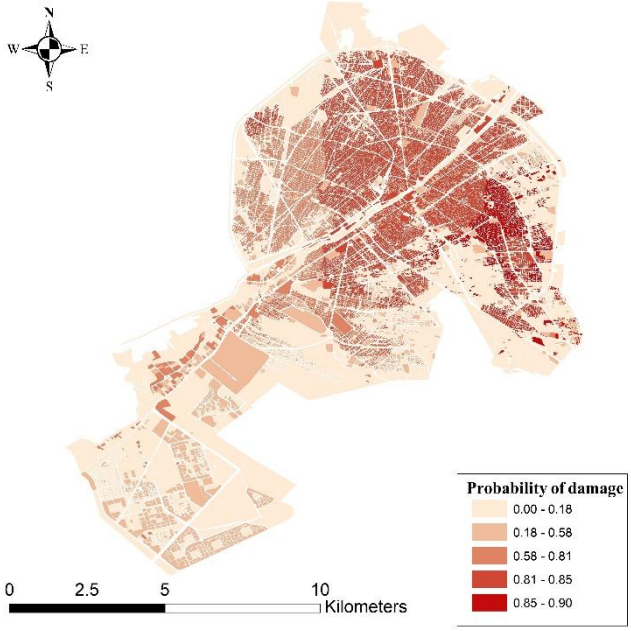

Fig. 12. Probability of building damage in Qom under a 475-year return period earthquake.

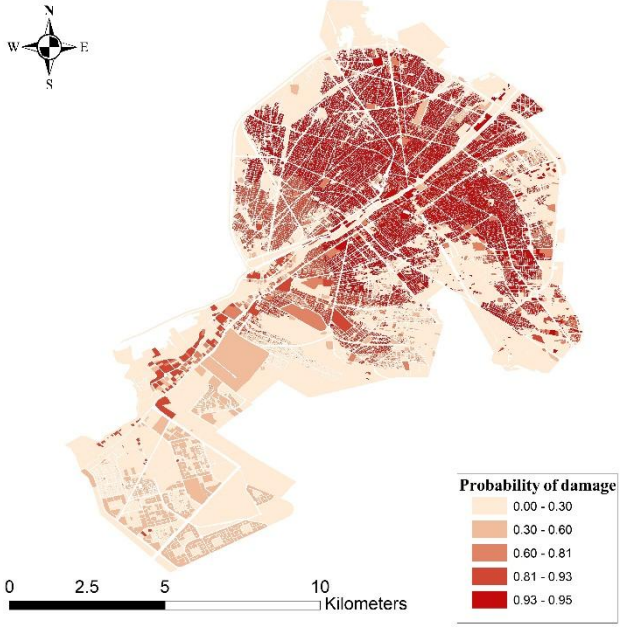

Fig. 13. Probability of building damage in Qom under a 2475-year return period earthquake.

6. Discussion

The findings of this study reveal a high seismic risk for Qom, driven by its significant seismic potential, indicated by a seismic potential index of 3.5 within 150 km, and the widespread presence of vulnerable unreinforced masonry buildings. The hazard assessment, using OpenQuake, shows substantial ground motion levels, particularly in the central and northern districts, with PGA values reaching up to 0.67 g for a 475-year return period. The soil conditions, characterized by Type II, III and IV classifications based on Vs30, suggest significant site amplification. This combination of high seismic hazard, weak soil conditions, and an extensive stock of non-ductile buildings creates a critical vulnerability, particularly in older urban areas, necessitating urgent measures to enhance the city's seismic resilience.

To mitigate this risk, a multi-faceted approach is required. The most pressing need is the retrofitting and strengthening of existing structures, particularly the extensive stock of unreinforced masonry buildings. Implementing a transparent building performance rating system, based on structural evaluation, could serve as a powerful incentive for owners to upgrade their properties. This system would empower the public to make informed decisions regarding building safety and encourage investment in seismic resilience. The municipality of Qom, as a key policy-making body in the construction sector, has a crucial role in promoting public awareness about seismic hazards and the importance of building safety through targeted educational campaigns. Financial incentives, such as tax reductions or subsidies, could further encourage property owners to undertake necessary strengthening measures. Enhancing the city's emergency response capabilities is equally important. The development of an online management system for crisis equipment, which provides real-time information on the location, quantity, and condition of available resources across municipal departments, would significantly improve operational efficiency and resource allocation during a disaster. This system would enable faster and

more coordinated response efforts. Furthermore, the creation and regular updating of accurate seismic hazard maps, which clearly delineate fault lines and high-risk zones, is essential. These maps should be made accessible to the public to increase awareness and inform land-use planning and construction decisions.

The design base acceleration (A) for the city of Qom per Standard 2800 [22] is 0.30g. The elastic response spectrum is obtained as A×B, where the factor *B* accounts for soil type and structural period, with maximum values of 2.5 for soil types 1 and 2, and 2.75 for soil types 3 and 4 per Standard 2800 [22] for Qom. The PGA values computed in this study (0.35g to 0.67g), accounting for local soil effects, yield an equivalent base acceleration range of 0.14g to 0.268g when divided by B_max, confirming that the standard's 0.30g is conservative and consistent with probabilistic seismic hazard analysis. These results enable the development of site-specific design response spectra, which, upon comparison with Standard No. 2800 spectra, can refine local amplification factors for precise structural analysis.

7. Conclusion

This study presented a comprehensive analysis of seismic hazard and building vulnerability in the city of Qom. First, the seismic potential index of Qom was determined using ArcGIS and available data, confirming the high seismicity of the region. Subsequently, maps of average shear-wave velocity to a depth of 30 meters and seismic soil classification of Qom were prepared. To estimate peak ground acceleration (PGA), the OpenQuake software was employed, and PGA maps for return periods of 475 and 2475 years were generated. Based on fragility curves derived from a domestic study, Qom's buildings were classified, and their damage under different earthquake scenarios was estimated. The findings can be summarized as follows.

- The seismic potential index (EPI) within a 150 km radius around Qom was examined. With an EPI of 3.5, Qom is among the most seismically active areas in the region. Although no historical record of major earthquakes exists, the high density of faults indicates significant seismic hazard potential.
- Results showed that Qom is highly vulnerable due to the predominance of masonry buildings lacking adequate lateral load-bearing systems. The mean probability of building damage under 475 and 2475 year return period earthquakes was estimated at 66.5% and 80.5%, respectively.
- Northern and central areas of Qom are more vulnerable, while newer western districts (particularly Pardisan) exhibit better seismic performance due to modern construction practices and earthquake-resistant structural systems.
- To reduce seismic risk in Qom, a comprehensive, multi-faceted approach is essential, prioritizing the retrofitting of vulnerable older buildings. Establishing a transparent building performance assessment system and incentivizing owners through financial mechanisms such as tax reductions are critical. Additionally, enhancing public awareness, strengthening emergency preparedness systems, and developing updated seismic hazard maps for urban planning and site selection are necessary steps to improve resilience and mitigate future losses.
- To enhance the accuracy and transferability of results, future studies should incorporate post-earthquake damage data from Qom for validation of fragility curves and hazard assessments. Additionally, integrating more advanced modeling approaches (e.g., nonlinear dynamic analysis) and considering spatial and socio-economic factors (e.g., construction quality, building age, population distribution) can improve risk quantification. Furthermore, developing fragility curves for modern building systems would support risk assessment in rapidly urbanizing areas.

Statements & Declarations

Author contributions

Mahdi Moradi: Conceptualization, Methodology, Data collection, Investigation, Writing - Original Draft, Supervision.

Mohammad Sadegh Torkaman: Data organization, Writing - Original Draft, Writing - Review & Editing.

Mohammad Reza Hasani: Writing - Review & Editing.

Funding

This research was conducted as part of the project entitled "Assessment of Qom's Resilience against Natural Hazards and Disasters (1404)", financially supported by the Municipality of Qom. The author gratefully acknowledges the Municipality of Qom for their financial support in carrying out this study.

Data availability

Data available on request due to project restrictions: The data presented in this study are available on request from the corresponding author. The data are not publicly available because the project was conducted as a research plan supported by the Municipality of Qom.

Declarations

The authors declare no conflict of interest.

References

[1] Municipality Statistical Municipality Yearbook of Qom (In Persian). 3rd ed. Qom (IR): Municipality of Qom; 2020.

[2] Seddighi, H., Seddighi, S. How much the Iranian government spent on disasters in the last 100 years? A critical policy analysis. Cost Effectiveness and Resource Allocation, 2020; 18: 46. doi:10.1186/s12962-020-00242-8.

[3] Eskandari, M., Afsari, N., Gheitanchi, M. R. Studying seismotectonics and seismicity of Qom province. 2008; 3: 59–71.

[4] Alizadeh, S., Honarvar, M. Assessing the physical resilience of urban areas (Case study: District 7 of Qom city) (In Persian). Architectural Studies, 2018; 1: 1–3.

[5] Khorasani Zadeh, M., Borzuyi Khah Foomani, M., Rahimi, A. A. Estimating the seismic vulnerability of Qom city based on the Alborz fault scenario. In: Proceedings of the 5th Comprehensive Conference on Crisis Management and HSE; 2019 Jan 19–20; Tehran, Iran. p. 1–8.

[6] Sianko, I., Ozdemir, Z., Hajirasouliha, I., Pilakoutas, K. Probabilistic seismic risk assessment framework: case study Adapazari, Turkey. Bulletin of Earthquake Engineering, 2023; 21: 3133–3162. doi:10.1007/s10518-023-01674-2.

[7] Sadeghi, M., Ghafory-Ashtiany, M., Pakdel-Lahiji, N. Developing seismic vulnerability curves for typical Iranian buildings. Proceedings of the Institution of Mechanical Engineers, Part O: Journal of Risk and Reliability, 2015; 229: 627–640. doi:10.1177/1748006X15596085.

[8] Rota, M., Penna, A., Strobbia, C. L. Processing Italian damage data to derive typological fragility curves. Soil Dynamics and Earthquake Engineering, 2008; 28: 933–947. doi:10.1016/j.soildyn.2007.10.010.

[9] Fallah Tafti, M., Amini Hosseini, K., Mansouri, B. Generation of new fragility curves for common types of buildings in Iran. Bulletin of Earthquake Engineering, 2020; 18: 3079–3099. doi:10.1007/s10518-020-00811-5.

[10] Lallemant, D., Kiremidjian, A., Burton, H. Statistical procedures for developing earthquake damage fragility curves. Earthquake Engineering & Structural Dynamics, 2015; 44: 1373–1389. doi:10.1002/eqe.2522.

[11] Cascone, V., Bayraktar, B., Basili, R., Crowley, H., Gibbons, S., Johnson, K., Lorito, S., Løvholt, F., Pagani, M., Romano, F., Tonini, R., Volpe, M. The GTM global PTHA: towards interoperability with the GEM OpenQuake engine. EGU General Assembly Conference Abstracts, 2025; EGU25–19264.

[12] Serdar Kirçil, M., Polat, Z. Fragility analysis of mid-rise R/C frame buildings. Engineering Structures, 2006; 28: 1335–1345. doi:10.1016/j.engstruct.2006.01.004.

[13] JICA, CEST The study on seismic microzoning of the Greater Tehran Area in the Islamic Republic of Iran. Japan International Cooperation Agency, Centre for Earthquake and Environmental Studies of Tehran, 2000; 291–390.

[14] Mansouri, B., Kiani, A., Amini-Hosseini, K. A Platform for earthquake risk assessment in Iran case studies: Tehran scenarios and Ahar-Varzeghan earthquake (In Persian). Journal of Seismology and Earthquake Engineering, 2014; 16: 51–69.

[15] Kamalian, M., Jafari, M. K., Ghayamghamian, M. R., Shafiee, A., Hamzehloo, H., Haghshenas, E., Sohrabi-bidar, A. Site effect microzonation of Qom, Iran. Engineering Geology, 2008; 97: 63–79. doi:10.1016/j.enggeo.2007.12.006.

[16] Ghafoori, S. M. M., Zafarani, H., Adlparvar, M. R. Identification of optimization-based probabilistic scenarios for seismic loss analysis of Qom lifelines (In Persian). Journal of Earthquake Sciences and Engineering, 2019; 7: 1–14.

[17] Vaseghi, Z., Dehkordi, M. R., Amiri, G. G., Seilany, A., Eghbali, M. Investigating Resilience Indicators of Urban Areas Against Earthquakes (Case Study: Qom City). 2024; doi:10.21203/rs.3.rs-4906728/v1.

[18] Shirvani Harandi, V., Amini Hosseini, K., Mansouri, B. Assessment of Key Parameters Affecting Vulnerability in District 4 of Qom City Due to a Potential Earthquake. Bulletin of Earthquake Science and Engineering, 2024; 11: 57–68. doi:10.48303/bese.2024.2031962.1168.

[19] Maghami, S., Sohrabi-Bidar, A., Bignardi, S., Zarean, A., Kamalian, M. Extracting the shear wave velocity structure of deep alluviums of “Qom” Basin (Iran) employing HVSR inversion of microtremor recordings. Journal of Applied Geophysics, 2021; 185: 104246. doi:10.1016/j.jappgeo.2020.104246.

[20] Ahmad, R. A., Singh, R. P., Adris, A. Seismic hazard assessment of Syria using seismicity, DEM, slope, active faults and GIS. Remote Sensing Applications: Society and Environment, 2017; 6: 59–70. doi:10.1016/j.rsase.2017.04.003.

[21] Mirzaei, N., Gheytanchi, M., Nasrieh, S., Raeisi, M., Zarifi, Z., Tabaei, G. Fundamental parameters of earthquakes in Iran (In Persian). 1st ed. Tehran (IR): Daneshnegar Publication; 2002.

[22] Building and Housing Research Center. Standard No. 2800: Iranian code of practice for seismic resistant design of buildings. Tehran (IR): 2800; 2015.

[23] Ramazi, H. R. Seismotectonic, seismicity and relative earthquake hazard zoning in Qom province. 1st ed. Qom (IR): Housing and Urbanization Organization of Qom Province; 2002.

[24] Pagani, M., Silva, V., Rao, A., Simionato, M., Johnson, K. OpenQuake engine manual. Global Earthquake Model Foundation, 2023; 3: 216.

[25] Wells, D. L., Coppersmith, K. J. New empirical relationships among magnitude, rupture length, rupture width, rupture area, and surface displacement. Bulletin of the seismological Society of America, 1994; 84: 974–1002. doi:10.1785/BSSA0840040974.

[26] Campbell, K. W., Bozorgnia, Y. NGA-West2 ground motion model for the average horizontal components of PGA, PGV, and 5% damped linear acceleration response spectra. Earthquake Spectra, 2014; 30: 1087–1115. doi:10.1193/062913EQS175M.

[27] Chiou, B. S.-J., Youngs, R. R. Update of the Chiou and Youngs NGA model for the average horizontal component of peak ground motion and response spectra. Earthquake Spectra, 2014; 30: 1117–1153. doi:10.1193/072813EQS219M.

[28] Akkar, S., Bommer, J. J. Empirical equations for the prediction of PGA, PGV, and spectral accelerations in Europe, the Mediterranean region, and the Middle East. Seismological Research Letters, 2010; 81: 195–206. doi:10.1785/gssrl.81.2.195.

Civil Engineering and Applied Solutions

Research Article

journal homepage: ceas.journals.umz.ac.ir

CEAS Civil Engineering and Applied Solutions

Feasibility Study to Evaluate the Application of Microsilica in Enhancing the Mechanical and Physical Characteristics of an Oil-Contaminated Silty Soil

Arvin Monjezi [a], Hamed Ahmadi Chenarboni [b], Hossein MolaAbasi [c*]

[a] *Department of Civil Engineering, Arak Branch, Islamic Azad University, Arak, Iran*
[b] *Department of Civil Engineering, Omidiyeh, Islamic Azad University, Ahvaz, Iran*
[c] *Department of Civil Engineering, Gonbad Kavous University, Gonbad Kavous, Golestan, Iran*

ARTICLE INFO

Keywords:
Oil-contamination
Microsilica
Silty soil
Stabilization
Unconfined compressive strength

Article history:
Received 12 December 2025
Accepted 26 April 2026
Available online 01 October 2026

ABSTRACT

This study investigates the modification of oil-contaminated soils using microsilica, a pozzolanic material. Laboratory tests, including compaction, Atterberg limits, direct shear, consolidation, and unconfined compression, were conducted. The results show that adding an optimal dosage of 15% microsilica improved soil mechanical properties: it reduced the compression index, decreased void ratio over time, and lowered plasticity. These improvements are attributed to particle agglomeration, flocculation, and long-term pozzolanic reactions between microsilica and soil minerals. Overall, 15% microsilica effectively enhanced the strength and consolidation behavior of oil-contaminated soils after 28 days of curing.

1. Introduction

The accelerated pace of urban development has contributed to a considerable growth in the construction of expansive, tightly clustered structures. Such extensive and dense construction activities necessitate a stable and robust foundation soil capable of supporting the imposed loads. Consequently, evaluating the strength and stability of the underlying soil becomes a critical step in selecting suitable sites before initiating structural design [1]. To put it differently, the soil's bearing capacity plays a critical role in determining a structure's ability to bear loads, making its assessment essential during initial studies. The behavior of soils is primarily influenced by their inherent properties and, secondarily, by environmental conditions and the detrimental impacts caused by human activities [2, 3].

A significant issue impacting various regions globally is the infiltration of oil into urban soils, resulting in contamination and alterations to the soil's fundamental properties [4-6]. This pollution may originate from multiple sources, including oil leaks near petroleum refineries, damaged pipelines and storage reservoirs, as well as the incorrect disposal of used engine oil [7, 8]. Crude oil is a type of hydrocarbon contaminant that disrupts the soil's structure and has harmful impacts on its physical, chemical, and mechanical characteristics [9-12].

Oil contamination significantly alters soil fabric and interparticle bonding mechanisms by coating soil particles with hydrocarbons, which disrupts direct particle-to-particle contact and reduces interparticle friction. This coating promotes a more porous, agglomerated, and loose structure, increasing void spaces, eccentricity, and overall porosity while decreasing density. In fine-grained soils, oil may enhance cohesion temporarily through viscous bridging, but it generally weakens van der Waals forces, cation exchange capacity, and frictional interactions, leading to reduced shear strength, unconfined compressive strength (UCS), internal friction angle, and load-bearing capacity. Permeability also decreases as oil blocks interparticle gaps, further compromising mechanical integrity and stability for foundations or slopes [13].

* Corresponding author.
E-mail addresses: hma@gonbad.ac.ir (H. MolaAbasi).

https://doi.org/10.22080/ceas.2026.30763.1063
ISSN: 3092-7749/
How to cite this article: Monjezi, A., Ahmadi Chenarboni, H., MolaAbasi, H. Feasibility Study to Evaluate the Application of Microsilica in Enhancing the Mechanical and Physical Characteristics of an Oil-Contaminated Silty Soil. Civil Engineering and Applied Solutions. 2026; 2(4): 15–27. doi:10.22080/ceas.2026.30763.1063.

Addressing these issues is a key priority for geotechnical engineers, who aim to render oil-contaminated soils suitable for civil engineering operations. Given that soil contamination remediation is both costly and time-intensive, identifying effective solutions for improving such soils has consistently garnered attention. If the soil's strength is insufficient to support the imposed loads, relocating the project may be considered. However, site-specific constraints and limited availability of alternative land often compel engineers to focus on soil improvement. Chemical stabilization is one method that effectively enhances soil behavior, especially in soils polluted with crude oil, where a sequence of chemical reactions plays a key role [14-16]. Earlier studies have shown that additives like lime and cement are crucial in stabilizing and restoring soils affected by contamination [5, 8, 17]. However, the use of these conventional materials, while potentially imposing significant costs on the project, may also present limitations, such as increased soil brittleness [18, 19]. Furthermore, the production of these additives is linked to the release of greenhouse gases, such as carbon dioxide, which result in significant and irreversible environmental harm [20]. Consequently, researchers continuously seek alternative materials to minimize the reliance on conventional binders. Microsilica, a largely spherical silica substance, emerges as a by-product of silicon alloy manufacturing and is produced in substantial quantities globally [21, 22]. Due to the adverse health effects associated with the release of this material as industrial waste into the environment, researchers are actively exploring its utilization in the construction sector. Its significant pozzolanic properties, coupled with its high reactivity, have rendered this industrial by-product a valuable substitute for traditional additives [23]. Furthermore, the amorphous structure of microsilica particles with their high Specific Surface Area (SSA) makes it a highly reactive substance [24]. Notably, microsilica particles are significantly smaller than conventional additives like cement, being 100 to 150 times smaller. This characteristic enables them to effectively fill the micro-pores between soil particles, resulting in a substantially denser composition. This distinctive attribute, known as the "filling/packing effect," markedly enhances the soil's physical and mechanical properties [21, 25].

The addition of microsilica (including precipitated silica, nanosilica, or silica fume) modifies these mechanisms by filling voids, promoting pozzolanic reactions with available calcium sources to form calcium silicate hydrate (C-S-H) gels, and creating cementitious bridges between particles. This results in a denser, more uniform, and isotropic fabric, with reductions in pore area, eccentricity, and porosity, while enhancing cohesion (e.g., doubling in some cases), friction angle, and shear strength. Consequently, UCS and load-bearing capacity are restored or even enhanced beyond that of untreated clean soil in many instances, depending on dosage, curing time, and soil type/contamination level [26, 27].

Previous studies have shown that the incorporation of microsilica can improve the strength characteristics of different soil types. However, most existing research has primarily focused on the use of microsilica in combination with calcium-based binders such as cement or lime, or on its application in uncontaminated soils. Consequently, there remains a significant lack of knowledge regarding the effectiveness of microsilica used alone for the stabilization of oil-contaminated fine-grained soils, particularly with respect to both strength and consolidation behavior. Therefore, this study aims to systematically evaluate the feasibility of using microsilica as a standalone stabilizing agent for oil-contaminated silty soil. Soil specimens were treated with microsilica contents of up to 20% and cured for designated periods. Subsequently, a comprehensive laboratory testing program—including compaction, Atterberg limits, direct shear, unconfined compressive strength (UCS), and one-dimensional consolidation tests—was conducted to assess the mechanical and physical performance of the treated soils.

2. Materials and method

2.1. Based soil and stabilizer

In this study, soil samples were sourced from a depth of 20 cm in proximity to an oil refinery located in Ahvaz in which the precise sampling location is depicted in Fig. 1. To characterize the soil, wet sieving and hydrometer tests were done in accordance with ASTM D422, and the results are presented in Fig. 2. Based on the test results, with over 50% passing through the #200 sieve, the soil was classified as fine-grained. The determination of Atterberg limits for the untreated soil further revealed that based on Unified Soil Classification System (USCS) it was silt with low plasticity (ML).

The hydrocarbon contamination in this study deposit was quantified using the conventional Soxhlet extraction method. Organic solvents such as dichloromethane were employed to extract petroleum compounds, and the contamination level was measured by comparing the original soil mass to the mass of the extracted hydrocarbons. The analysis showed that the soil contained 10% oil contamination by dry mass. The geotechnical characteristics of the contaminated soil such as liquid limit(LL), plasticity index(PI), specific gravity (Gs), maximum dty density (MDD), optimum moisture content (OMC) and unconfined compressive strength (UCS) are presented in Table 1. The oil-contaminated soil was dark brown in color and exhibited an unconfined compressive strength (UCS) of approximately 886 kPa.

The chemical structure of the soil was investigated through X-ray fluorescence (XRF) analysis, and the findings are provided in Table 2. Additionally, X-ray diffraction (XRD) analysis indicated that the soil primarily comprises quartz, calcite, dolomite, biotite, palygorskite, and gypsum. Microsilica used as a stabilizer in this research was sourced from the Iran Ferroalloy Industries Company. Its chemical and physical properties are outlined in Tables 2 and 3, respectively.

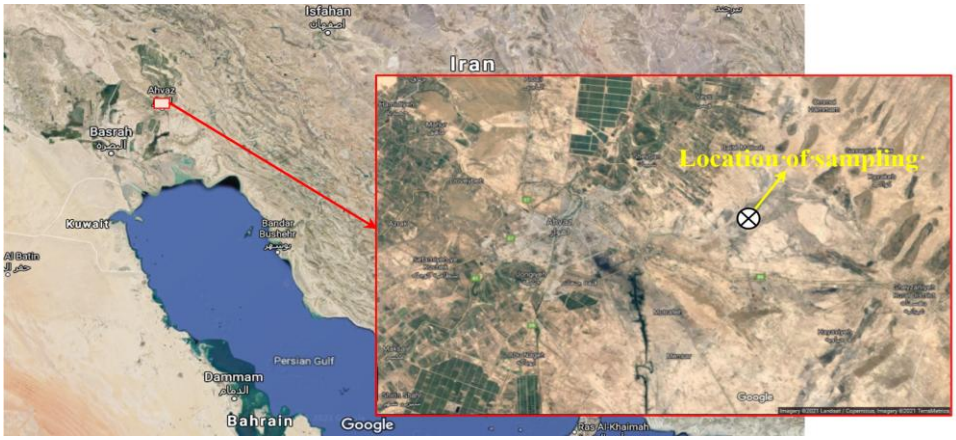

Fig. 1. Location of oil-contaminated soil used in this study.

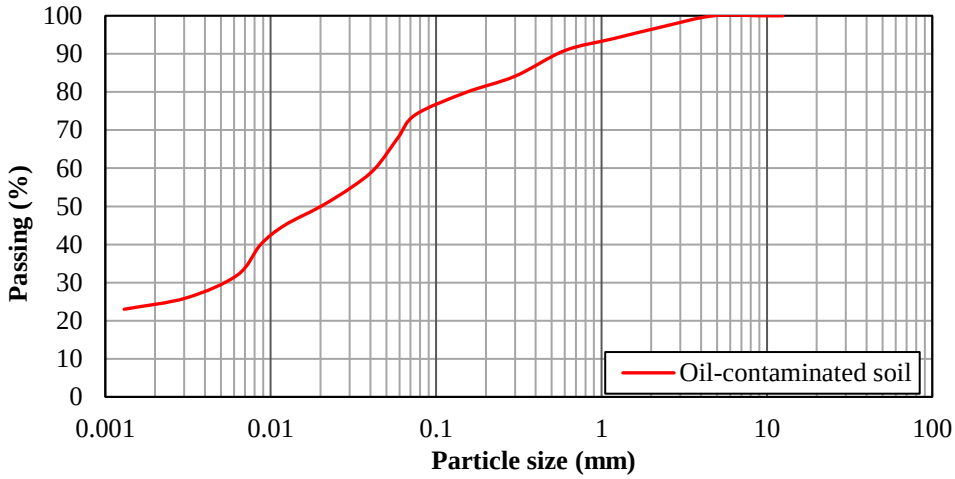

Fig. 2. Particle size distribution of the studied oil-contaminated soil.

Table 1. Oil-contaminated soil index.

Characteristics	Value	ASTM Standard
LL (%)	38.13	ASTM D4318
PI (%)	26.70	ASTM D4318
G_S	2.62	ASTM D854
MDD (g/cm^3)	1.9	ASTM D698
OMC (%)	13.2	ASTM D698
UCS untreated sample in OMC and MDD (kPa)	886	ASTM D2166
Color	Dark brown	-

Table 2. Chemical compositions (percentage in weight (%)) of materials used in this study.

Chemical composition	Material	
	Soil	Microsilica
SiO_2	66.31	91.7
Al_2O_3	25.42	1.13
Fe_2O_3	1.12	1.42
CaO	1.23	1.52
MgO	0.21	0.29
Na_2O	0.12	0.51
K_2O	0.1	1.21
MnO	-	0.7
SO_3	-	0.33
TiO_2	-	-
LOI	5.49	1.19

*Loss on ignition

Table 3. Physical properties of microsilica used in this study.

Microsilica properties	Value
Structure	Amorphous
Size, μ	0.2-0.3
Physical form	Powder
Color	White
Bulk density, kg/m^3	200
Specific gravity (G_S)	2.64

2.2. Sample preparation and methodology

To improve the strength characteristics and stabilize the oil-contaminated soil, microsilica was added at contents of 5%, 10%, 15%, and 20% by dry weight of soil. For each microsilica dosage, a comprehensive experimental program was implemented to evaluate its effectiveness. First, standard Proctor compaction tests were performed on untreated and treated samples to determine the Optimum Moisture Content (OMC) and Maximum Dry Density (MDD) required for specimen preparation. Dry microsilica powder was initially mixed thoroughly with the soil, after which water was added to achieve a uniform mixture. Compaction tests were conducted in accordance with ASTM D698.

Cylindrical specimens with a diameter of 3.5 cm and a height of 10 cm were prepared at their respective OMC and MDD values for Unconfined Compressive Strength (UCS) testing. The specimens were sealed in airtight plastic containers and cured at room temperature for 28 days before being tested according to ASTM D2166.

Direct shear tests were also conducted following ASTM D3080. The soil–microsilica mixtures were compacted into square shear boxes with a side length of 5 cm in three layers, each 2 cm thick, at their corresponding OMC and MDD. After 28 days of curing, vertical normal stresses of 50, 100, and 150 kPa were applied to determine shear strength parameters, including cohesion (C) and internal friction angle (ϕ).

Atterberg limits tests were performed on untreated and treated soils in accordance with ASTM D4318 to evaluate changes in soil plasticity due to microsilica addition. After mixing soil, microsilica, and water, the samples were cured for 28 days, and Liquid Limit (LL) and Plastic Limit (PL) were determined. The Plasticity Index (PI) was then calculated as the difference between LL and PL.

One-dimensional consolidation tests were carried out in accordance with ASTM D2435 to assess compressibility and consolidation characteristics. Soil–microsilica mixtures prepared at their respective OMC and MDD were placed into molds with a diameter of 50 mm and a height of 20 mm and tested in an oedometer after curing periods of 7 and 28 days. These tests provided key parameters such as compression index, coefficient of consolidation, and void ratio for evaluating the settlement behavior of stabilized soils.

3. Result and discussion

3.1. Effect of microsilica on MDD and OMC of the contaminated soil

In this study, standard Proctor tests were performed on all samples, including parent oil-contaminated soil and microsilica-stabilized ones, to determine the OMC and MDD values. Figs. 3 and 4 show the results of the compaction test in full. As can be seen, the addition of microsilica to oil-contaminated soil increased the OMC as well as decreased the MDD. The inclusion of microsilica into the soil caused a change in the particle size distribution and increased the particle surface of the blends compared to that of the oil-contaminated soil sample. The amount of these changes was directly related to the amount of microsilica in the compounds. Adding 20% of microsilica content to contaminated soil increased OMC from 13.18% to 16.3%. In addition, as the OMC increased, the MDD of the composites gradually decreased. This effect can be attributed to the additional microsilica filling the voids between the particles of the samples [28, 29]. As can be seen in Fig. 4, the addition of 5% microsilica had little effect on MDD changes. The most significant increase in performance was observed with the addition of 15% microsilica to the contaminated soil. This specific microsilica content reduced the soil's Maximum Dry Density (MDD) from 1.92 to 1.88 g/cm³. According to previous studies, [28, 29], a similar behavior was observed for soils without oil-contaminants stabilized with microsilica.

3.2. Effect of microsilica on consistency limits of the contaminated soil

To determine the liquid limit (LL), plastic limit (PL), and Plasticity Index (PI) of oil-contaminated soil, the Atterberg limits tests were performed on the samples, the results of which are shown in Figs. 5 and 6. As shown in Fig. 5, as the amount of microsilica increased, the LL and PL of the soil decreased. The trend of changing these two parameters was such that their differences (PI) also showed a downward behavior. The incorporation of microsilica into the soil particles can induce particle flocculation over time, which in turn reduces the Liquid Limit (LL) and, consequently, decreases the soil's plasticity [30, 31].

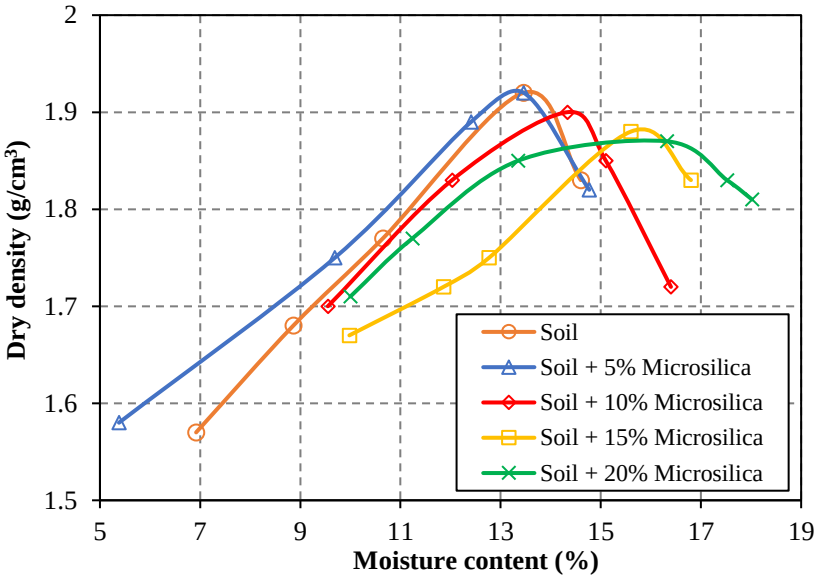

Fig. 3. Results of compaction tests on microsilica-stabilized oil-contaminated soil samples.

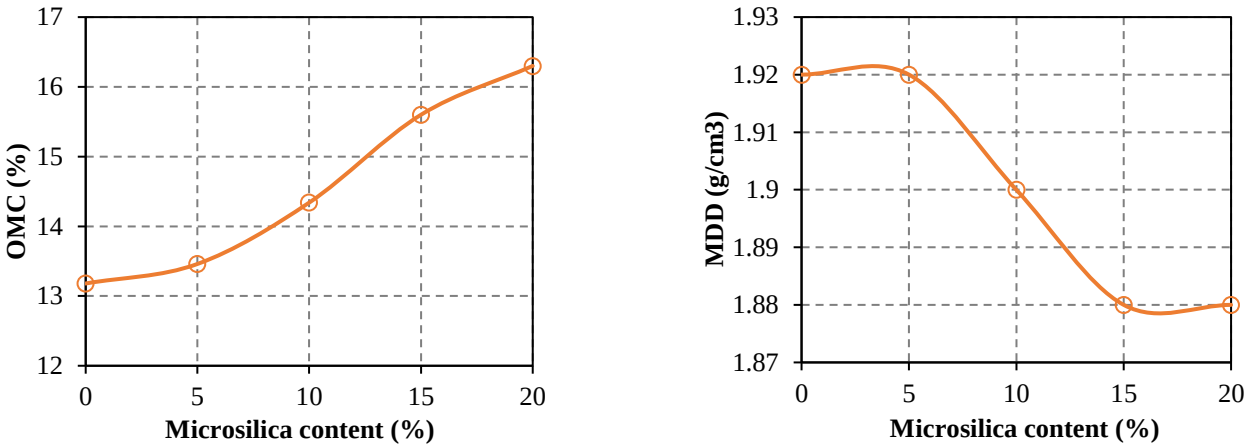

Fig. 4. Variation of OMC and MDD of microsilica-stabilized oil-contaminated soil samples.

The amount of 20% microsilica was able to reduce the LL from 38.13% to about 31%. This amount of additive was also able to reduce the PI by about 15%. It should be noted that this decrease in the PI and LL could change the USCS classification from ML to CL, as shown in Fig. 6. This can be due to the simultaneous reduction of PL and LL with the addition of microsilica, which changes the soil group.

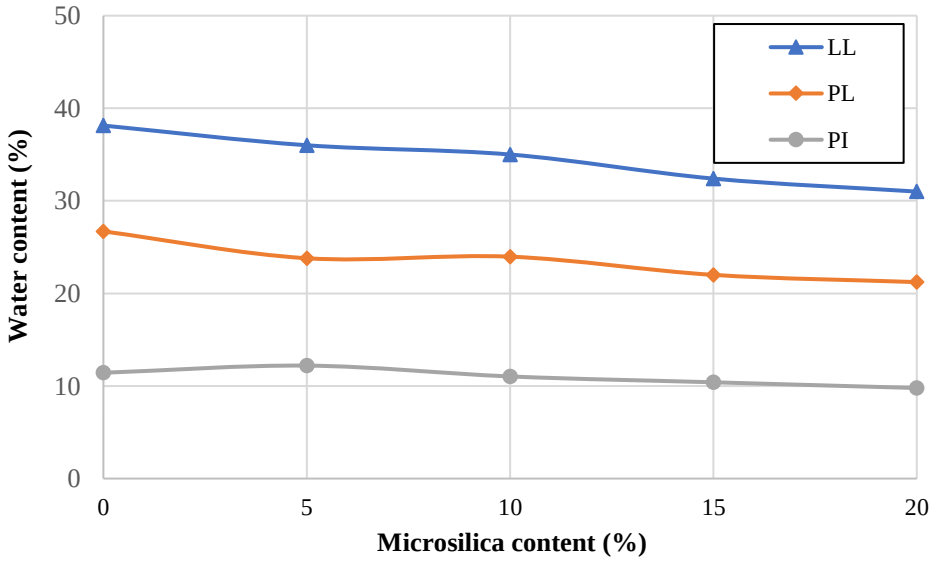

Fig. 5. Variation of Atterberg limits of microsilica-stabilized oil-contaminated soil samples.

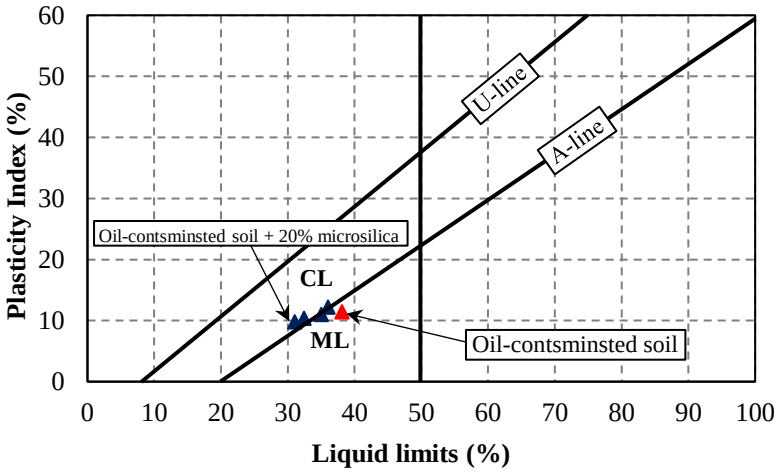

Fig. 6. Plasticity chart for microsilica-stabilized oil-contaminated soil samples.

3.3. Effect of microsilica on shear properties of the contaminated soil

In this study, direct shear tests were performed on the samples under fully saturated conditions, representing the critical state of fuel oil-contaminated soils after microsilica stabilization and curing. Saturation ensured uniform pore water distribution and accounted for the effects of moisture on interparticle friction and adhesion. Testing under these conditions provides a realistic and reliable assessment of shear strength across different microsilica dosages while reflecting the potential impact of oil contamination. Fig. 7 presents the shear strength changes for oil-contaminated soils stabilized with different amounts of microsilica. For this purpose, three different vertical confining pressures of 50, 100 and 150 kPa were considered to be able to determine the changes in cohesion (C) and friction angle (φ), the results of which are shown in Fig. 8. According to Fig. 7, it can be seen that the addition of microsilica up to 15% to oil-contaminated soil increased the shear strength of the soil. The shear strength of oil-contaminated soil at a vertical confining pressure of 50 kPa was approximately 33 kPa. In contrast, the sample containing 15% microsilica under similar conditions exhibited a shear strength of around 55 kPa. Additionally, as the vertical confining pressure increased, the shear strength also increased. Specifically, the shear strength of the 15% microsilica sample at vertical confining pressures of 100 kPa and 150 kPa rose by approximately 20% and 111%, respectively, compared to the strength at 50 kPa.It should be noted that the incorporation of more microsilica (20%) reduced shear strength. The reduction in shear strength at 150 kPa is more pronounced than at lower stresses. Although minor experimental errors cannot be entirely ruled out, repeated tests confirmed the trend. This stress-dependent behavior likely arises from increased particle rearrangement and localized brittleness at higher microsilica contents, which reduces interparticle contacts and shear resistance.

As shown in Fig. 8, with the addition of 15% microsilica to the oil-contaminated soil, the amount of internal friction angle increased from 24.65° to 31.38°. However, with the addition of 20% microsilica, despite increasing the cohesion to about 19.66 kPa, the internal friction angle and the value of shear strength decreased. It is important to note that the value of cohesion, as well as the internal friction angle of the soil, was very low due to the coating of soil particles with petroleum products which results in reduced interaction between particles. As the dosage of microsilica in the oil-contaminated soil composition increased, the value of cohesion and friction angle increased. The observed effect can be attributed to the increase in Optimum Moisture Content (OMC) corresponding to the stabilized samples, which in turn enhances the adhesion between the soil particles [28]. Additionally, the increase in the friction angle of the samples is attributed to the fact that, in the absence of microsilica, oil acts as a lubricant, allowing the particles and soil grains to slide past one another. This reduces the interaction and friction between the particles [32, 33].

The observed decrease in friction angle when microsilica content increases from 15 to 20 % can be attributed to over-saturation of the soil matrix with fine particles, which reduces interparticle friction and promotes a more brittle structure. At higher microsilica dosages, excessive gel formation and filling of voids can partially disrupt the natural particle contacts, leading to a reduction in the soil's internal resistance to shear. This explains why, despite small changes in unconfined compressive strength, the friction angle declines beyond the optimal 15 % dosage, highlighting the importance of identifying an optimal microsilica content for balancing strength gain and shear stability.

3.4. Effect of microsilica on UCS of the contaminated soil

Fig. 9 demonstrates the results of the UCS test in terms of stress-strain changes. As observed, the addition of microsilica has positively impacted the compressive strength of oil-contaminated soil. As the strain in the microsilica-treated samples increased, it led to a shift in the soil's behavior from a brittle state to a more ductile state. The ultimate strength for each sample is shown in Fig. 10. The addition of 15% microsilica to the oil-contaminated soil significantly improved its structure and increased the sample's strength by approximately 158% compared to the unstabilized soil, achieving a maximum Unconfined Compressive Strength (UCS) of 2288 kPa. Notably, the strain at fracture for this sample was 12.38%, much higher than the 5.1% strain observed in the unstabilized contaminated soil. However, further increases in microsilica content not only led to a slight reduction in compressive strength but also decreased the strain by about 10.92%.

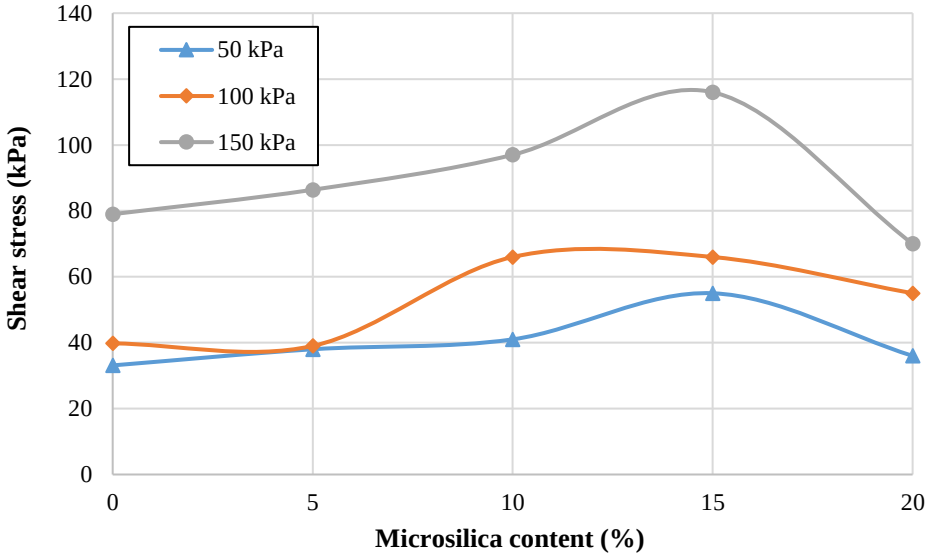

Fig. 7. Variation of shear strength for microsilica-stabilized oil-contaminated soil samples.

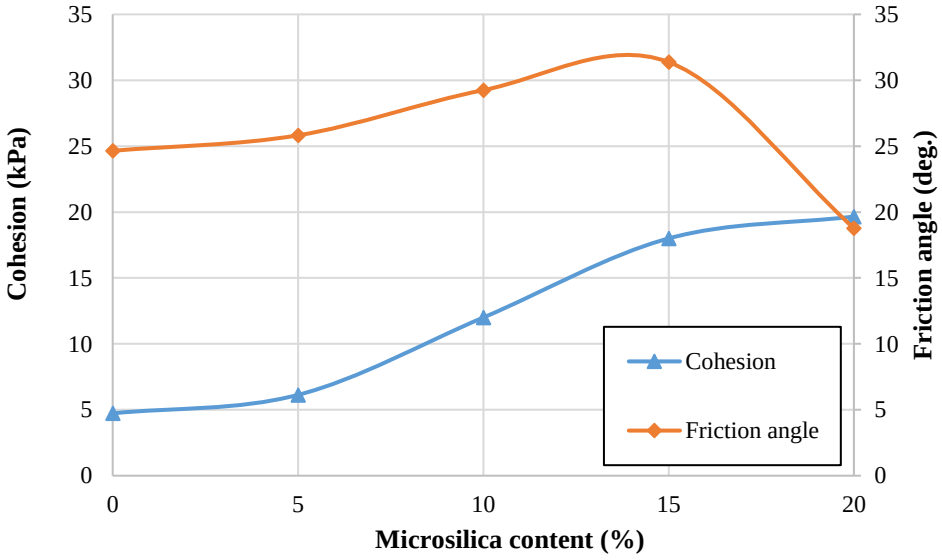

Fig. 8. Variation of cohesion and friction angle for microsilica-stabilized oil-contaminated soil samples.

These results align well with the shear strength test outcomes, indicating that the optimal microsilica content for oil-contaminated soil is 15%. The observed increase in compressive strength can be attributed to the pozzolanic reaction between the silica and soil particles in the presence of water, which occurs over time, enhancing the mechanical properties of the soil. The soil contains clay minerals, which provide a limited amount of naturally occurring calcium (e.g., in carbonates or clay lattice structures). While classical pozzolanic reactions typically require additional calcium sources such as lime or cement, the observed improvements in soil properties are primarily attributed to surface interactions between microsilica and clay particles, particle agglomeration, and flocculation. Therefore, even in the absence of added calcium, microsilica can effectively modify the mechanical behavior of clay-rich soils. This point has been clarified in the manuscript, moderating claims related to classical pozzolanic reactions and emphasizing the combined mechanical and surface-interaction effects of microsilica. Additionally, the internal friction of microsilica particles plays a crucial role in strengthening the oil-contaminated samples. Microsilica reacts with the soil particles, improving both internal friction and cohesion. This reaction counters the lubricating effect of the oil surrounding the soil particles, allowing the formation of a more cohesive and integrated structure, ultimately leading to increased strength.

3.5. Effect of microsilica on consolidation behavior of the contaminated soil

One of the key parameters in foundation design on soil is the compression index (Cc), as it provides valuable insight into soil settlement when subjected to increased loads. The compression index is determined from the slope of the linear portion of the e-log p curve, which represents the relationship between the void ratio (e) and the logarithm of the applied pressure (p) [34]. In this study, one-dimensional consolidation test was performed on all samples after 7 and 28 days of curing, during which the compression index, coefficient of consolidation and void ratio were determined, the results of which are shown in Fig. 11. The results of the one-dimensional consolidation test indicate that the addition of microsilica to the soil led to a reduction in the compression index of the oil-contaminated soil after 7 and 28 days of curing.

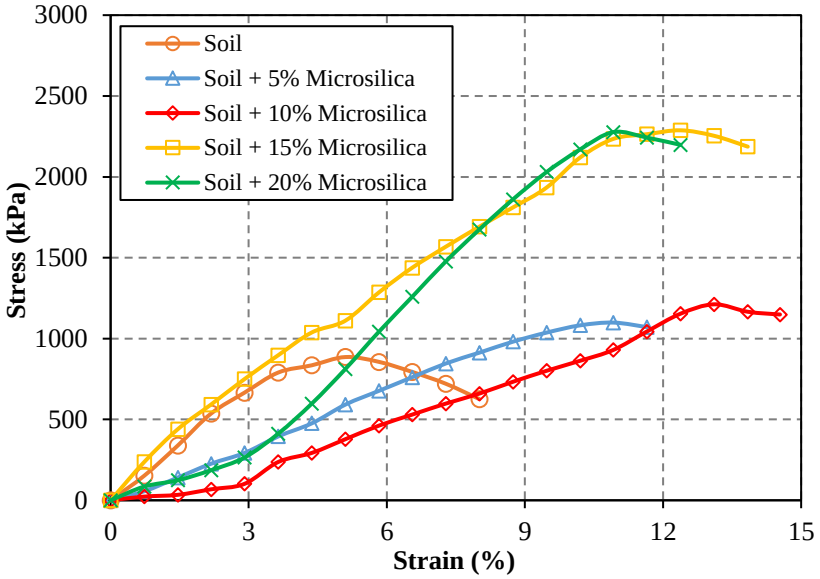

Fig. 9. Stress-strain curves for microsilica-stabilized oil-contaminated soil samples.

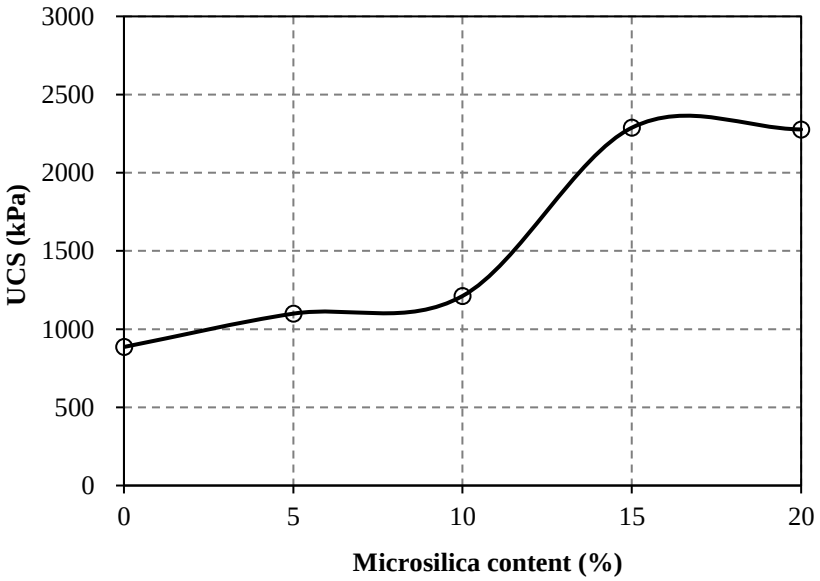

Fig. 10. Variation of the UCS for microsilica-stabilized oil-contaminated soil samples.

Initially, the compression index for the contaminated soil was 0.192. However, with the incorporation of microsilica, this value decreased by 15%, reaching approximately 0.129 after 7 days of curing (Fig. 11a). Furthermore, the compression index continued to decrease over the curing period, reaching approximately 0.11 after 28 days. This significant reduction in the compression index can be attributed to the reaction between microsilica and the oil-contaminated soil particles. During these chemical reactions, a cementitious gel is formed, which enhances the resistance of the samples to external loads, thereby improving the soil's overall structural integrity [35]. However, with the increase of microsilica, the compression index increased again and reached 0.138.

Another important parameter derived from the one-dimensional consolidation test is the coefficient of consolidation (Cv), which is usually obtained through the graphical method (i.e., logarithm of time) introduced by Casagrande and Fadum [36]. The coefficient of consolidation is a measure of the rate at which consolidation occurs in soil under a given load. It indicates the time required for a certain degree of consolidation to take place, reflecting the soil's ability to undergo compression over time when subjected to increasing pressure [37]. It should be noted that two factors can affect this parameter, including the amount of compressed water and the flow rate of that water. Fig. 11b shows the results obtained for the coefficient of consolidation. As can be seen, the addition of microsilica to the oil-contaminated soil increased this coefficient at an early age. So that with the addition of 15% microsilica, Cv increased from 0.015 cm2/sec for untreated soil to 0.041 cm2/sec. But with the addition of microsilica up to about 20%, it was observed that the Cv value was reduced to 0.036 cm^2/sec. It should be noted that the addition of microsilica to the soil after 7-day curing caused chemical reactions in the samples. Short-term reactions, such as cation exchange, cause the structure of the contaminated soil to flocculate, leading to an increase in the size of the soil particles. This, in turn, results in an increased coefficient of consolidation (Cv) as well as higher permeability. In general, it can be stated that after 7 days of curing, attractive forces dominate over repulsive forces due to the increased ion concentration. The replacement of monovalent ions on the surfaces of soil particles with multivalent ions from the additive leads to the particles coming closer together. This process creates a flocculated structure in

the soil, which increases the void size within the soil samples [21]. However, over time, as long-term reactions progress, the coefficient of consolidation decreases further, even becoming lower than that of the oil-contaminated soil. This reduction can be attributed to the formation of new cementitious products during the pozzolanic reactions, which fill the voids between the soil particles, thereby reducing the soil's permeability and enhancing its overall stability. As can be seen, the addition of microsilica to the contaminated soil after 28 days of treatment causes the coefficient of consolidation to decrease to about 0.018 cm2/Sec. Therefore, the variations of Cv in the short and long term were different and opposite to each other.

Fig. 11c illustrates the variation in initial void ratios for different oil-contaminated soil compositions. As the microsilica content increased to 15%, the void ratio increased, but then decreased with a further increase in microsilica content to 20% after 7 days of curing. The void ratios for oil-contaminated soil stabilized with 15% and 20% microsilica were 0.55 and 0.49, respectively, compared to 0.47 for the unstabilized contaminated soil. The addition of microsilica to the samples led to a decrease in the density of the samples. This can be attributed to the chemical reactions between the microsilica and soil particles, which result in the agglomeration or flocculation of the particles. This leads to an increase in the void ratio, which consequently decreases the density of the samples, as observed in the density test. However, as previously mentioned, after 28 days of curing, the formation of new cementitious products fills the voids within the soil, reducing the void ratio. Specifically, after adding 15% microsilica to the contaminated soil, the void ratio decreases to approximately 0.35 after 28 days of curing.

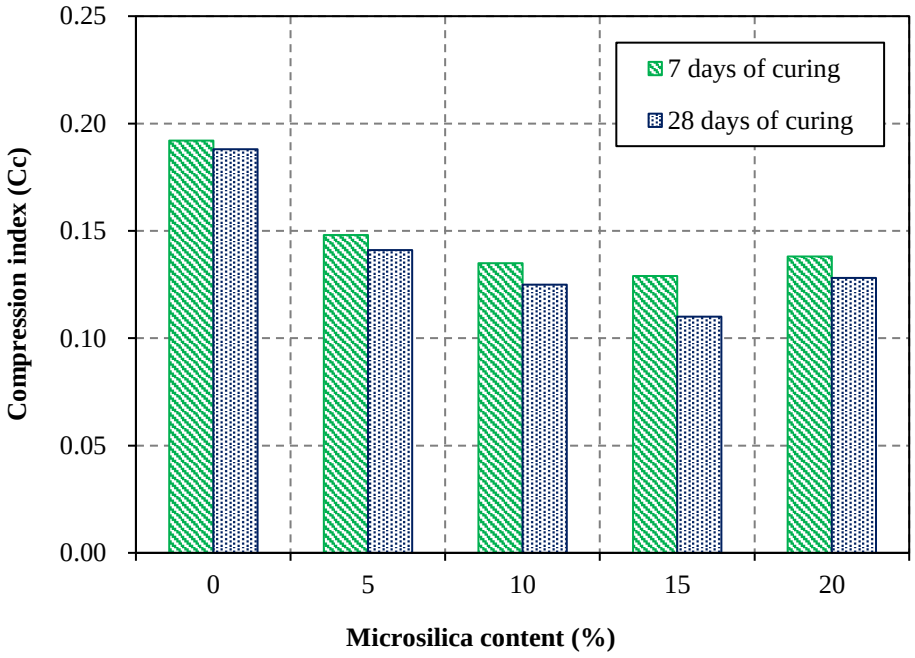

(a)

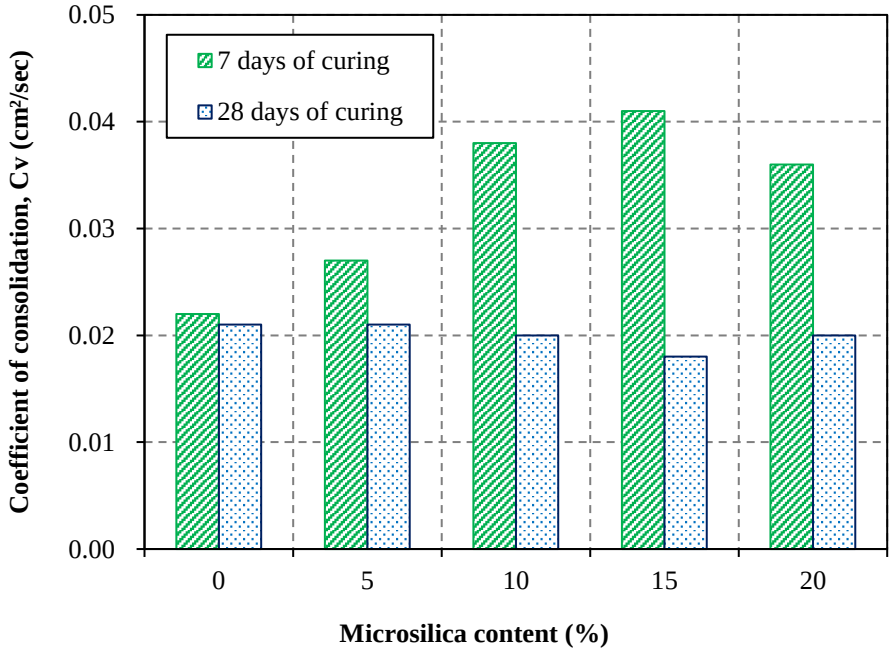

(b)

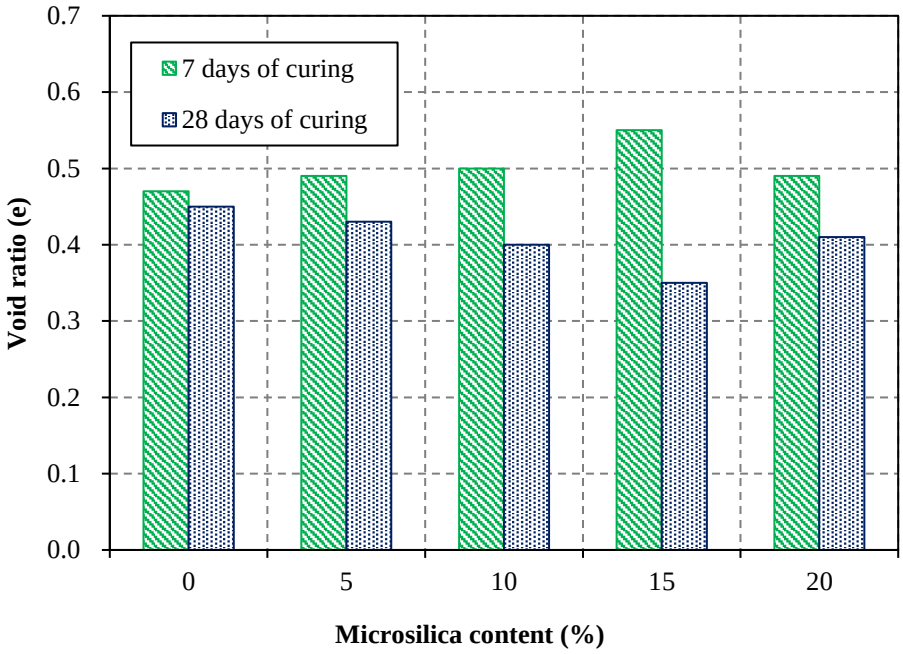

(c)

Fig. 11. Variation of a) compression index, b) coefficient of consolidation, and c) void ratio for microsilica-stabilized oil-contaminated soil samples.

4. Discussion

The results of this study indicate that the addition of 15 % microsilica to fuel oil-contaminated soil significantly improves soil plasticity, unconfined compressive strength, shear strength, and consolidation parameters. This dosage was selected as the optimal content under controlled laboratory conditions based on detailed sensitivity analysis, which included microsilica contents up to 20 %. The data show that while the maximum dry density remained almost unchanged between 15 % and 20 %, shear strength decreased beyond 15 %, and unconfined compressive strength showed minimal change, indicating that 15 % represents a balance between mechanical improvement and potential adverse effects. Consolidation parameters after 28 days further confirmed that 15 % microsilica provides an effective balance between strength development and settlement control. The primary mechanisms contributing to these improvements include pozzolanic reactions, flocculation, and cementitious gel formation, as reported in previous studies.

Unlike nanosilica, microsilica is relatively cost-effective and widely available for laboratory and research purposes, allowing for precise and controlled evaluation of its effects. It should be noted that this study focuses on the research and laboratory evaluation phase, and the results cannot be directly generalized to large-scale field applications. For practical implementation, further consideration of optimal dosages, constructability, and economic feasibility is required. With ongoing technological advancements and improvements in production processes, the cost of microsilica and nanosilica is expected to decrease, enhancing their practical applicability and economic viability in engineering projects.

The observed temporal reduction in compression index and void ratio indicates that time-dependent pozzolanic reactions play a significant role in the long-term consolidation behavior of microsilica-stabilized oil-contaminated soils. As curing progresses, the pozzolanic reaction between microsilica and soil minerals promotes the formation of additional cementitious gels, which fill voids, bind soil particles, and increase structural stiffness. This process not only reduces compressibility but also enhances resistance to settlement under sustained loading. While long-term field behavior beyond laboratory conditions remains to be confirmed, these findings highlight the importance of curing time in optimizing the consolidation performance of treated soils and provide a basis for future investigations on long-term settlement under realistic field loads.

In addition to geotechnical performance, the sustainability aspects of microsilica should also be considered. Microsilica, as an industrial by-product from silicon and ferrosilicon alloy production, represents industrial waste valorization, converting a by-product into a value-added material. Its use contributes to resource efficiency, reduces environmental burdens from waste disposal, and aligns with sustainable engineering practices. Compared to traditional stabilizers such as Portland cement or lime, which are energy-intensive and associated with higher carbon footprints, the use of microsilica can lower the overall environmental impact of soil stabilization. Recent studies in the literature have emphasized the importance of evaluating both mechanical performance and environmental compatibility when selecting stabilizing materials, including assessing potential reductions in environmental burden associated with alternative additives such as microsilica and nano-TiO_2 in geotechnical soil stabilization [38].

The observed reduction in soil plasticity and improvement in unconfined compressive strength after 28 days highlight the effectiveness of microsilica stabilization under controlled laboratory conditions. These results suggest that the treated soils can be considered for pavement subbase or road construction applications, where moisture conditions can be controlled, and uniform compaction is achievable. However, for semi-deep or deep soil improvement projects, the variability in moisture content,

heterogeneous contamination levels, and scale effects in the field may influence the stabilization efficiency. Therefore, further investigations, including pilot-scale or in-situ trials, are necessary to assess the practical applicability and optimize treatment strategies under real field conditions.

Furthermore, the improved strength and compressibility of microsilica-stabilized oil-contaminated soils have direct implications for deep foundation performance. The modified soil parameters, including reduced plasticity, increased shear strength, and controlled compressibility, can be used as input in both analytical and experimental assessments of helical pile capacity under tension and compression, as demonstrated in previous studies on dense sand. Incorporating these parameters allows the extension of existing models to contaminated and remediated ground conditions, providing valuable guidance for foundation design and performance prediction in areas affected by fuel oil contamination. Further research is recommended to validate these applications under field conditions with variable moisture content and soil heterogeneity.

5. Concluding remark

In this study, an effort was made to explore the potential of using microsilica to stabilize oil-contaminated soils. To achieve this, a series of laboratory tests was conducted on soil samples both with and without microsilica, leading to the following key findings:

- The addition of microsilica to the oil-contaminated soil resulted in an increase in Optimum Moisture Content (OMC) and a decrease in Maximum Dry Density (MDD). The most significant change in MDD was observed with the inclusion of 15% microsilica in the contaminated soil. Furthermore, the incorporation of microsilica altered the particle size distribution and increased the particle surface area of the mixture compared to the untreated oil-contaminated soil sample.
- The inclusion of microsilica in the soil matrix resulted in the flocculation of particles after the curing period, leading to a reduction in both the Liquid Limit (LL) and Plastic Limit (PL), which, in turn, decreased the plasticity of the soil samples. Notably, the reduction in Plasticity Index (PI) and LL could potentially alter the Unified Soil Classification System (USCS) classification from ML (Silt with Low Plasticity) to CL (Clay with Low Plasticity).- The addition of microsilica up to 15%, along with an increase in vertical confining pressure, resulted in an enhancement of the shear strength of the soil samples. Additionally, the incorporation of microsilica into the contaminated soil reduced the lubricating effect, thereby increasing both the cohesion and friction angle of the soil.
- The addition of 15% microsilica to the contaminated soil increased its unconfined compressive strength (UCS) by approximately 158% after 28 days of curing, reaching a maximum value of 2288 kPa. Furthermore, the strain at fracture for this sample was 12.38%, which is significantly higher than the 5.1% observed for the untreated contaminated soil. The increase in UCS in the presence of microsilica can be attributed to the pozzolanic reaction between the silica and soil particles in the presence of water, which enhances the strength of the soil.
- As the microsilica content increased to 15%, the compression index decreased after both 7 and 28 days of curing. Meanwhile, the coefficient of consolidation and void ratio showed an increasing trend in the short term and a decreasing trend in the long term. It is important to note that short-term reactions, such as cation exchange, altered the contaminated soil structure to a flocculated form, resulting in a larger grain size and subsequently increased void ratio and permeability. In contrast, during long-term reactions, the formation of a cementitious gel filled the voids, thereby enhancing the resistance of the samples to external loads.

For future research, it is recommended to perform microstructural analyses, such as scanning electron microscopy (SEM), energy-dispersive X-ray spectroscopy (EDS), Fourier-transform infrared spectroscopy (FTIR), or X-ray diffraction (XRD), to provide direct evidence of mechanisms like pozzolanic reactions, flocculation, and cementitious gel formation, and to further understand and validate the processes involved in soil stabilization.

Statements & Declarations

Author contributions

Arvin Monjezi: Investigation, Formal analysis, Data curation, Software, Writing - Original Draft.

Hamed Ahmadi Chenarboni: Project administration, Resources, Writing - Review & Editing.

Hossein MolaAbasi: Conceptualization, Methodology, Software, Writing - Review & Editing.

Funding

The authors received no financial support for the research, authorship, and/or publication of this article.

Data availability

The data presented in this study will be available on interested request from the corresponding author.

Declarations

The authors declare no conflict of interest.

References

[1] Moayedi, H., Mosallanezhad, M., Nazir, R., Kazemian, S., Huat, B. K. Peaty Soil Improvement by Using Cationic Reagent Grout and Electrokintic Method. Geotechnical and Geological Engineering, 2014; 32: 933–947. doi:10.1007/s10706-014-9770-7.

[2] Waleed, M., Alshawmar, F. Enhancing mechanical properties of low plasticity soil through coal and silica fume stabilization. Scientific Reports, 2025; 15: 9990. doi:10.1038/s41598-025-94149-0.

[3] Lahoori, M., Rosin-Paumier, S., Masrouri, F. Effect of monotonic and cyclic temperature variations on the mechanical behavior of a compacted soil. Engineering Geology, 2021; 290: 106195. doi:10.1016/j.enggeo.2021.106195.

[4] Karthick, A., Roy, B., Chattopadhyay, P. A review on the application of chemical surfactant and surfactant foam for remediation of petroleum oil contaminated soil. Journal of Environmental Management, 2019; 243: 187–205. doi:10.1016/j.jenvman.2019.04.092.

[5] Oluwatuyi, O. E., Ojuri, O. O., Khoshghalb, A. Cement-lime stabilization of crude oil contaminated kaolin clay. Journal of Rock Mechanics and Geotechnical Engineering, 2020; 12: 160–167. doi:10.1016/j.jrmge.2019.07.010.

[6] Petrillo, A., Di Chiara, G., Acampora, A., Fraternali, F., Farina, I. Application of stabilized contaminated soils as metaconcrete aggregates. Meccanica, 2025; 60: 3353–3363. doi:10.1007/s11012-025-01999-z.

[7] Shah, S. J., Shroff, A. V., Patel, J. V., Tiwari, K. C., Ramakrishnan, D. Stabilization of fuel oil contaminated soil—A case study. Geotechnical & Geological Engineering, 2003; 21: 415–427. doi:10.1023/B:GEGE.0000006052.61830.1a.

[8] Das, S., Kuppanan, N., Channashettar, V. A., Lal, B. Remediation of Oily Sludge- and Oil-Contaminated Soil from Petroleum Industry: Recent Developments and Future Prospects. 1st ed. Singapore: Springer Singapore; 2018. doi:10.1007/978-981-10-6178-3_9.

[9] Rajabi, H., Sharifipour, M. An Experimental Characterization of Shear Wave Velocity (Vs) in Clean and Hydrocarbon-Contaminated Sand. Geotechnical and Geological Engineering, 2017; 35: 2727–2745. doi:10.1007/s10706-017-0274-0.

[10] Li, Y., Zeng, X., Zhou, J., Liu, H., Gu, Y., Pan, Z., Zeng, Y., Zeng, Y. Incorporation of disposed oil-contaminated soil in cement-based materials. Resources, Conservation and Recycling, 2020; 160: 104838. doi:10.1016/j.resconrec.2020.104838.

[11] Li, M., Ma, C., Sun, Z. M., Yao, X. Y. Mechanical properties distribution of lime-fly ash solidified oil contaminated soil in a coastal environment. European Journal of Environmental and Civil Engineering, 2022; 26: 3027–3042. doi:10.1080/19648189.2020.1781695.

[12] Shahidi, M., Farrokhi, F., Asemi, F. Experimental study of the effect of adding clay nanoparticles to improve strength properties of contaminated clayey-sand soil with gasoil. Amirkabir Journal of Civil Engineering, 2020; 51: 1145–1162. doi:10.22060/ceej.2018.14287.5612.

[13] Mekkiyah, H. M., Al-Hamadani, Y. A. J., Abdulhameed, A. A., Resheq, A. S., Mohammed, Z. B. Effect of Crude Oil on the Geotechnical Properties of Various Soils and the Developed Remediation Methods. Applied Sciences, 2023; 13: 9103. doi:10.3390/app13169103.

[14] Vakili, A. H., Selamat, M. R. B., Salimi, M., Gararei, S. G. Evaluation of pozzolanic Portland cement as geotechnical stabilizer of a dispersive clay. International Journal of Geotechnical Engineering, 2021; 15: 504–511. doi:10.1080/19386362.2019.1583515.

[15] Jayakrishnan, V., Gracious, A., Shaju, A. C. Effect of Fly Ash on Geotechnical Properties of Oil-Contaminated Soil. In: Advances in Civil Engineering; 2021 Sep 21–22; Singapore, Republic of Singapore. p. 219–232.

[16] Salimi, M., Dordsheykhtorkamani, A., Afrasiabian, A., Khajeh, A. Incorporation of Volcanic Ash for Enhanced Treatment of a Cement-Stabilized Clayey Soil. Journal of Materials in Civil Engineering, 2021; 33: 04020465. doi:10.1061/(ASCE)MT.1943-5533.0003571.

[17] Ghorbani, A., Hasanzadehshooiili, H., Mohammadi, M., Sianati, F., Salimi, M., Sadowski, L., Szymanowski, J. Effect of Selected Nanospheres on the Mechanical Strength of Lime-Stabilized High-Plasticity Clay Soils. Advances in Civil Engineering, 2019; 2019: 4257530. doi:10.1155/2019/4257530.

[18] Goodarzi, A. R., Salimi, M. Effect of iron industry slags on the geotechnical properties and mineralogy characteristics of expansive clayey soils. Modares Journal of Civil Engineering, 2015; 15: 160–170.

[19] Afrasiabian, A., Salimi, M., Movahedrad, M., Vakili, A. H. Assessing the impact of GBFS on mechanical behaviour and microstructure of soft clay. International Journal of Geotechnical Engineering, 2021; 15: 327–337. doi:10.1080/19386362.2019.1565393.

[20] van Deventer, J. S. J., Provis, J. L., Duxson, P., Brice, D. G. Chemical Research and Climate Change as Drivers in the Commercial Adoption of Alkali Activated Materials. Waste and Biomass Valorization, 2010; 1: 145–155. doi:10.1007/s12649-010-9015-9.

[21] Goodarzi, A. R., Akbari, H. R., Salimi, M. Enhanced stabilization of highly expansive clays by mixing cement and silica fume. Applied Clay Science, 2016; 132-133: 675–684. doi:10.1016/j.clay.2016.08.023.

[22] Mehta, A., Ashish, D. K. Silica fume and waste glass in cement concrete production: A review. Journal of Building Engineering, 2020; 29: 100888. doi:10.1016/j.jobe.2019.100888.

[23] Fan, Y., Yang, Y., Niu, B., Liu, Z., Dan, J., Wang, J. Synthesis of sodium silicate using industrial by-products glauber's salt and microsilica: Effective reuse of the waste. Waste Management, 2021; 131: 359–367. doi:10.1016/j.wasman.2021.06.026.

[24] Yang, Q., Du, C. Experimental Study on the Effect of Plant Ash on Soft Clay Stabilized with Cement-Based Composites. Geotechnical and Geological Engineering, 2021; 39: 105–117. doi:10.1007/s10706-020-01476-2.

[25] Zaini, M. S. I., Suwito, A. R., Hasan, M., Zolkepli, M. F., Abu Talib, Z. Effect of Silica Fume as Industrial Byproduct on the Stabilization of Kaolin Clay Soil. International Journal of Sustainable Construction Engineering and Technology, 2025; 16: 349–364.

[26] Kulanthaivel, P., Krishnaraja, A. R., Muthusamy, S., Mishra, O. P., Sha, M. S., Sadasivuni, K. K. An Experimental Analysis of Precipitated Silica in Petroleum-Contaminated Clay for the Strengthening of Soil Characteristics. Iranian Journal of Science and Technology, Transactions of Civil Engineering, 2024; 48: 1573–1579. doi:10.1007/s40996-023-01242-3.

[27] Naeini, S., Shahabivand, P. Influence of nano-silica stabilization on the shear strength behavior of crude oil–contaminated silty sand. GeoStruct Innovations, 2025; 3: 13–28. doi:10.56578/gsi030102.

[28] Kalkan, E., Akbulut, S. The positive effects of silica fume on the permeability, swelling pressure and compressive strength of natural clay liners. Engineering Geology, 2004; 73: 145–156. doi:10.1016/j.enggeo.2004.01.001.

[29] Kalkan, E. Influence of silica fume on the desiccation cracks of compacted clayey soils. Applied Clay Science, 2009; 43: 296–302. doi:10.1016/j.clay.2008.09.002.

[30] Kalkan, E. Impact of wetting–drying cycles on swelling behavior of clayey soils modified by silica fume. Applied Clay Science, 2011; 52: 345–352. doi:10.1016/j.clay.2011.03.014.

[31] Phanikumar, B. R., m, J. R., e, R. R. Silica fume stabilization of an expansive clay subgrade and the effect of silica fume-stabilised soil cushion on its CBR. Geomechanics and Geoengineering, 2020; 15: 64–77. doi:10.1080/17486025.2019.1620348.

[32] Abdelhalim, R. A., El Sawwaf, M., Nasr, A. M., Farouk, A. Experimental and numerical studies of laterally loaded piles located near oil-contaminated sand slope. Engineering Science and Technology, an International Journal, 2020; 23: 744–757. doi:10.1016/j.jestch.2020.03.001.

[33] Portelinha, F. H. M., De Souza Correia, N., Santos Mendes, I., Silva, J. W. B. D. Geotechnical Properties and Microstructure of a Diesel Contaminated Lateritic Soil Treated with Lime. Soil and Sediment Contamination: An International Journal, 2021; 30: 838–861. doi:10.1080/15320383.2021.1893648.

[34] Sarker, D., Shahrear Apu, O., Kumar, N., Wang Jay, X., Lynam Joan, G. Application of Sustainable Lignin Stabilized Expansive Soils in Highway Subgrade. 1st ed. Reston (VA): American Society of Civil Engineers (ASCE); 2021. doi:10.1061/9780784483435.033.

[35] Changizi, F., Haddad, A. Improving the geotechnical properties of soft clay with nano-silica particles. Proceedings of the Institution of Civil Engineers - Ground Improvement, 2017; 170: 62–71. doi:10.1680/jgrim.15.00026.

[36] Casagrande, A., Fadum, R. E. Notes on soil testing for engineering purposes. 1st ed. Cambridge (MA): Harvard University, Graduate School of Engineering; 1940.

[37] Ali, N., Kumar, D. A., Pathan, D. A. F. H. Effect of Soil Stabilizers on Consolidation Characteristics of Compacted Clay. Engineering Science and Technology International Research Journal, 2019; 3: 1–12.

[38] Asadoullahtabar, S. R., Asgari, A., Mohammad Rezapour Tabari, M. Assessment, identifying, and presenting a plan for the stabilization of loessic soils exposed to scouring in the path of gas pipelines, case study: Maraveh-Tappeh city. Engineering Geology, 2024; 342: 107747. doi:10.1016/j.enggeo.2024.107747.

Civil Engineering and Applied Solutions

Research Article

journal homepage: ceas.journals.umz.ac.ir

CEAS Civil Engineering and Applied Solutions

Earthquake-Induced Deformation of Road Embankments: A Finite Difference Method

Vahid Sadeghi [a], Mohsen Bagheri [b*], Jaber Abasi Hamidi [a]

[a] *Department of Civil Engineering, Saroyeh Institute of Education, Sari, Iran*
[b] *Faculty of Civil Engineering, Babol Noshirvani University of Technology, Babol, Iran*

ARTICLE INFO

Keywords:
Road embankments
Seismic performance
Dynamic numerical analysis
Soil liquefaction
FLAC

Article history:
Received 15 December 2025
Accepted 23 April 2026
Available online 01 October 2026

ABSTRACT

This paper presents a numerical study on the seismic performance of road embankments using finite difference modeling implemented in FLAC. Nonlinear dynamic analyses are conducted to quantify the effects of critical seismic parameters, including peak ground acceleration (PGA) and thickness of liquefiable soil on deformation patterns and settlement behavior of embankments. The results demonstrate that elevated groundwater conditions and the onset of soil liquefaction markedly intensify permanent deformations and compromise global stability. Maximum displacements are predominantly generated during the strong-motion phase of the earthquake, followed by a degree of post-shaking stabilization that is strongly governed by soil mechanical properties. The induced deformations may lead to longitudinal and transverse cracking, reduction in effective embankment height, and progressive modification of slope geometry, thereby impairing structural integrity and traffic safety. The study highlights the importance of incorporating seismic frequency content, coupled hydro-geotechnical conditions, and soil strength characteristics into the seismic design, evaluation, and rehabilitation of road embankments in earthquake-prone areas. The findings contribute to improving predictive assessments and offer practical implications for enhancing the seismic resilience of transportation infrastructure.

1. Introduction

Iran is situated within the Alpine–Himalayan seismic belt, one of the most tectonically active regions in the world, and is therefore repeatedly subjected to moderate to strong earthquakes. Numerous historical and recent seismic events have resulted in extensive damage to transportation infrastructure, particularly road embankments, which constitute a fundamental component of road networks. The seismic vulnerability of these earth structures poses a serious challenge, as their failure can severely impair traffic circulation, delay emergency operations, and hinder post-earthquake recovery.

Road embankments are commonly constructed to overcome complex topographical conditions, provide grade separation, and ensure continuity of transportation corridors. Under seismic loading, however, these structures are exposed to inertial forces, cyclic shear stresses, and excess pore water pressure generation, which may lead to large permanent deformations, slope instability, and in severe cases, liquefaction-induced failure. Previous studies have shown that earthquake-induced damage to embankments can cause disruptions comparable to, or even exceeding, those observed in structural roadway elements such as bridges and pavements, particularly when constructed on soft or saturated soils [1, 2]. Field evidence from major earthquakes, including the Bam (2003), East Azerbaijan (2012), and Kermanshah (2017) events, has highlighted the susceptibility of Iranian road embankments to seismic loading. In many cases, embankments are founded on weak or fine-grained soils with high plasticity, especially along rural and

* Corresponding author.
E-mail addresses: m.bagheri@stu.nit.ac.ir (M. Bagheri).

https://doi.org/10.22080/ceas.2026.30800.1066
ISSN: 3092-7749/
How to cite this article: Sadeghi, V., Bagheri, M., Abasi Hamidi, H. Earthquake-Induced Deformation of Road Embankments: A Finite Difference Method. Civil Engineering and Applied Solutions. 2026; 2(4): 28–41. doi:10.22080/ceas.2026.30800.1066.

secondary road networks where locally available materials are widely used. Although these soils may perform adequately under static conditions, their stiffness and shear strength can degrade significantly during seismic shaking, resulting in excessive settlement, cracking, and loss of stability. The challenge of improving embankment performance in seismic regions is further compounded by economic, environmental, and geographical constraints. Large-scale replacement of weak soils or extensive structural interventions are often impractical. Consequently, there is a growing need for efficient and sustainable solutions that enhance the dynamic behavior of embankments while minimizing construction costs and environmental impacts. Soil stabilization and reinforcement techniques, including chemical additives, geosynthetics, and innovative eco-friendly materials, have emerged as promising approaches to mitigate seismic-induced deformations and improve overall stability. Despite existing research, there remains a need for comprehensive numerical investigations that explicitly account for dynamic loading characteristics, groundwater conditions, and soil improvement measures within a unified framework. In this study, the seismic response of road embankments under dry and saturated conditions is examined through advanced finite difference modeling using FLAC. The primary objective is to evaluate the effectiveness of selected stabilization strategies in reducing permanent deformations and enhancing embankment resilience under earthquake loading. The outcomes of this research aim to provide practical insights and design-oriented guidance for improving the seismic performance of road embankments, thereby contributing to the resilience and sustainability of transportation infrastructure in earthquake-prone regions.

2. Literature review

Earthquake-induced permanent deformations in road embankments are commonly attributed to several fundamental mechanisms, which may act independently or simultaneously depending on the soil conditions and seismic characteristics. These mechanisms can be broadly classified into compaction, lateral spreading, and global instability, as schematically illustrated in Fig. 1. Each mechanism reflects a distinct mode of soil response and deformation pattern under cyclic loading. Global instability is typically associated with the localization of shear and deviatoric strains along a well-defined failure surface, leading to large-scale slope failure or rotational sliding. In contrast, compaction and lateral spreading are characterized by more diffuse deformation processes. Compaction involves volumetric strain accumulation caused by cyclic densification of loose soils, whereas lateral spreading results from plastic shear deformations that develop over a wider zone, often triggered or amplified by excess pore water pressure generation. These mechanisms lead to progressive settlement, horizontal displacement, and gradual alteration of the embankment geometry rather than abrupt collapse. A clear distinction between these deformation modes is essential for accurate seismic performance evaluation and for the development of effective mitigation and retrofitting strategies. Failure to identify the dominant mechanism may result in inadequate design solutions or underestimation of seismic risk. Post-earthquake reconnaissance studies and documented case histories provide valuable insights into these behaviors. Representative examples of road embankment failures observed during various seismic events are presented in Figs. 2–7 [3, 4], illustrating the range of damage severity and the influence of local soil conditions, groundwater levels, and earthquake characteristics. Previous studies have emphasized that the interaction between seismic loading parameters and site-specific geotechnical conditions governs the dominant deformation mechanism and the resulting embankment response. Consequently, advanced numerical modeling and well-calibrated analytical approaches are increasingly employed to capture these complex behaviors and to improve the reliability of seismic assessment methods for road embankments.

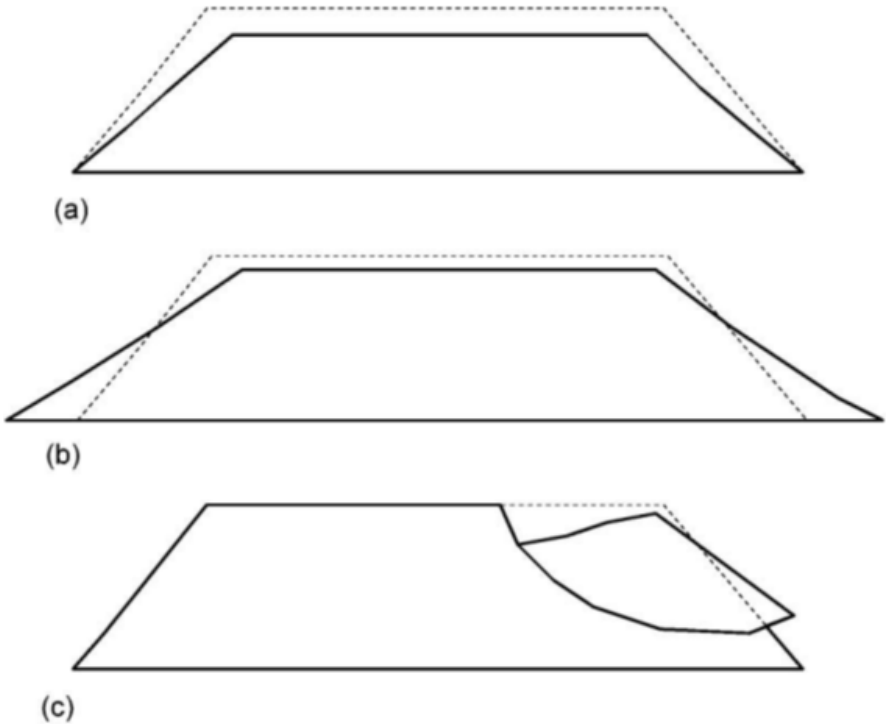

Fig. 1. Conceptual illustration of permanent deformation mechanisms in road embankments subjected to seismic loading: (a) volumetric compaction, (b) lateral spreading, and (c) global slope instability. Dashed outlines represent the initial (undeformed) configuration, while solid outlines indicate the post-earthquake deformed geometry.

Fig. 2. Vertical cracking observed along road alignments following the Haiti earthquake.

Fig. 3. Permanent embankment displacements near an overpass caused by the 1980 Irpinia earthquake, Lioni, Italy.

Fig. 4. Surface cracking on a road embankment after the 1980 Irpinia earthquake, Lioni, Italy.

Fig. 5. Vertical cracking in a road embankment during the Haiti earthquake.

Fig. 6. Shear failure in a road embankment during the 2010 Chile earthquake, showing notable lateral pavement displacement.

Fig. 7. Longitudinal cracking in a road embankment during the Peru earthquake, reflecting tensile stresses along the road axis.

In recent years, extensive numerical research has been devoted to improving the understanding of the seismic behavior of road embankments, particularly in regions characterized by high seismicity and soils prone to liquefaction. Strong ground motions can induce significant degradation of soil shear strength, generate excess pore water pressures, and result in large permanent settlements and lateral displacements. These complex soil–structure interactions highlight the necessity for reliable seismic performance assessment frameworks and resilient design methodologies for transportation infrastructure.

Khalil et al. [5] developed numerical fragility curves for highway embankments using a multi-mechanism elasto-plastic constitutive formulation. In their study, embankment settlement was adopted as the damage variable, while peak ground acceleration (PGA) served as the intensity measure, enabling a probabilistic evaluation of seismic vulnerability. Similarly, Oblak et al. [6] employed the advanced PM4Sand constitutive model to simulate liquefaction-induced deformations, using permanent settlement at the embankment crest as a damage index. Their results demonstrated that the use of state-of-the-art constitutive models significantly enhances the accuracy of predicting embankment response under earthquake loading, particularly in liquefiable soil conditions.

Further investigations have focused on the performance of the UBC3D-PLM model in capturing the dynamic response of embankments subjected to seismic excitation. Studies by Chakraborty and Sawant [7] confirmed the capability of this constitutive model to realistically reproduce key mechanisms such as dilation, cyclic mobility, and permanent deformation in sandy and silty deposits. These findings underscore the robustness of UBC3D-PLM as an effective numerical tool for simulating complex soil behavior and evaluating embankment performance in earthquake-prone environments.

At the network level, one of the most comprehensive efforts to date is the REDARS 2 framework, developed through a collaborative initiative between the Multidisciplinary Center for Earthquake Engineering Research (MCEER) and the Federal Highway Administration (FHWA). Introduced in 2006, REDARS 2 provides a systematic methodology and software platform for seismic risk assessment of highway systems. The framework integrates regional seismic hazard analysis, component-level damage modeling for bridges, roadways, tunnels, and embankments, and traffic network simulation to quantify post-earthquake disruptions. While REDARS 2 has been primarily calibrated for regions such as California, its development highlighted the critical need for region-specific seismic risk assessment tools that reflect local geotechnical conditions and seismic characteristics. El-Maissi et al. [8] indicated that road networks are critical components of transportation infrastructure, essential for economic and social development, and must maintain functionality during and after seismic events. Recent research has focused on assessing the vulnerability of road networks and their assets, examining damage states and associated impacts. Two main approaches have been employed: physical-based methods, including fragility functions and vulnerability indices, and traffic-based methods, emphasizing accessibility and link importance. This review highlights the strengths and limitations of these methodologies, identifies key research gaps, and provides directions for future studies on seismic resilience of road networks. El-Maissi et al. [9] investigated that urban road networks are key components of resilient infrastructure, requiring robust performance during earthquakes. Previous studies often focused on single-criterion physical vulnerability, neglecting interactions with surrounding built environments. This research introduces an integrated approach using two Vulnerability Indexes: Intrinsic Seismic Vulnerability (ISVI) for direct roadway damage and Eccentric Seismic Vulnerability (ESVI) for impacts from adjacent building damage. The combined assessment enhances emergency planning and accessibility to critical services, providing a comprehensive tool for urban resilience and risk mitigation.

Yildirim et al. [10] indicated that Seismic events pose critical risks to urban road infrastructure, affecting both road networks and adjacent buildings. This study proposes an integrated vulnerability assessment using an Interval-valued Fermatean fuzzy Analytic Hierarchy Process, combining quantitative and qualitative criteria to evaluate risk for each road segment. The methodology captures interactions between damaged buildings, road networks, and disaster response, enhancing preparedness and mitigation strategies. Case studies in Istanbul and Gölbaşı, Türkiye, validate the approach and demonstrate its effectiveness in identifying high-risk areas and supporting resilient urban infrastructure planning. Broniewicz and Ogrodnik [11] reviewed recent literature on multi-criteria decision-making (MCDM/MCDA) in the transport sector, highlighting popular methods and emerging research trends from 2021 to 2024. A case study on a road investment in Poland demonstrates the application of different criteria weighting techniques, including AHP, Fuzzy AHP, and CRITIC. The TOPSIS method was employed to rank project alternatives, with results compared to official design documentation. The findings illustrate the effectiveness of MCDM approaches for transport decision-making and emphasize the influence of weighting methods on project evaluation outcomes.

Overall, the existing body of literature demonstrates significant progress in modeling and assessing the seismic performance of road embankments [12-15]. However, there remains a clear need for comprehensive numerical studies that integrate advanced constitutive models, site-specific soil conditions, groundwater effects, and realistic seismic inputs within a unified framework. Addressing these gaps is essential for improving the reliability of embankment performance predictions and for developing practical design and retrofit strategies tailored to seismically active regions such as Iran. Despite the substantial advances reported in the literature, several critical gaps remain in the seismic assessment of road embankments. Most existing studies focus either on fragility-based evaluations or on advanced constitutive modeling without systematically investigating the combined influence of seismic intensity measures, frequency content, groundwater conditions, and soil improvement strategies within a unified numerical framework. In particular, the coupled effects of groundwater level variations and liquefaction susceptibility on permanent embankment deformations under realistic earthquake records have received limited attention. To address these gaps, the present study employs advanced finite difference modeling to investigate the seismic response of road embankments under both dry and saturated conditions, explicitly accounting for key earthquake characteristics and soil behavior. The novelty of this research lies in the integrated evaluation of embankment deformation mechanisms, liquefaction effects, and stabilization measures, providing design-oriented insights that contribute to the development of more resilient and region-specific seismic design and retrofitting guidelines for transportation infrastructure.

3. Numerical simulation

3.1. Static analysis

The seismic response of the material and its tendency for strain softening are largely governed by its initial stress state and inherent properties [16]. To simulate a steady-state free-field condition, the model is initialized with geostatic stresses assigned to each grid zone, which allows the system to achieve equilibrium through mechanical computations. In the static analysis, the road embankment was subjected exclusively to gravitational loading. The base of the model was fully constrained in all directions, while the lateral boundaries were restricted along the x-axis. It is essential to disable the flow calculation feature during this stage. Moreover, to avoid coupling effects between pore pressure and volumetric deformation, the bulk modulus of water was set to zero.

3.2. Dynamic analysis

Following the static analysis under effective stress conditions, the dynamic response of the embankment system was investigated through the following procedure:

Step 1 – Baseline Correction

Prior to applying the horizontal components of the earthquake records, baseline correction of the acceleration histories was performed. Direct double integration of uncorrected acceleration often results in residual displacements at the end of the motion. To address this, a low-frequency adjustment was added to the input ground motion, ensuring that the final displacement returns to zero.

Step 2 – Wave Propagation Considerations

Accurate wave propagation is critical in dynamic simulations. Errors may arise if the numerical grid does not appropriately capture the highest shear wave frequencies of the soil. The finite difference grid spacing was determined based on the maximum allowable shear wave frequency, f, calculated as [16]:

$$f = \frac{c_s}{10\Delta l} \tag{1}$$

where

c_s is the shear wave velocity of the soil, and Δl represents the largest grid dimension. A uniform grid size of 1 m × 1 m was adopted, resulting in a maximum permissible frequency of 5 Hz corresponding to the slowest soil layers. To ensure numerical stability, the input earthquake records were filtered with a low-pass filter set to 4 Hz, accounting for potential reductions in shear wave velocity due to plastic deformation during seismic loading.

Step 3 – Dynamic Boundary Conditions: Kuhlemeyer RL, Lysmer

To simulate free-field conditions at the model boundaries, free-field boundary conditions were applied laterally, while absorbing boundaries were implemented to emulate the outward propagation of waves at the base. The viscous boundaries developed by Kuhlemeyer Roger and Lysmer [17] were utilized to effectively absorb outgoing waves, thus approximating half-space behavior. The horizontal components of acceleration records from the Imperial Valley, Kobe Port Island, and Kocaeli earthquakes were applied at the model base. These accelerations were converted into equivalent shear stress waves following the procedure described in FLAC [16].

Step 4 – Rayleigh Damping Implementation

Rayleigh damping, comprising two frequency-dependent viscous components, was applied to all model elements. By selecting an appropriate center frequency, damping can be maintained nearly constant across a range of frequencies surrounding this point [16]. The center frequency was chosen between the natural frequency of the system and the predominant frequency of the input motion, and a damping ratio of 5% was assigned. Dynamic simulations were then performed, and the responses were recorded for subsequent interpretation and assessment.

3.3. Equilibrium equations and constitutive model

In more general situations for which the soil is not in static equilibrium, for example, during seismic wave propagation, the governing equations are the equations of motion. The dynamic analyses were conducted as fully non-linear elasto-plastic two-dimensional coupled stress-flow analyses with coupled liquefaction triggering using the Fast Lagrangian Analysis of Continua (*FLAC*) [16]. In *FLAC*, calculation of displacements and pore pressure is carried out by solving a coupled system of equations, including the motion equation and the diffusion equation. In this code, saturated soil is treated as a two-phase material. Biot coupled equations were used for the soil and water phases. Pore pressure generation is incremental and fully integrated with the nonlinear dynamic analyses. During dynamic analyses, pore fluid simply responds to changes in pore volume caused by mechanical dynamic loading. The average pore pressure does not vary significantly during the analysis. It is known, however, that pore pressure may build up considerably during cyclic shear loading. It is important to incorporate this physical process in the coupled nonlinear dynamic analysis. Martin Geoffrey et al. [18] proposed the following empirical equation that relates the increment of volume decrease,$\Delta\varepsilon_{vd}$, to the cyclic shear-strain amplitude,γ:

$$\Delta\varepsilon_{vd} = c_1(\gamma - c_2\varepsilon_{vd}) + \frac{c_2\varepsilon_{vd}^2}{\gamma - c_4\varepsilon_{vd}} \tag{2}$$

Byrne [19] proposed a modified two-parameter effective stress model (Eq. 3).

$$\frac{\Delta\varepsilon_{vd}}{\gamma} = c_1 exp\left(-c_2\left(\frac{\varepsilon_{vd}}{\gamma}\right)\right) \tag{3}$$

Where c_1 and $c_2$are constants with different interpretations from Eq. (3), c_1 can be derived from relative density, D_r, as follows:

$$c_1 = 7600(D_r)^{-2.5} \tag{4}$$

$$c_2 = \frac{0.4}{c_1} \tag{5}$$

Further, Byrne [19] represented an empirical relation between D_r and a normalized standard penetration test $(N_1)_{60}$ values.

$$D_r = 15\ (N_1)_{60}^{0.5} \quad (6)$$

$$c_1 = 8.7\ (N_1)_{60}^{-1.25} \quad (7)$$

The above mentioned formulation is available in FLAC as a built-in model and was adopted in this study along with a bilinear, elastic- perfectly plastic stress–strain relationship and Rayleigh damping. Therefore, during dynamic analysis, as effective stresses decrease with increase in pore pressure, the soil begins to yield and increments of permanent deformation are accumulated.

3.4. Numerical modeling of seismic response of road embankments on liquefiable soils

Numerical analyses of the road embankments were conducted using the finite difference software FLAC [16] to investigate their seismic response on liquefiable soils. The main objective of the simulations was to quantify embankment deformation and stability under dynamic earthquake loading conditions. The embankment was founded on a 10 m thick layer of loose sand with a relative density of 30% (D_r = 30%), modeled as a homogeneous, cohesionless material following the Mohr–Coulomb failure criterion. This liquefiable sand layer was placed atop a dense gravelly stratum representing the underlying foundation soil, based on geotechnical site investigations. To capture realistic pore pressure effects, the water table was gradually raised to exceed the sand layer, ensuring full saturation of the liquefiable soil. The material parameters for both the soils are summarized in Table 1. The numerical model setup allowed for an explicit evaluation of liquefaction-induced settlements, lateral spreading, and potential slope instabilities under prescribed earthquake motions, providing insights into the coupled behavior of embankments and their supporting soils during seismic events.

Table 1. Material properties of the road embankment and foundation soils used in the seismic analysis.

Material type	Υ_{dry} (kg/m^3)	Υ_{sat} (kg/m^3)	φ	C (KPa)	ψ	v	K (m/s)	n	E (KPa)	$N_{1(60)}$
Road embankments	17	19	32	1	2	0.25	1×10^{-3}	0.35	8×10^4	16
Sand	16	18	25	0	0	0.3	1×10^{-6}	0.44	2×10^4	10
Dense gravelly soil	19	21	38	0	8	0.25	1×10^{-7}	0.24	1.2×10^4	45

The finite difference model of the road embankment and underlying soil layers is illustrated in Fig. 8. To represent the seismic response of the liquefiable silt layer, the Finn constitutive model was employed. This model incorporates a coupled effective stress framework, combining the Mohr–Coulomb failure criterion with volumetric strain–based pore water pressure generation, enabling a realistic simulation of liquefaction-induced behavior. Boundary conditions were applied by fully restraining displacements at the base of the model, while the embankment and soil layers were allowed to deform freely elsewhere. Prior to applying dynamic earthquake excitations, the model was brought to static equilibrium to ensure a stable initial stress state. This approach allowed for a robust evaluation of embankment settlements, lateral spreading, and slope stability under seismic loading, capturing the coupled interaction between the embankment and the liquefiable foundation soils.

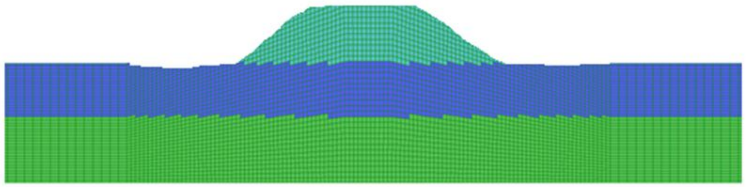

Fig. 8. Schematic geometry and finite difference mesh of the road embankment model used in the seismic analysis.

Each numerical model was subjected to earthquake excitation derived from a scaled record of the Kobe earthquake (1995), Northridge (1994), and Loma Prieta (1989) (Fig. 9). The selected ground motion records were obtained from the PEER Strong Motion Database, as summarized in Table 2. The analyses focused on evaluating the seismic response of the embankments by monitoring the evolution of excess pore water pressure ratios ($r_u = \Delta u/\sigma_0$), as well as horizontal and vertical displacements at the crest and along the slopes. This approach enabled a detailed assessment of embankment deformation mechanisms and liquefaction-induced effects under realistic seismic loading conditions.

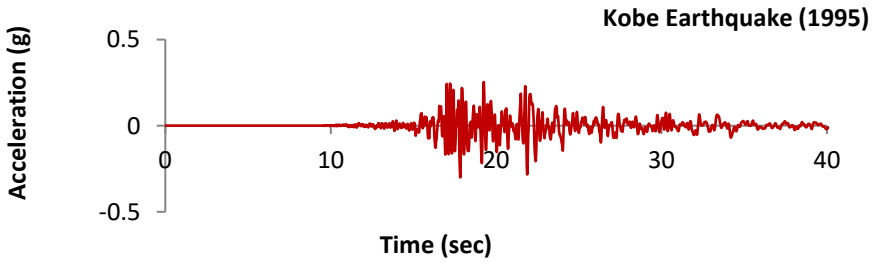

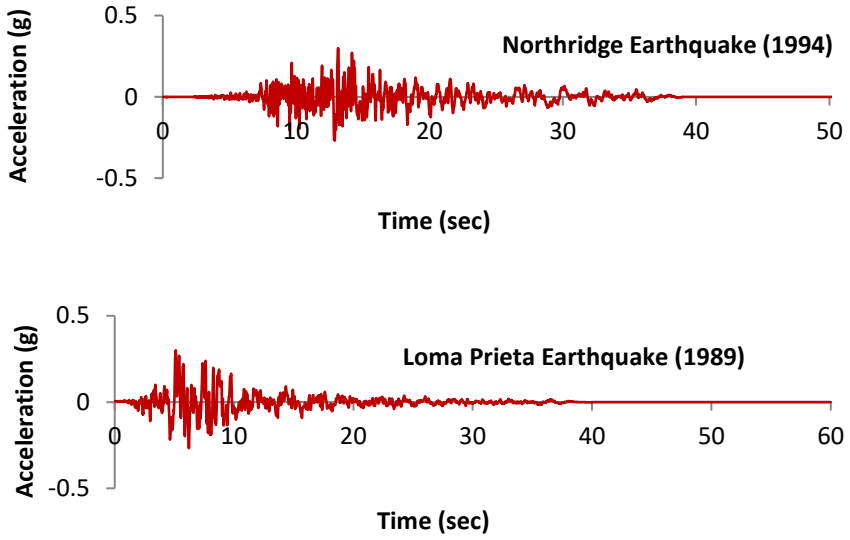

Fig. 9. Ground motion records selected for dynamic time-history analyses of the road embankment models.

Table 2. Seismic input parameters used in the numerical analysis.

Record	M_w	Predominant period, $T_p(s)$	PGA (g)	I_a (m/s)	PGA/PGA (s)	$D_{5-95}(s)$	Specific energy density $(J.m^{-2}sec^{-2})$
Elcentro (1940)	7.2	0.46	0.32	0.392 2.321 5.725	0.097	25	2170.75
Kobe (1995)	6.9	0.16	0.32	0.320 1.896 4.692	0.082	8.7	1256
Kocaeli (1999)	7.4	1.4	0.32	0.232 1.33 3.284	0.182	10	10395

3.5. Model validation

The soil behavior in this study was represented using a combination of the elasto-plastic Mohr–Coulomb model and the Finn constitutive model to capture liquefaction-induced phenomena in loose, saturated granular soils. Material properties, including bulk and shear moduli and soil density, were calibrated based on centrifuge test results to ensure realistic response under dynamic loading. Fully coupled nonlinear dynamic analyses were conducted using the explicit finite difference code FLAC (Itasca) [16], which solves a coupled system of equations encompassing both the equations of motion and pore pressure diffusion. In this framework, saturated soils are modeled as two-phase materials using Biot's theory to account for soil–water interactions. Prior to applying seismic excitation, static analyses were performed under gravity loading with fully fixed base boundaries and lateral boundaries constrained in the horizontal direction. To decouple pore pressure from mechanical volume changes, the water bulk modulus was set to zero. The cyclic pore pressure generation in the liquefiable soil was modeled following the empirical relationship proposed by Byrne [19], based on Martin Geoffrey et al. [18], which links volumetric strain increments to the amplitude of cyclic shear strain. This approach was implemented in FLAC using the built-in model along with a bilinear elastic–perfectly plastic stress–strain response and Rayleigh damping. During dynamic simulations, effective stresses decreased with increasing pore pressure, initiating soil yielding and progressive accumulation of permanent deformations. The model was validated by comparing the evolution of excess pore pressures obtained from numerical analyses with centrifuge experimental measurements (Fig. 10). The close agreement between predicted and observed pore pressure curves confirms the reliability of the numerical approach for simulating liquefaction-induced behavior and supports its application for assessing the seismic performance of road embankments founded on liquefiable soils.

4. Result and discussion

This section presents a detailed evaluation of the dynamic response of the road embankment and the underlying liquefiable soil. The analyses focus on the temporal evolution of excess pore water pressure ratios (r_u), as well as vertical and horizontal deformations, both within the free-field soil and along the embankment. By comparing the time histories at key locations, insights into the mechanisms driving embankment settlements, lateral spreading, and overall stability under seismic loading are obtained. The results are interpreted in the context of the interaction between cyclic shear stresses, pore pressure development, and the mechanical properties of the soil layers. Trends in pore pressure generation and dissipation are correlated with corresponding deformations, highlighting the influence of liquefaction on embankment performance. Furthermore, spatial variations in settlement and lateral displacement are examined to identify critical zones susceptible to instability. This comprehensive analysis provides a mechanistic understanding of the seismic behavior of embankments on liquefiable foundations and informs the effectiveness of

potential mitigation or stabilization strategies.

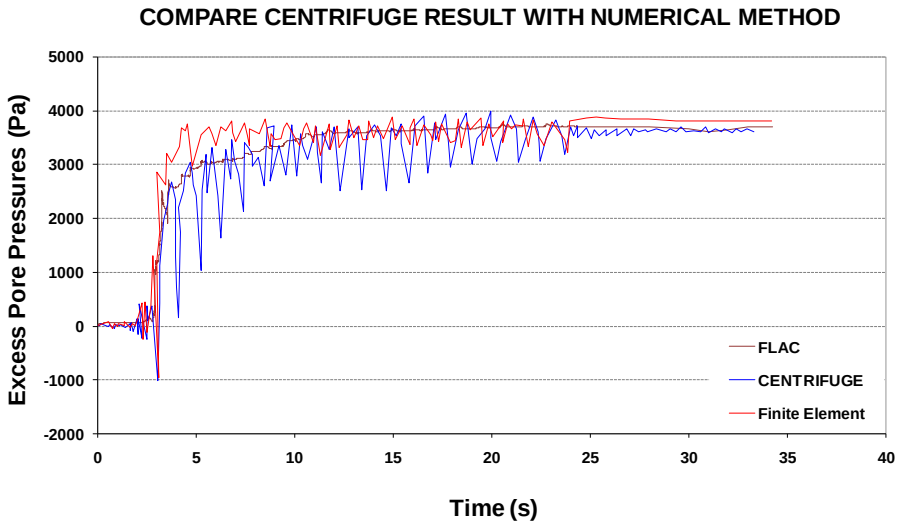

Fig. 10. Comparison of excess pore pressure evolution between centrifuge experiments and the numerical model.

4.1. Free field

The temporal variation of excess pore water pressure ratio (r_u) at different depths in the free-field soil during seismic shaking is presented in Fig. 11. The evolution of r_u is strongly influenced by the characteristics of the earthquake input, with peak values occurring during the maximum strong-motion phase, followed by gradual dissipation. These observations indicate that a substantial portion of the soil experiences a significant reduction in shear strength during the seismic event. The pronounced increase in pore pressure underscores the potential for liquefaction and associated deformations, emphasizing the need for effective mitigation strategies to safeguard the stability and integrity of road embankments constructed on such vulnerable soils.

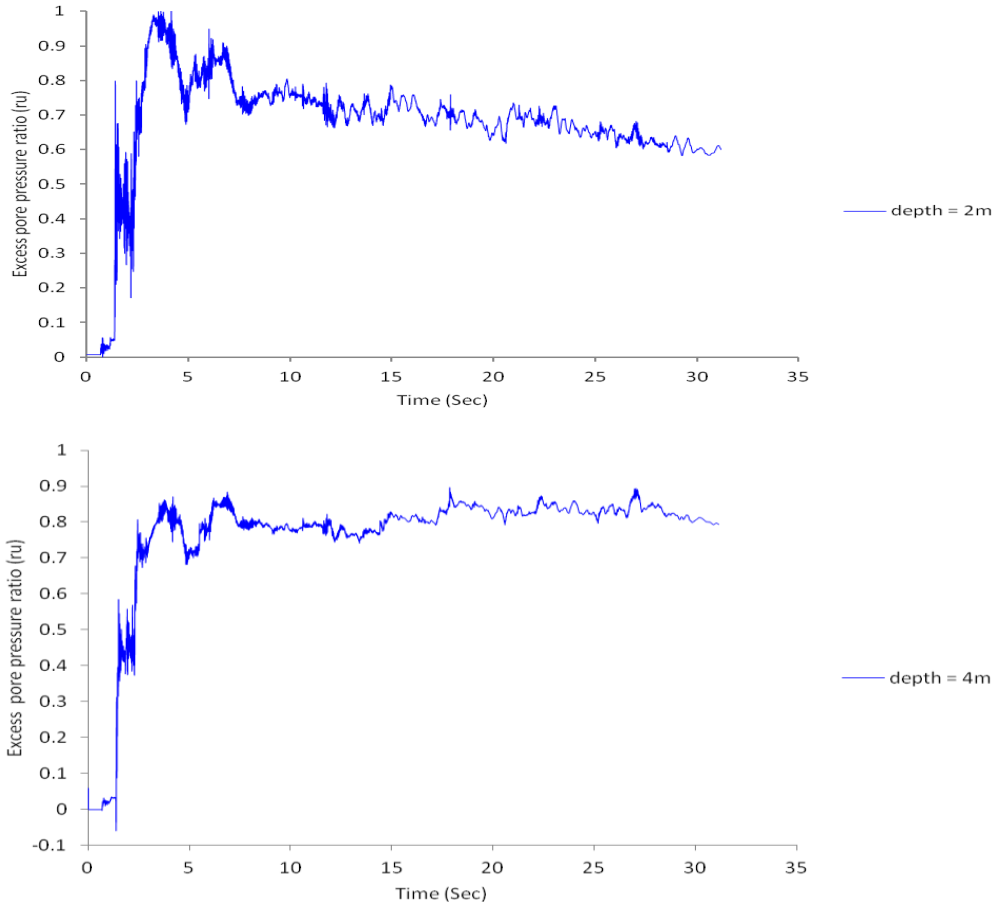

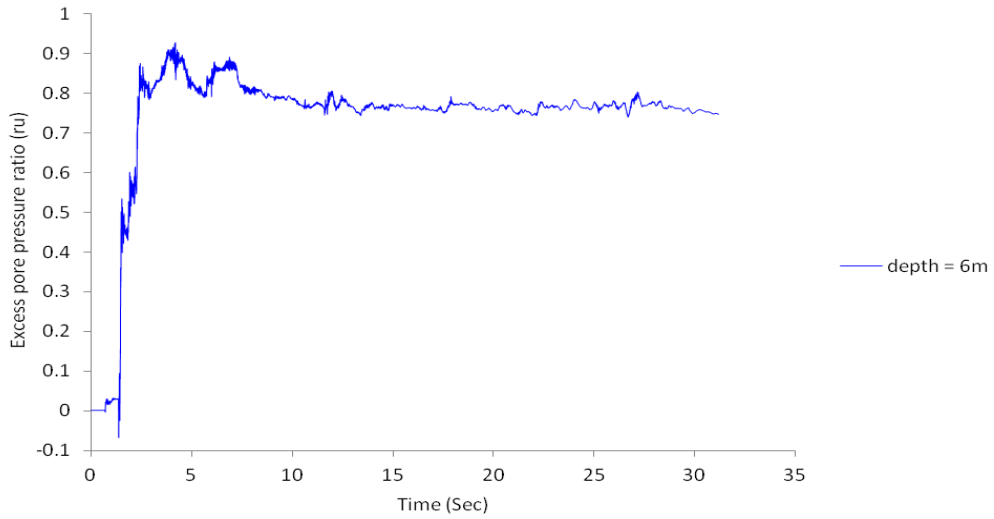

Fig. 11. Evolution of excess pore water pressure ratio at depths of 2, 4, and 6 m in the free-field soil under the Kobe earthquake (0.32 g).

4.2. Conditions of the roadway embankment during seismic loading

The dynamic response of road embankments during strong seismic events, such as the Kobe earthquake, is a critical determinant of transportation infrastructure performance. Under earthquake loading, embankments exhibit vertical settlements driven by soil densification and shear deformation, alongside horizontal displacements caused by reductions in soil shear strength. These deformations can lead to a decrease in embankment height, alterations in slope geometry, surface irregularities, and localized stress concentrations, potentially resulting in partial or localized structural failures. Additionally, asymmetric displacement patterns generate bending and torsional stresses, which further increase the susceptibility of the embankment to cracking and localized deformations (Fig. 12). To mitigate such effects, engineering interventions including dynamic compaction, soil improvement through grouting or chemical stabilizers, enhanced drainage, and resilient design strategies are recommended. The findings underscore the importance of targeted research into embankment stability under seismic excitation, particularly in regions with liquefiable or weak soils, to inform effective design, retrofitting, and risk-reduction strategies.

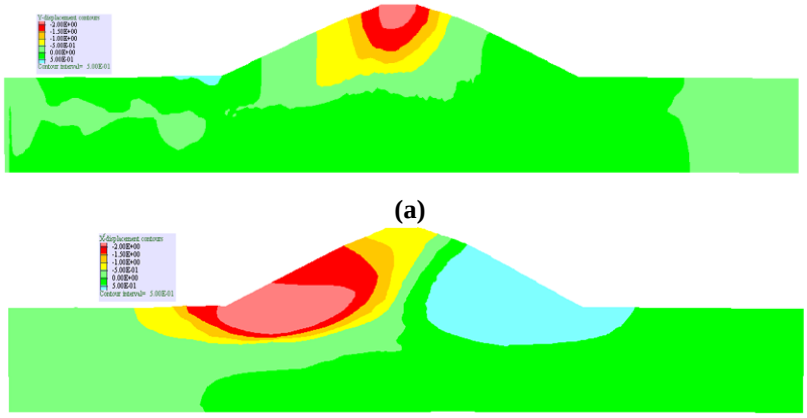

(a)

(b)

Fig. 12. Vertical settlement (a) and horizontal displacement (b) of the road embankment under the Kobe earthquake acceleration record(0.32 g).

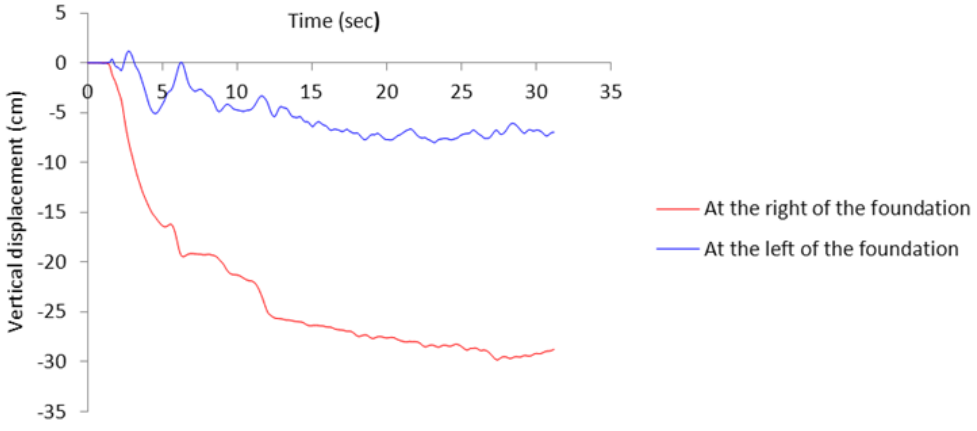

Fig. 13. Vertical settlement profile of the roadway embankment under the Kobe earthquake (0.32 g).

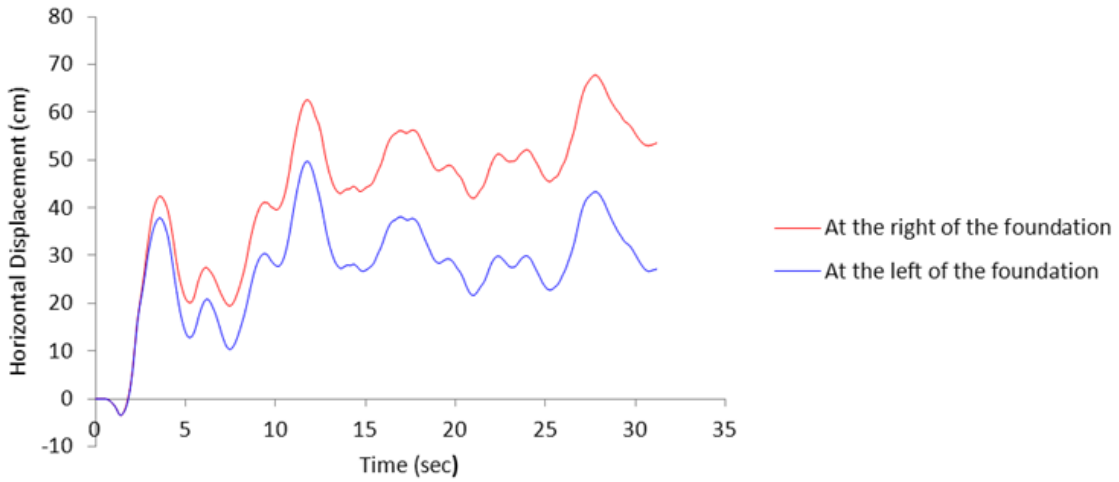

Fig. 14. Lateral displacement profile of the roadway embankment under the Kobe earthquake (0.32 g).

As illustrated in Figs. 13 and 14, the presence of liquefiable soil layers beneath the roadway embankment induces pronounced and non-uniform vertical settlements as well as lateral displacements. Such asymmetric deformations can compromise the structural integrity of the embankment, potentially causing substantial damage to the roadway foundation and affecting its serviceability. These observations highlight the critical influence of underlying soil conditions on seismic performance and underscore the need for targeted mitigation and stabilization measures in embankments constructed on liquefiable deposits.

4.3. Influence of peak ground acceleration (PGA)

The results presented in Tables 3 and 4 indicate that increases in peak ground acceleration (PGA), combined with elevated groundwater levels, substantially amplify both horizontal and vertical deformations of the roadway embankment. Higher PGA intensifies lateral seismic forces, while a raised water table reduces effective soil strength, exacerbating the potential for liquefaction and embankment instability. Under these conditions, the embankment is susceptible to deep surface cracking, localized distortions, and even partial structural failure. To mitigate these risks, strategies such as enhanced drainage systems, soil improvement through grouting or chemical additives, and the design of more resilient embankment structures are recommended. These findings emphasize the critical need for detailed investigations into the combined effects of seismic intensity and hydrogeological conditions on embankment performance. Moreover, they provide a practical basis for developing engineering solutions aimed at improving safety and minimizing earthquake-induced damage to transportation infrastructure.

Table 3. Crest horizontal displacements of the roadway embankment under the Kobe earthquake at varying peak ground accelerations (PGA).

	Horizontal displacement (m)			
Groundwater level from ground surface (cm)	**(PGA = 0.15)**	**(PGA = 0.25)**	**(PGA = 0.35)**	**(PGA = 0.45)**
100	1.32	1.82	2.14	3.62
60	1.86	2.41	3.12	4.15
20	2.52	3.26	3.88	4.65

Table 4. Crest vertical settlements of the roadway embankment under the Kobe earthquake at varying peak ground accelerations (PGA).

	Settlement (m)			
Groundwater level from ground surface (cm)	**(PGA = 0.15)**	**(PGA = 0.25)**	**(PGA = 0.35)**	**(PGA = 0.45)**
100	1.45	1.75	2.35	3.11
60	1.84	2.15	2.85	3.57
20	2.12	2.46	3.42	4.86

4.4. Influence of thickness of liquefiable soil

It is shown (in Fig. 15) that the effect of thickness of liquefiable soil on horizontal and vertical displacement profile of the roadway embankment under the different earthquakes. It is clear that the amount of horizontal and vertical displacement significantly increase with increase of thickness of liquefiable soil. This rate in higher PGA is more obvious especially (PGA > 0.35 g).

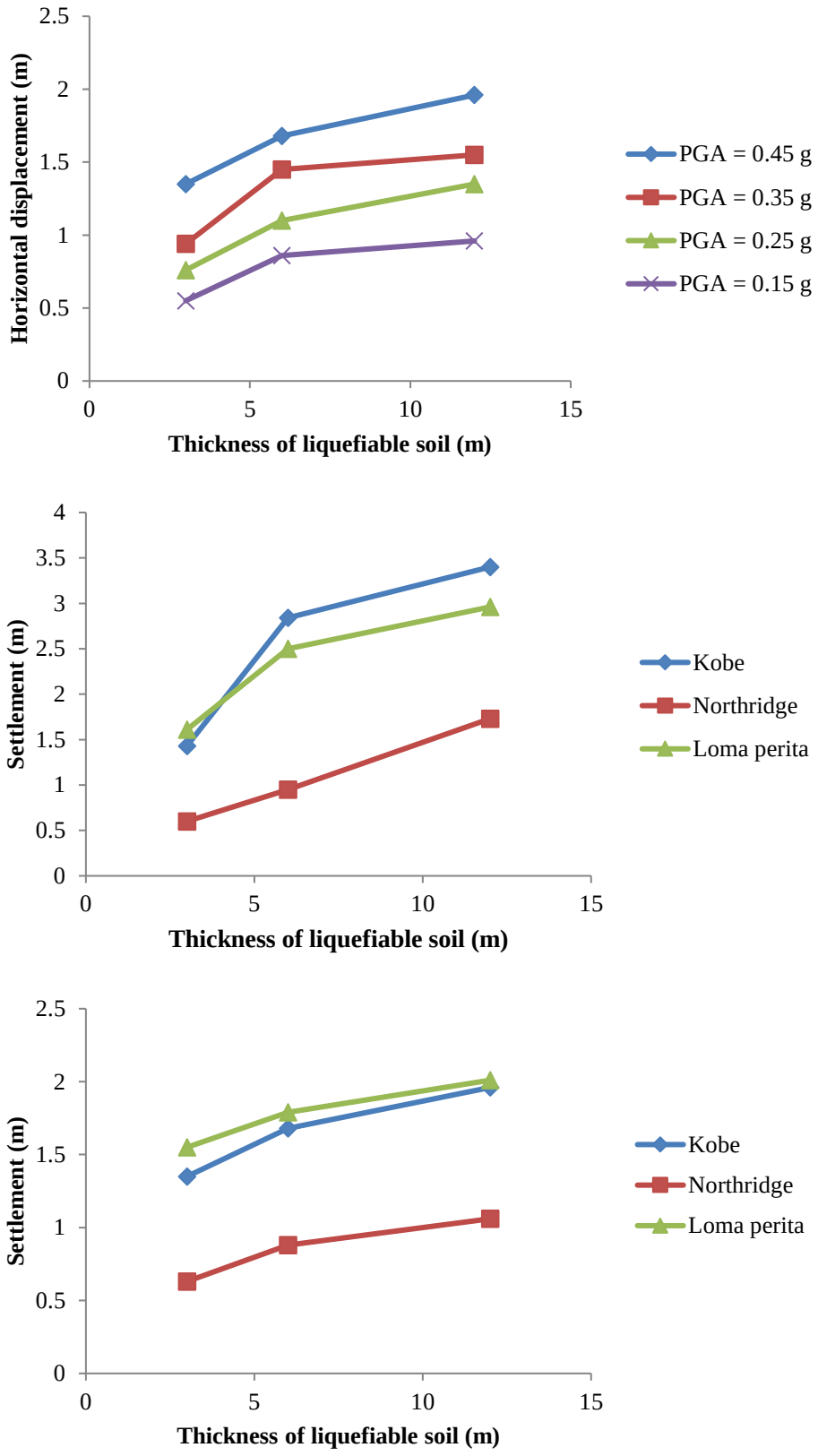

Fig. 15. Horizontal and vertical displacement profile of the roadway embankment under the different earthquakes.

5. Conclusion

This study employed numerical simulations to investigate the seismic response of road embankments constructed on liquefiable soils. The results demonstrate that the frequency content of earthquake input is a key parameter influencing both vertical and horizontal deformations. Even under similar peak ground accelerations, differences in seismic energy distribution can result in substantial variations in settlement and lateral displacement, highlighting the necessity of accounting for both PGA and input energy characteristics in seismic assessments. The analyses further indicate that increases in ground acceleration and elevated groundwater levels significantly exacerbate embankment deformations. Higher seismic forces, combined with reduced effective soil strength due to increased pore water pressure, amplify the risk of liquefaction and slope instability. Free-field analyses revealed that lateral

displacements, particularly near the surface, contribute notably to embankment instability. Peak settlements were observed predominantly during the strong-motion phase, often resulting in deep cracking, localized distortions, reductions in embankment height, and changes in surface slope. These deformations can compromise the structural integrity of the embankment and adversely affect the performance of adjacent transportation infrastructure. The findings emphasize the importance of comprehensive seismic evaluations for road embankments, particularly in regions with liquefiable soils. Mitigation strategies such as enhanced drainage to control pore pressure, soil improvement through grouting or dynamic compaction, and resilient structural design capable of accommodating a wide range of seismic frequencies and intensities are critical for reducing damage and improving overall stability. Implementing these measures not only protects the embankment but also contributes to the resilience and safety of transportation networks in seismically active areas.

Statements & Declarations

Author contributions

Vahid Sadeghi: Investigation, Formal analysis, Data curation, Software, Writing - Original Draft.

Mohsen Bagheri: Project administration, Resources, Software, Writing - Review & Editing.

Jaber Abasi Hamidi: Conceptualization, Methodology, Software, Writing - Review & Editing.

Funding

The authors received no financial support for the research, authorship, and/or publication of this article.

Data availability

The data presented in this study will be available on interested request from the corresponding author.

Declarations

The authors declare no conflict of interest.

References

[1] Argyroudis, S., Kaynia, A. M. Analytical seismic fragility functions for highway and railway embankments and cuts. Earthquake Engineering & Structural Dynamics, 2015; 44: 1863–1879. doi:10.1002/eqe.2563.

[2] Argyroudis, S., Kaynia, A. M., Pitilakis, K. Development of fragility functions for geotechnical constructions: Application to cantilever retaining walls. Soil dynamics and earthquake engineering, 2013; 50: 106–116. doi:10.1016/j.soildyn.2013.02.014.

[3] Ledezma, C., Hutchinson, T., Ashford, S. A., Moss, R., Arduino, P., Bray, J. D., Olson, S., Hashash, Y. M., Verdugo, R., Frost, D. Effects of ground failure on bridges, roads, and railroads. Earthquake Spectra, 2012; 28: 119–143. doi:10.1193/1.4000024.

[4] Cubrinovski, M., Robinson, K., Taylor, M., Hughes, M., Orense, R. Lateral spreading and its impacts in urban areas in the 2010–2011 Christchurch earthquakes. New Zealand Journal of Geology and Geophysics, 2012; 55: 255–269. doi:10.1080/00288306.2012.699895.

[5] Khalil, C., Rapti, I., Lopez-Caballero, F. Numerical Evaluation of Fragility Curves for Earthquake-Liquefaction-Induced Settlements of an Embankment. 1st ed. Reston (VR): American Society of Civil Engineers (ASCE); 2017. doi:10.1061/9780784480700.

[6] Oblak, A., Kosič, M., Viana Da Fonseca, A., Logar, J. Fragility Assessment of Traffic Embankments Exposed to Earthquake-Induced Liquefaction. Applied Sciences, 2020; 10: 6832. doi:10.3390/app10196832.

[7] Chakraborty, A., Sawant, V. A. Calibration of UBC3D-PLM Constitutive Model to Simulate the Dynamic Response of Earthen Embankment Resting on Liquefiable Soil. In: Proceedings of 17th Symposium on Earthquake Engineering (Vol. 3); 2023; Singapore. p. 771–783.

[8] El-Maissi, A. M., Argyroudis, S. A., Nazri, F. M. Seismic Vulnerability Assessment Methodologies for Roadway Assets and Networks: A State-of-the-Art Review. Sustainability, 2021; 13: 61. doi:10.3390/su13010061.

[9] El-Maissi, A. M., Argyroudis, S. A., Kassem, M. M., Mohamed Nazri, F. Integrated seismic vulnerability assessment of road network in complex built environment toward more resilient cities. Sustainable Cities and Society, 2023; 89: 104363. doi:10.1016/j.scs.2022.104363.

[10] Yildirim, A. K., Kavus, B. Y., Karaca, T. K., Bozbey, İ., Taskin, A. A novel seismic vulnerability assessment for the urban roadway by using interval valued fermatean fuzzy analytical hierarchy process. Natural Hazards, 2024; 120: 13811–13834. doi:10.1007/s11069-024-06748-1.

[11] Broniewicz, E., Ogrodnik, K. Application Potential of MCDM/MCDA Methods in Transport—Literature Review and Case Study. Sustainability, 2025; 17: 7671. doi:10.3390/su17177671.

[12] Maruyama, Y., Lai, S., Lchii, K., Tobita, T. Fragility functions for highway embankments based on damage data from recent earthquakes in Japan. Soil dynamics and earthquake engineering, 2010; 30: 1158–1167. doi:10.1016/j.soildyn.2010.04.013.

[13] Yang, M., Taiebat, M., Dafalias, Y. F. SANISAND-MSf: a sand plasticity model with memory surface and semifluidised state. Geotechnique, 2022; 72: 227–246. doi:10.1680/jgeot.19.P.363.

[14] López-Querol, S., Blázquez, R. Identification of failure mechanisms of road embankments due to liquefaction: optimal corrective measures at seismic sites. Canadian Geotechnical Journal, 2006; 43: 889–902. doi:10.1139/t06-051.

[15] Soleimanian, N., Akhtarpour, A., Baradaran, M. S. Experimental and Numerical Investigation of Landfill Leachate Emission in Unsaturated Sandy Soils. Civil Engineering and Applied Solutions, 2026; 2: 58–73. doi:10.22080/ceas.2025.29684.1028.

[16] Itasca, F. FLAC (Fast Lagrangian Analysis of Continua)-Fast Lagrangian Analysis of Continua. User Manual, Itasca Consulting Group, 2011;

[17] Kuhlemeyer Roger, L., Lysmer, J. Finite Element Method Accuracy for Wave Propagation Problems. Journal of the Soil Mechanics and Foundations Division, 1973; 99: 421–427. doi:10.1061/JSFEAQ.0001885.

[18] Martin Geoffrey, R., Seed, H. B., Finn, W. D. L. Fundamentals of Liquefaction under Cyclic Loading. Journal of the Geotechnical Engineering Division, 1975; 101: 423–438. doi:10.1061/AJGEB6.0000164.

[19] Byrne, P. M. A Cyclic Shear-Volume Coupling and Pore Pressure Model for Sand. In: InternationalConferences on Recent Advances in Geotechnical Earthquake Engineering and Soil Dynamics; 1991 Mar 12–13; St. Louis, Missouri. p. 47–55.

Civil Engineering and Applied Solutions

Research Article

journal homepage: ceas.journals.umz.ac.ir

CEAS Civil Engineering and Applied Solutions

Waste Management Future Planning in Iraq's Middle Euphrates Region through GIS-Based Multi-Criteria Decision Making for Optimal Landfill Siting

Ammar Rasheed Al-Hamami [a], Ozeair Abessi [a*], Ali Chabuk [b]

[a] *Department of Environmental Engineering, School of Civil Engineering, Babol Noshirvani University of Technology, Babol, Iran*
[b] *Department of Environmental Engineering, School of Engineering, University of Babylon, Babylon, Iraq*

ARTICLE INFO

Keywords:
Landfilling
Middle euphrates region
Multi-criteria
Decision-making

Article history:
Received 20 December 2025
Accepted 18 April 2026
Available online 01 October 2026

ABSTRACT

The Middle Euphrates region comprises four provinces: Najaf, Babylon, Karbala, and Qadisiya. These Iraq's central region provinces severely suffer from poor solid waste collection and disposal systems. There is no landfill site that meets the environmental standards, and this has led to several open dumping practices all around the region which negatively impacted public and environmental health. The lack of national strategies and properly designed landfill sites necessitated urgent action to implement a sustainable waste disposal method. This study tackles this problem by finding some safe locations for sanitary landfill employing a combination of MCDM and GIS techniques. Selecting a landfill site involves many criteria and restrictions, making it a challenging process. So, a range of factors, including sixteen criteria, were determined and weighted using AHP and SRS methods. A suitability index map for potential landfill sites was created by integrating these criteria. The final suitability maps (AHP and SRS) indicated that the majority of the region falls within moderate-to-high suitability classes, and eight candidate landfill sites (two per province) were selected within the 'high' and 'most suitable' zones for possible land filling. The study contributes to future waste management planning in Iraq's Middle Euphrates Region by integrating GIS-based suitability analysis with projected waste generation and landfill capacity requirements up to 2040.

1. Introduction

Rapid population growth, urbanization, and economic development have led to constant increases in municipal solid waste generation, posing significant challenges for sustainable waste management in developing countries. Inadequate infrastructure, limited financial resources, and reliance on uncontrolled dumping or poorly managed landfills have raised environmental and public health risks, including soil and groundwater contamination, air pollution, and ecosystem degradation. Besides population growth, the increasing level of welfare and living standards are becoming the main cause of rising solid waste production in the world. The expansion of economic and manufacturing activities in urban areas has also increased waste generation, making the management of growing volumes of solid waste a critical challenge in modern urban environments. Waste management involves a range of techniques and processes for the collection, transportation, treatment, and final disposal of waste materials, with the objective of minimizing adverse environmental, economic, and public health impacts [1]. In low and middle-income countries, landfilling is the most practical waste management option due to its relatively low costs, ability to handle unsorted waste, and lower technical requirements compared to other methods [2]. Therefore, landfilling, whether through multiple local sites or a single centralized facility, remains the most common disposal method in developing countries. When properly engineered, landfills represent a significant environmental improvement over open dumping. Therefore, sanitary ground-based landfilling is generally preferred over

* Corresponding author.
E-mail addresses: oabessi@nit.ac.ir (O. Abessi).

https://doi.org/10.22080/ceas.2026.30860.1067
ISSN: 3092-7749/
How to cite this article: Al-Hamami, A., Abessi, O., Chabuk, A. aste Management Future Planning in Iraq's Middle Euphrates Region through GIS-Based Multi-Criteria Decision Making for Optimal Landfill Siting. Civil Engineering and Applied Solutions. 2026; 2(4): 42–59. doi:10.22080/ceas.2026.30860.1067.

open space waste domping everywhere [3].

Solid waste management also involves waste gathering generated by industrial, commercial, residential, and public sectors. It represents a technical and systematic approach aimed at conserving natural resources by minimizing resource consumption and promoting waste reduction, reuse, and recycling. This framework ensures that all waste materials, whether solid, liquid, gaseous, or radioactive, are properly handled, treated, and disposed using appropriate methods to minimize their adverse impacts on the natural environment [4]. The importance of these systems has grown in parallel with industrial and societal development of our communities. At the beginning of the industrial revolution, better understanding of disease caused vaccination, sanitation systems, and public health contributing to lower mortality rates, particularly among children, and increasing average life expectancy. While at the same time, the rise of consumerist culture has contributed to an increase in the production of various types of wastes and their related diseases [5]. Hence, municipal systems must adapt effective approaches to preserve public health, hygiene, aesthetics, economic stability, and the environmental quality while the cities are developing [6]. Consequently, proper waste disposal through accurate and careful siting of the disposal facility has become crucial.

When selecting a site, numerous factors must be considered, such as population growth, governmental laws, social and environmental regulations, public health and safety issues, together with funding limitations from state and municipal sources [2]. Moreover, increasing the environmental awareness, limited land availability for waste disposal, and rising social and political opposition to regional landfill sitings are emerging challenges in this field [7, 8]. In landfills, the biological breakdown of buried organic material generates methane gas and leachate [1]. Waste disposal also leads to the release of toxic and other greenhouse gases, and it will contribute to global warming and environmental degradation to large scales [9]. All these limitations make landfills a transitional pathway toward more advanced integrated waste management systems in the intermediate term. Over the longer term, however, municipal waste disposal methods are expected to evolve towards more advanced and sustainable options, including waste incineration, large-scale composting, anaerobic digestion, and integrated recycling systems. The share of each may differ across regions, and decisions are made based on the amount of waste generated, waste composition, technological needs, and the urban planning capacity. Landfilling is easier to implement than other methods, and in general, it is inevitable in many cases. Therefore, even in countries with diverse waste management approaches, landfills continue to be essential for disposing of unusable or residual waste [10]. They also play a significant role in energy recovery from organic waste like an active bioreactor, which remains an ongoing concern [11]. So alongside the novel methods, i.e., waste reduction, recycling, reuse, composting, and energy recovery, landfilling is still and most probably in the future will be considered as an alternative for municipal waste disposal [12]. This approach involves the controlled burial of waste in the ground with multiple engineering measures to limit leachate and gas emissions [13]. Although landfill design and operational requirements are well documented in standards, guidelines, and technical handbooks [2], landfill siting remains a location-specific decision that must account for regional characteristics, country-specific regulations, and local constraints, necessitating modern methods and advanced tools [6, 7]. Recent studies have increasingly applied integrated remote sensing (RS), geographic information systems (GIS), and multi-criteria decision making (MCDM) techniques for municipal landfill site selection. Methodological transparency, robustness checking, and the production of planning-oriented outputs to support decision-making in data-scarce contexts are what are specifically emphasized in these studies [7, 14-17]. Amirsoleymani et al. [7] evaluated spatial restrictions for urban sanitary landfill siting in Mazandaran Province, Iran, using an integrated GIS and Analytic Hierarchy Process (AHP) approach. Environmental, geological, hydrological, and socio-economic criteria were weighted using expert judgment and spatially analyzed to identify suitable areas in accordance with Iran's national regulations. Elkhrachy et al. [14] employed RS data combined with GIS-based MCDM to identify suitable landfill sites in Najran City, Saudi Arabia, demonstrating the effectiveness of spatial analysis in addressing environmental and socio-economic constraints. Similarly, Saha and Roy [15] applied an RS–GIS-based MCDM framework to identify suitable waste disposal sites in Cooch Behar Municipality, India, aimed to help sustainable site selection under rapid urban growth. Sharma et al. [16] proposed an integrated GIS–MCDM framework incorporating zoning, ranking, and sensitivity analysis, highlighting the importance of robustness and decision reliability in landfill siting processes. In more complex regions, Chaturvedi et al. [17] combined RS–GIS tools with AHP and VIKOR methods to address landfill site selection challenges in hilly regions, demonstrating improved decision accuracy under topographic constraints. Collectively, these studies confirm that integrated GIS–MCDM approaches provide systematic and reliable tools for environmentally sound and socially acceptable landfill site selection.

It is worth noting that although sanitary landfills are accepted worldwide as a proper waste disposal method, they are not a common practice in Iraq, where open dumping is still widely used. Limited financial resources and lack of regulatory enforcement and strategic national waste management plans, besides geological and hydrological difficulties, such as shallow groundwater levels in many areas, seem to be the reason of prevalent open dumping traditions there. However, there are ongoing efforts in some Iraqi governorates to identify and develop suitable sanitary landfill sites based on the future scenarios and tourist activities variable [1, 8, 18]. This study aims to determine the optimal landfill sites in the Middle Euphrates region by applying key criteria aligned with ecological and technological regulations. Despite the extensive application of GIS–MCDM techniques in landfill siting studies, regional-scale analyses comparing multiple weighting approaches within a region remain limited, particularly in data-scarce contexts like Iraq. This study contributes to fill this gap in Iraq by jointly applying AHP and SRS methods within a GIS environment to support regional landfill planning across four provinces, while linking suitability outcomes with long-term waste generation and capacity projections up to 2040.

2. Study area

The study area of this paper is located within Iraq, a country in Western Asia bordered by several nations in the Middle East

region. Iraq covers an area of approximately 438,000 km² and exhibits diverse climatic, topographic, and hydrological conditions. The country experiences predominantly hot summers and mild to cool winters, with precipitation varying significantly across regions. In recent decades, the country has experienced rapid population growth and urban expansion, causing increasing pressure on infrastructure systems, particularly municipal solid waste management. The study region comprises four provinces: Najaf, Babylon, Karbala, and Qadisiya of the country of Iraq. Together, these provinces form the majority of the Middle Euphrates area, spanning about 47,426 km² and accounting for 10.82% of Iraq's total area (Fig. 1).

Al-Najaf Province is located in southern Iraq within the Mid-Euphrates Region. It is in a desert area, with an elevation of 70 meters above sea level [18]. The province borders Saudi Arabia externally. It spans roughly 28545 km^2 and has a population of 1,778,739 in 2024 [19]. It accounts for 6.6% of Iraq's total land area and is located at coordinates latitudes 31° 59' 16" N and longitudes 44° 19' 40" E. For administrative purposes, Al-Najaf is divided into three districts i.e.,Al-Najaf, Al-Kufa, and Al-Manathera [20]. Babylon Province is one of the most renowned ancient cities worldwide. Founded 4,100 years ago, Babylon served as the political centre of a vast and influential empire [21]. It spans an area of 5337 km² in central Iraq, approximately 100 km south of Baghdad, situated at coordinates longitudes 44° 25' 28" E and latitude 32° 28' 00" N. Based on census data from 2024, approximately 2,702,600 residents live within this province, distributed across its cities [22]. The primary district in the Babylon Province includes Al-Hillah, Al-Musayib, Al-Mahawil, Al-Qasim, and Al-Hashimiyah [23]. These primary cities are connected to sixteen smaller towns. Karbala Province covers 4,986 km² and has a population of approximately 1,418,950 people [22]. It is centrally located in Iraq between 44° 01′ 48″ E longitude and 32° 37′ 12″ N latitude. The area includes three districts: Karbala, Ain Al-Tamur, and Al-Hindiya. Muslims consider Karbala a sacred city because it contains some holy shrines for Shia Muslims. Each year, millions of pilgrims participate in various events in Karbala City. During the major gathering, Al-Arba'een, over 20 million pilgrims travel to Iraq for 15 to 20 days [23]. Al-Qadisyiah Province, also known as Al-Diwaniyah, is a major city located in south-central Iraq. It lies at latitudes 31°59' 00", and longitudes 44° 55' 00" E [24]. The province covers an area of 8558 km² and is divided into four primary districts, which include fifteen administrative regions, Al-Diwaniyah, Al-Shamiya, Afak, and Al-Hamza, and eleven sub-districts [25]. According to data from the Iraqi Ministry of Planning [22], the population is 1,430,714. These four provinces have implemented identical waste management strategies and are facing similar issues and challenges. A shared problem among all of them is the mismanagement in the collection, transportation, and disposal of municipal solid waste into standard sanitary landfills.

This study tries to estimate municipal waste generated in the Middle Euphrates Provinces by following a series of steps and calculations derived from recent local studies. The data collected enables the projection of waste generation up to 2040 (period of 22024-2040), considering a 2.5% annual population growth. The daily waste per person for the four provinces was estimated using data over the past five years, assuming a yearly increase of 1% in waste generation rates [19, 26]. The waste generated by visitors in Al-Najaf Ashraf and Holy Karbala was estimated too [23]. For calculating the area required for each landfill, the study assumed that 60% of the total waste comprises biodegradable materials, primarily organic components. This figure is grounded in prior research examining urban waste composition across the four provinces in the study region [27]. Accurately estimating the total volume of solid waste that requires disposal is a critical step in selecting appropriate landfill sites. To find optimal landfill site in each region spatial analyses were carried out within the GIS environment, utilizing consistent spatial referencing and raster processing settings to maintain methodological coherence.

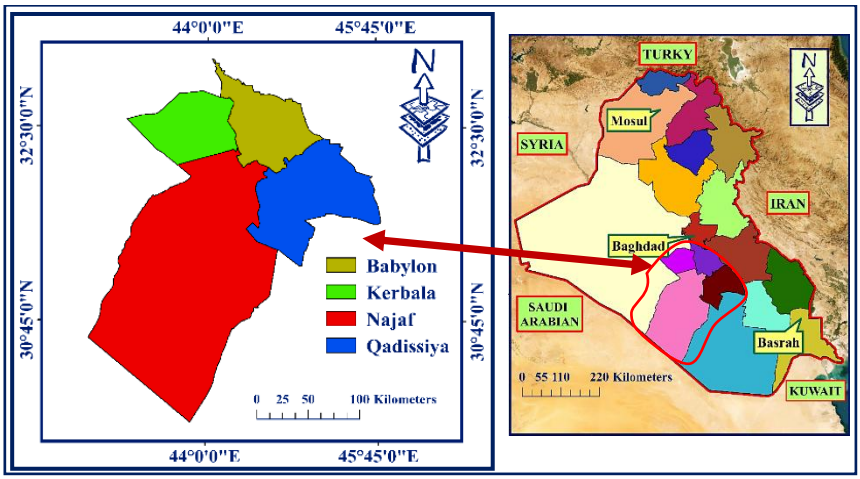

Fig. 1. The study area (Middle Euphrates region) consists of four provinces.

3. Material and methods

3.1. Conceptual model and hierarchies

Fig. 2 presents a summary of the proposed model designed for identifying landfill sites across the four Middle Euphrates Provinces in Iraq. It shows a structured framework that integrates environmental, technical, social, and economic factors to identify and compare suitable locations for a landfill. Environmental Criteria like the location of rivers, slope, land use, soil types, ground water level, etc are the core components of this conceptual model while technical and social-economical criteria like distance from residential areas (cities and villages), cultural sites, airport, refineries, power lines and accessibility to the site are other

complementary criteria. For the criteria, there are some absolute exclusion or buffer zone requirements to protect lands. Some countries have strict and clear national and regional environmental laws for the exclusions while Iraq lacks such detailed national regulations specifically for landfill siting and relying instead on broader environmental laws and plans that emphasize general protections. This step by step model first eliminates areas that violate legal and environmental constraints obtained through the literature and previous studies and do the suitability analysis for the remaining areas using weighted criteria and finally rank and classify the areas. The candidate sites compare for the accessibility and ownership ability and preferred site with minimum area needed for the waste produced along the period of operation will be selected. The processing steps of GIS, including buffering, distance mapping, reclassification, and weighted overlay, are described below in detail to ensure reproducibility.

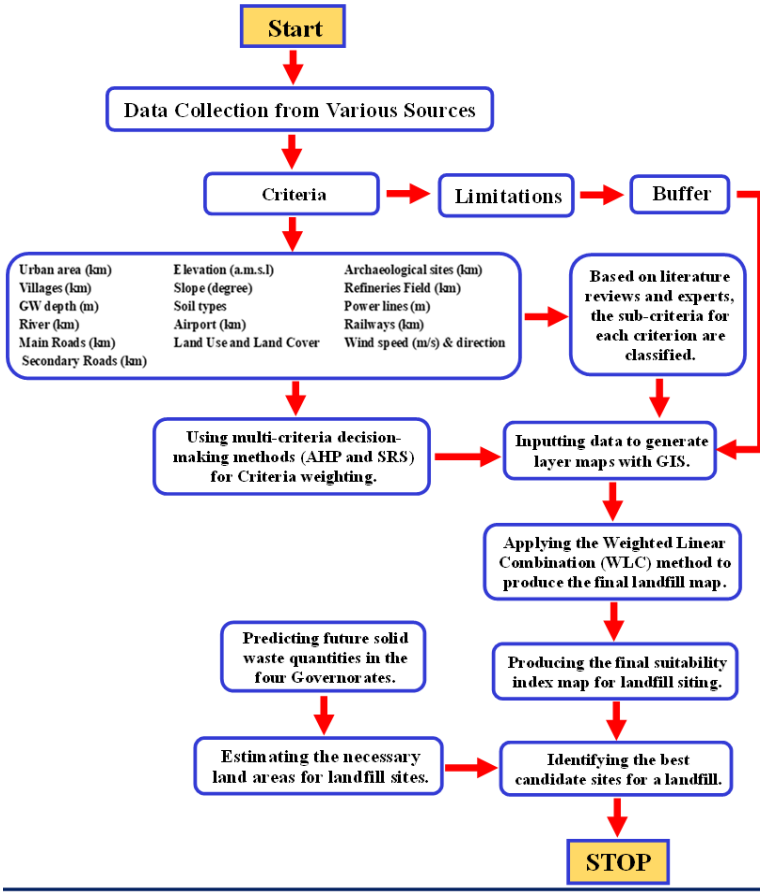

Fig. 2. Landfill site selection model and hierarchy of decision-making.

Environmental and artificial factors for landfill siting in the study area illustrated in Fig. 3. Although there are many potential criteria, using all of them is neither practical nor scientifically possible. Some out of many will be selected based on the scale and purpose of the study, legal and regulatory requirements, direct influences on environmental and public health risk, conditions of study region and expert local knowledge and judgment. Therefore, between numerous criteria proposed for landfill siting in the literature, only a limited number were selected in this study. The selected criteria represent the most influential, non-redundant factors, technical feasibility, and regulatory compliance at the regional planning scale.

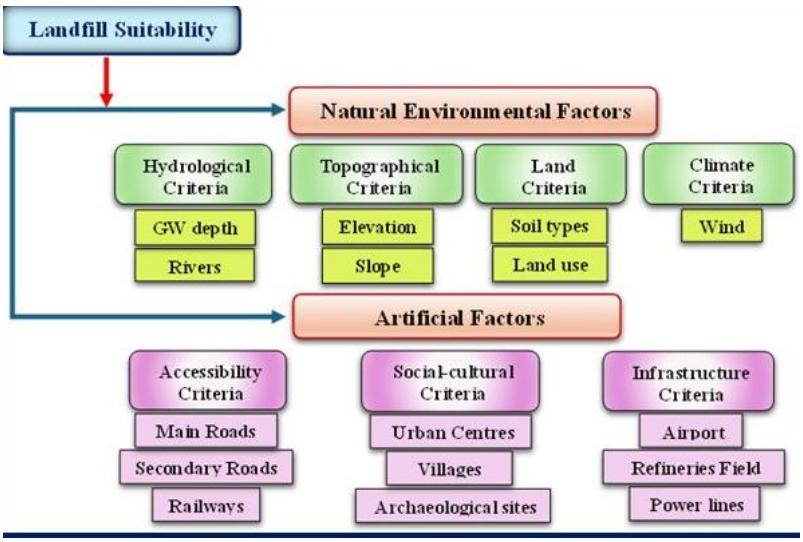

Fig. 3. Environmental and artificial factors for landfill siting in the study area.

3.2. GIS map layers

Various methods were employed in this study to generate the necessary map layers within GIS software. The first approach focused on creating individual shape files for various features, including urban areas, rivers, primary and secondary roads, villages, elevation, slope, power lines, refinery fields, and railways. The second technique utilized published information maps comprising geometric polygons representing locations, along with data stored in shape files, such as the soil types, sourced from Iraq's exploratory soil map, created at a scale of 1:1000000 [28] and the archaeological map of Iraq at the scale of 1:1500000, based on the World Digital Library, which is used to pinpoint archaeological and religious sites across the study provinces. The third approach uses kriging, an advanced spatial interpolation method, within ArcGIS's spatial analysis tools. It helps fill gaps between known data points, offering a more detailed view of spatial relationships. This method was used to generate a groundwater depth map from data collected from 222 wells across four provinces, based on information from the Iraqi Ministry of Water Resources [22]. The generated maps are used to convert vector maps into raster format, enabling easier provision and visualization of the raster data. All spatial datasets were processed within the ArcGIS environment (ArcGIS version 10.8) using the Spatial Analyst extension. A unified coordinate reference system (CRS) was applied to all layers (WGS 84 / UTM Zone 38N), and all raster datasets were resampled to a consistent spatial resolution of 30 × 30 m to ensure spatial compatibility prior to buffering, reclassification, and weighted overlay analysis. GIS operations including Euclidean Distance, Buffer, Reclassify, Raster Calculator (Map Algebra), and Weighted Overlay were applied systematically to generate standardized suitability layers.

3.3. Criteria selection

In the study, sixteen distinct criteria were created as layers encompassing the study region. Various GIS processes, including buffering, clipping, extracting, overlaying, proximity analysis, converting, reclassifying, and map algebra, were performed to generate the final layers, with each criterion being categorized within GIS. Based on earlier research and expert opinions, each class has been assigned an appropriateness rating, as presented in Table 1. For each criterion, the geographical feature or key location was encircled by a buffer zone. To develop the criteria map layers within the GIS framework, the entire study area was divided into several zones. Subsequently, the buffer maps were converted into raster maps using the following process.

A digital GIS database was created, and the exclusion zones were set up to enforce mapping restrictions. It helps to establish appropriate buffer zones or specific restrictions around the key areas to meet all criteria on the maps. MCDM models are used to identify the most suitable option by assigning weights to each criterion according to its relative importance in achieving the research objectives. Sub-criteria weightings are established based on literature, expert judgment, and environmental laws and regulations. To develop an effective index map and indicate the priorities for landfill site selection, all weighted criteria derived from AHP and SRS methodologies within GIS were overlaid.

Table 1. Suitability score for each selected criterion and its sub-criteria.

No.	Criteria	Buffer zone	Rating values	Notes
1	Urban area (km)	0 – 5 km	0	Buffer zone of 5 km [29-31]
		5 – 10 km	10	
		10 – 15 km	7	
		> 15 km	4	
2	Villages (km)	0 - 1 km	0	Buffer zone of 1 km [31, 32]
		> 1 km	10	
3	Groundwater Depth (m)	0 – 3 m	4	>30 m [33]; > 15 m [34]; 10 m [35]
		3 – 10 m	6	
		10 – 30 m	7	
		30 – 50 m	8	
		50 – 75 m	9	
		75 – 104 m	10	
4	Rivers (km)	0 - 1 km	0	Buffer zone of 1 km [32, 36, 37]
		> 1 km	10	
5	Main Roads (km)	0 - 0.5 km	0	Buffer zone of 1 km [38, 39]
		0.5 – 1 km	7	
		1 – 2 km	10	
		2 – 3 km	5	
		> 3 km	3	
6	Secondary Roads (m)	0 - 100 m	0	Buffer zone of 100 m [40, 41]
		100 – 500 m	5	
		500 – 1000 m	7	
		> 1000 m	10	

7	Elevation (a.m.s.l)	7 – 91 m	9	An essential aspect in waste disposal is the sea level of the area. Locations that are much higher above sea level and incur high transportation costs are usually deemed unsuitable. Conversely, areas close to sea level are more vulnerable to water contamination and flooding risks [33, 40]
		91 – 182 m	10	
		182 – 273 m	7	
		273 – 364 m	5	
		364 – 455 m	4	
8	Slope (degree)	0º - 5º	10	The best slope of landfilling is 0–5° [30, 41, 42]
		>5º	6	
9	Soil Types	SH (34)	3	Brown soil, medium and shallow phase over gypsum
		SW (35)	4	Brown soil, deep phase
		S1	1	Gypsiferous Gravel Soils
		S4	5	River Levee Soils
		S5	7	River Basin Soils, Silted Phase
		S6	9	Basin Depression Soils
		S7	10	Periodically Flooded Soils
		S8	9	Haur Soils
		S9	6	Silted Haur and Marsh Soils
		S11	4	Active Dune Land
		S17	2	Mixed Gypsiferous and Desert Land
		S18	3	Sand Dune Land
		S20	6	Stony desert land
		S21	3	Saline lake bottom land
		S5'	8	River Basin Soils in the Poorly Drained Phase
10	Airport (km)	0 - 5	0	Buffer zone of 5 km [32];3 km [40, 43]
		5 - 10	5	
		> 10	10	
11	Land-Use (LU)	Water bodies	0	Land-use (LU) items were adopted according to [39, 44, 45]
		Build up areas	0	
		Agriculture & Fertile	0	
		Unused lands	10	
12	Archaeological sites (km)	0 - 1 km	0	Buffer zone of 1 km [32, 36, 42]
		1 – 3 km	5	
		> 3 km	10	
13	Refinery fields (km)	0 – 5 km	0	Buffer zone of 5 km [32, 41, 44]
		> 5 km	10	
14	Powerlines (m)	0 – 30 m	0	Buffer zone of 30 m [37, 41]
		> 30 m	10	
15	Railways (km)	0 - 0.5 km	0	Buffer zone of 500 m [9, 41, 46]
		> 0.5 km	10	
16	Wind speed (m/s) & direction	2.19 - 2.42	5	In Al-Najaf City In Babylon City In Al-Qadisiya City In Karbala City Sites should be located away from residential areas, taking into account the prevailing wind direction [36]
		1.93 - 2.19	6	
		1.64 - 1.93	7	
		≤ 1.64 m/s	8	

The maps of sixteen GIS layers are as follows. "Urban Area" in which buffer zone was divided into four categories, as illustrated in Fig. 4a, ranging from 0 - 5 km, 5 - 10 km, 10 - 15 km, and over 15 km. These categories were scored as 0, 10, 7, and 4, respectively. The buffer zones in the "Villages" layer, extending from each village to the landfill site, have been categorized into two classes: 0-1 km and over 1 km. These categories were assigned scores of zero and ten (Fig. 4b). For "Groundwater Depth", potential sites were assigned rating grades of 4, 6, 7, 8, 9, and 10 based on depths of 0 - 3 m, 3 - 10 m, 10 - 30 m, 30 - 50 m, 50 - 75 m, and more than 75 m, respectively (Fig. 4c). The "River" grading criteria assigns a zero score to the buffer zone within 0-1000 m from the river boundary, and a score of 10 for zones beyond 1000 m, indicating surface water protection from contamination (Fig. 4d). The buffer zones of the "Main Road" layer, which extend from roads to landfill sites, are categorized into five distinct ranges, as shown in Fig. 4e. The ranges are 0 - 500 m, 500 - 1000 m, 1000 - 2000 m, 2000 - 3000 m, and over 3000 m, with respective scores of 0, 7, 10, 5, and 3. The buffer zones of the "Secondary Road" layer, which extend from roads to landfill sites, are divided into four categories, as shown in Fig. 4f. The zones are categorized as 0 - 100 m, 100 - 500 m, 500 - 1000 m, and over 1000 m, with scores of 0, 5, 7,

and 10 assigned accordingly. The Elevation map (Fig. 4g) contains mean sea level (a.m.s.l.) related calculations. The elevation values were 9, 10, 7, 5, and 4, classified into five categories (a.m.s.l.) of 7-91, 91-182, 182-237, 237-364, and 364-455, respectively. Elevations from 91 to 182 (a.m.s.l.) were considered the most suitable elevation for landfill siting, whereas those between 7 and 91 (a.m.s.l.) were considered only appropriate. To prepare the "Slope" layer map, areas with slopes of 0–5 degrees were assigned a score of 10, while those with slopes of 5–15 degrees received a score of 6 (Fig. 4h). The soil in the Middle Euphrates is composed of alluvial deposits, which are detrital materials. These deposits extend over the entire region to a depth of more than 50 meters, with no bedrock exposed [47]. Furthermore, the soil shows no evidence of cracks or faults. Therefore, the Middle Euphrates area is not classified as a seismic hazard zone [48]. According to Buringh [28], the 'Soil Types' layer in the study area includes fifteen different types (Fig. 4i). These include Brown soil with medium and shallow phases over gypsum; Brown soil with deep phases; Gypsiferous Gravel Soils; River Levee Soils; River Basin Soils with Silted Phases; Basin Depression Soils; Periodically Flooded Soils; Haur Soils; Silted Haur and Marsh Soils; Active Dune Land; Mixed Gypsiferous and Desert Land; Sand Dune Land; Stony Desert Land; Saline Lake Bottom Land; and River Basin Soils with Poorly Drained Phase. Each has been assigned scores of 3, 4, 1, 5, 7, 9, 10, 9, 6, 4, 2, 3, 6, 3, and 8 based on their features. The buffer zone for the ‘‘Airport’’ layer was divided into three categories (Fig. 4j). The first category, covering buffer zones of fewer than 5 km around the airport, is prohibited and assigned a value of zero. The second category includes buffer zones of 5-10 km, which received a value of 5. The peak rate of 10 was given to buffer > 10 km.

The "Land Use Classification" (LUC) map of the study area was divided into four categories, shown in Fig. 4k: agriculture and fertile land, water bodies, unused lands, and built-up areas. Each category was assigned a score of 0, except for Unused Land, which received a score of 10. The buffer zone for the ‘‘Archaeological Sites’’ layer was categorized into three classes, as depicted in Fig. 4l. Areas within 1 km of archaeological sites were excluded and given a zero value. Buffer zones between 1 and 3 km received a value of 5, and those exceeding 3 km were assigned the maximum value of 10. The buffer zone of the "Refinery fields" map layer was categorized into two classes, as shown in Fig. 4m. The first category covers buffer zones of 0 - 5 km around oil and gas sites with a zero score, indicating it is banned. The second category, which includes buffer zones > 5 km, received a score of 10. The buffer zones of the "Powerlines" layer, which include areas from powerlines to landfill sites, were categorized into two classes (0 - 30 m and over 30 m) as shown in Fig. 4n. These classes were assigned scores of 0 and 10. The buffer zones in the "Railways" layer, which include areas from railways to landfill sites, are divided into two classes (Fig. 4o). These classes are 0-0.5 km and over 0.5 km, assigned scores of 0 and 10. For the "Wind Speed" layer map, wind speeds were categorized into four classes: 2.19-2.42 m/s, 1.93-2.19 m/s, 1.64-1.93 m/s, and below 1.64 m/s. These classes were assigned grades of 5, 6, 7, and 8, respectively (Fig. 4p).

3.4. MCDM weighting

MCDM methods improve decision quality by clarifying, streamlining, and making the decision-making process more rational. Think of multi-criteria decision making (MCDM) as a core component of modern decision science and operational research. It deals with many decision criteria and options, providing a range of choices that consider different factors [16, 44]. Once the criteria maps are completed in the GIS, the process of selecting suitable waste burial sites in the study area begins. Two different methods were employed to assign weights to the criteria, using various styles within the MCDM techniques to assess each criterion's importance. These approaches are among the most frequently used in MCDM. The use of MCDM methods consists of the pairwise comparison method (AHP) and the Ranking method (SRS). The following methods were employed to identify the key weights of the criteria.

- Analytical Hierarchy Process (AHP)

This method is considered to facilitate faster decision-making, to analyse data, and assign appropriate weights to the selected criteria. A key step involves constructing a pairwise comparison matrix to evaluate the relative importance of the selected criteria with respect to the overall decision goal. This method was used across all provinces in the Middle Euphrates region to select appropriate landfills, showing its strong theoretical basis. It employs a nine-point scale, frequently utilized in analytic hierarchy processes, which indicates the relative importance of two factors at each point (see Table 2). This allows decision-makers to evaluate the contribution of each factor for achieving the goal through pairwise comparisons, thereby streamlining the decision procedure [49].

Table 2. The relative importance in pairwise comparisons [50].

Importance Intensity	Definition
1	Equal importance
2	Equal to moderately important
3	Moderate importance
4	Moderate to strong importance
5	Strong importance
6	Strong to very strong importance
7	Very strong importance
8	Very to extremely strong importance
9	Extreme importance

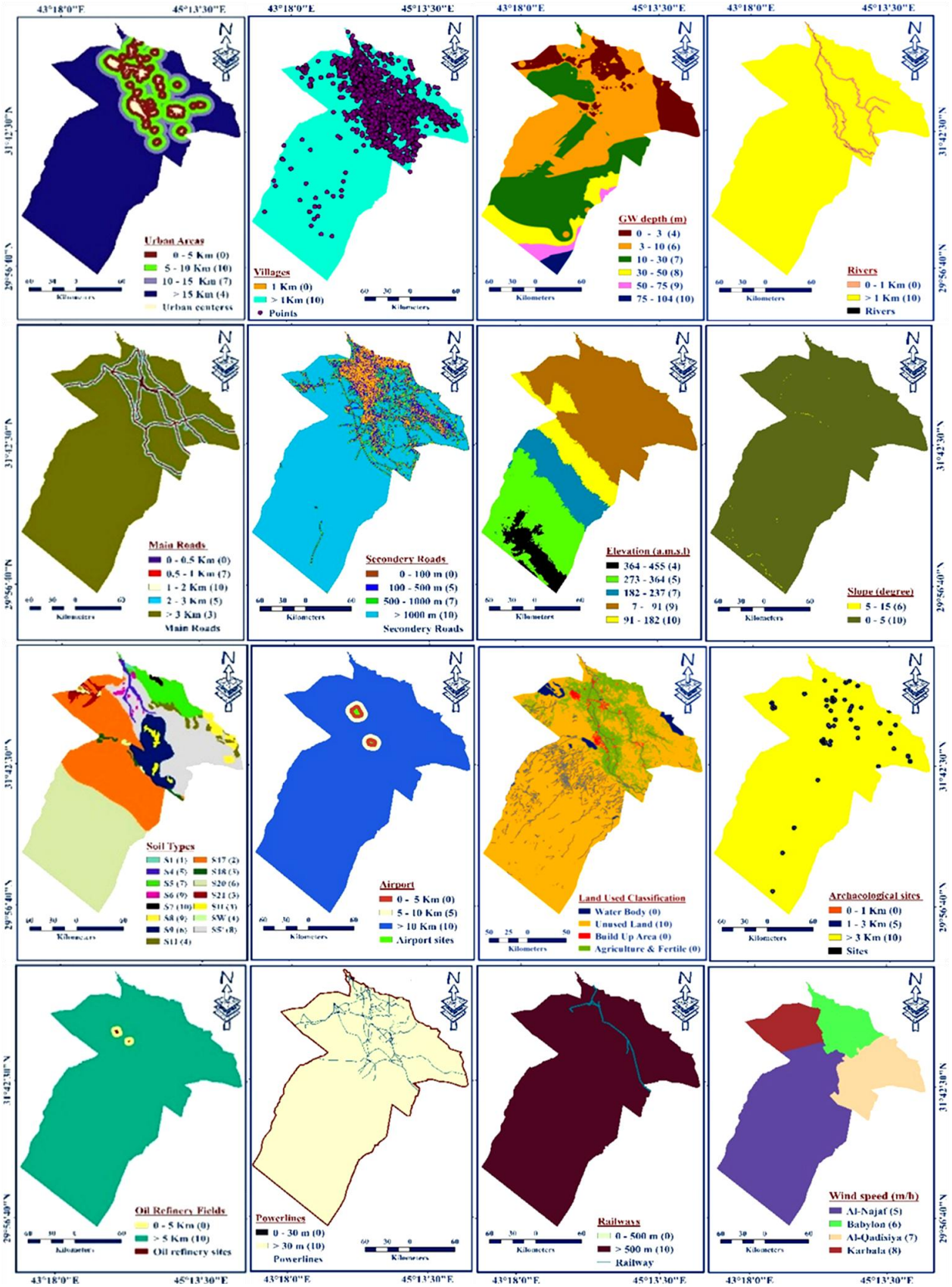

Fig. 4. Classified maps of the study area for (a) urban area, (b) villages, (c) GW depth, (d) rivers, (e) main road, (f) secondary road, (g) elevation, (h) slope, (i) soil types, (j) airport, (k) land use land cover (LULC), (l) archaeological sites, (m) Refinery fields, (n) powerlines, (o) railways, (p) wind speed.

In this study, the pairwise comparison matrix was constructed to compare the relative importance of the selected criteria, resulting in an $n \times n$ matrix, where n represents the total number of criteria (n = 16). Uyan [32] indicated that the elements of the pairwise comparison matrix are denoted by a_ij, where i = 1, 2, …, n and j = 1, 2, …, n. The comparison values are placed in the upper triangular part of the matrix, while the reciprocal values are used to fill the corresponding entries below the diagonal, as expressed in Eq. 1:

$$a_{ji} = \frac{1}{a_{ij}} \quad (1)$$

where a_{ij} is the element of the matrix representing the relative importance of the criterion i over criterion j.

The significance of the criteria from the standard comparison matrix can be illustrated in a matrix for decision-making on any problem using the method outlined below. This process involves multiplying each row of the original pairwise comparison matrix by the value of each criterion in the corresponding column for that row, applying the same multiplication across all rows. It is expressed using Eq. 2:

$$Eg_i = \sqrt[n]{a_{11} \times a_{12} \times a_{13} \times \ldots \times a_{1n}} \quad (2)$$

where n is the number of criteria and Eg_i represents the geometric mean of the pairwise comparison values for the criterion i. To obtain the priority vector (Pr_i), the geometric mean values are normalized by dividing each component by the sum of all geometric mean values, as shown in Eq. 3:

$$Pr_i = \frac{E_{gi}}{\sum_{k=1}^{n} E_{gk}} \quad (3)$$

The maximum eigenvalue (λ_{max}) was estimated based on the weighted sum of the pairwise comparison matrix and the derived priority vector, following the standard AHP procedure described in the literature.

$$\lambda_{max} = \sum_{j=1}^{n} WC_j * \sum_{i=1}^{m} a_{ij} \quad (4)$$

where, WC_j means the weighting value for each criterion, corresponding to the priority vector of the matrix. Here, i and j range from 1 to m and n, respectively. Additionally, a_{ij} indicates the sum of the criteria for each column of the matrix. The λ_{max} value in this study is 16.66. Lastly, Eq. 5 is employed to calculate the consistency index (*CI*):

$$CI = \frac{(\lambda_{max} - n)}{(n-1)} \quad (5)$$

This study shows that the *CI* is 0.0446, which indicates the variability of the estimated mistake around the actual value. As per Sólnes [51], *n* indicates the size of the matrix for the comparison components, while *CI* denotes the mean deviation. Alonso and Lamata [52] provided the average random index (*RI*) for matrices of various sizes in Table 3. Since this study involves 16 criteria, the *RI* value for n = 16 is 1.5978.

In this study, the consistency ratio (*CR*), which was 0.0279, is determined by dividing the consistency index (*CI*) by the random index (*RI*), as illustrated in Eq. 6.

$$CR = \frac{CI}{RI} \quad (6)$$

According to Coyle [53], a *CR* of zero indicates perfect consistency in any matrix, while Setiawan et al. [54] state that a *CR* above 0.1 suggests the need to reconsider or reverse the pairwise comparisons. In this study, sixteen criteria were used to create the pairwise comparison matrices. The calculated *CR* was 0.0279, which is well below 0.1, indicating a reasonable level of consistency in the current pairwise comparisons. Additionally, the *RI* value for n = 16 was estimated at 1.5978 for all matrices.

Table 3. RI for different values of *n* [52].

n	1	2	3	4	5	6	7	8	9	10	11	12	13	14	15	16
RI	0	0	0.58	0.9	1.12	1.24	1.32	1.41	1.45	1.49	1.51	1.48	1.56	1.57	1.59	1.59

Table 4 shows the priority vector and weight values for each criterion involved in the decision-making process. The study assessed the significance of each criterion compared to others, based on input from experienced field experts. Each criterion received a weight reflecting its importance. These weights were then used to build the AHP matrix, which allowed for calculating the precise weight of each criterion.

Table 4. The matrix of random pairwise comparisons used to estimate landfill site criterion weights.

Criteria	**UR**	**Villages**	**GW**	**River**	**M-Road**	**S-Road**	**Top.**	**Slope**	**Soil**	**Airport**	**Land Use**	**Arch.**	**Refinery**	**Power**	**Railways**	**Wind**
UR	1	2	2	3	4	4	5	5	5	6	6	7	7	8	8	9
Villages	0.50	1	1	2	3	3	4	4	4	5	5	6	6	7	7	8
GW	0.50	1.0	1	2	3	3	4	4	4	5	5	6	6	7	7	8
River	0.33	0.50	0.50	1	2	2	3	3	3	4	4	5	5	6	6	7
M-Road	0.25	0.33	0.33	0.5	1	1	2	2	2	3	3	4	4	5	5	6

S-Road	0.25	0.33	0.33	0.5	1	1	2	2	2	3	3	4	4	5	5	6
Top.	0.20	0.25	0.25	0.33	0.5	0.5	1	1	1	2	2	3	3	4	4	5
Slope	0.20	0.25	0.25	0.33	0.5	0.5	1	1	1	2	2	3	3	4	4	5
Soil	0.20	0.25	0.25	0.333	0.5	0.5	1	1	1	2	2	3	3	4	4	5
Airport	0.17	0.20	0.20	0.25	0.333	0.33	0.5	0.5	0.5	1	1	2	2	3	3	4
Land use	0.167	0.200	0.20	0.25	0.333	0.333	0.5	0.50	0.5	1	1	2	2	3	3	4
Arch.	0.143	0.167	0.167	0.20	0.25	0.25	0.33	0.33	0.33	0.5	0.5	1	1	2	2	3
Refineryfield	0.143	0.167	0.167	0.20	0.25	0.25	0.33	0.333	0.33	0.5	0.5	1	1	2	2	3
Power	0.125	0.143	0.143	0.17	0.20	0.20	0.25	0.25	0.25	0.33	0.33	0.5	0.5	1	1	2
Railways	0.125	0.143	0.143	0.17	0.20	0.200	0.25	0.25	0.25	0.333	0.33	0.5	0.5	1	1	2
Wind	0.111	0.125	0.125	0.14	0.167	0.167	0.20	0.2	0.2	0.25	0.25	0.33	0.33	0.5	0.5	1

To determine the weights of criteria using the AHP, a structured questionnaire was employed. The questionnaire was distributed to 31 experts with professional backgrounds in environmental engineering, urban planning, and municipal solid waste management, as shown in Table 5. The respondents were selected based on their academic qualifications and practical experience in waste management and environmental planning. Individual pairwise comparison matrices were collected and aggregated using the geometric mean method to derive the final comparison matrix. The reliability of the collected judgments was evaluated for each using the consistency index (*CI*) and consistency ratio (*CR*), which confirmed an acceptable level of consistency.

Table 5. Expert profile and questionnaire summary used for AHP weighting.

Item	Description
Number of questionnaires distributed	31
Expert background	Environmental engineering, urban planning, GIS, and solid waste management
Professional experience	More than 5 years
Affiliation	Universities, municipalities, environmental and planning agencies
Questionnaire type	Structured AHP pairwise comparison questionnaire
Judgment aggregation method	Geometric mean
Reliability assessment	Consistency Index (CI) and Consistency Ratio (CR < 0.1)

The criteria weighting process was designed to ensure transparency and reproducibility by combining expert judgment with established guidance from the literature and relevant environmental planning considerations. Literature and regulatory guidelines were also used to define exclusion constraints and inform the relative importance of criteria, while the final weighting values primarily reflect the collective expert assessment of regional environmental and planning priorities. The assignment of weights to the criteria was based on the primary goal of minimizing environmental and public health risks while ensuring practical feasibility at the regional planning level. Criteria that are directly related to environmental protection and human exposure, such as distance from urban centers, groundwater depth, and proximity to surface water bodies, were given higher weights because they play a crucial role in preventing contamination and health impacts. In contrast, criteria associated with technical accessibility and infrastructure, including roads, power lines, and railways, received lower weights since these factors can be addressed through engineering solutions during the design and operation of landfills. The final weights represent a balanced integration of expert judgment, established landfill siting guidelines found in the literature, and regional planning considerations specific to the Middle Euphrates area.

- Straight Rank Sum (SRS) Technique

This technique is among several ranking methods utilized in multi-criteria decision-making analyses. Based on literature and expert judgment, it offers a straightforward approach for assigning weights to criteria by ranking them from most to least important using the expression $n - r_i + 1$. To standardize these weights, each criterion weight is divided by the total sum of all ranking values, which is obtained by summing $(n - r_g + 1)$ as shown in Eq. 7 [30, 44]:

$$W_i = \frac{n - r_i + 1}{\sum (n - r_g + 1)} \quad (7)$$

In Eq. 7, W_i is the normalized weight of the ith criterion, n is the total number of criteria (n = 16), and r_i is its assigned rank ($r_i = 1$ for the most important and $r_i = n$ for the least important). The summation term normalizes the weights so that $\sum Wi$ = 1, and the resulting SRS weights are reported in Table 6.

Table 6. The weights assigned to criteria in the SRS method and their normalized values.

No.	Criterion	Criteria weights ($n - r_i + 1$)	Normalized weights (W_i)
1	Urban centres	16	0.1176
2	Villages	15	0.1103
3	Groundwater depth	14	0.1029

4	Rivers	13	0.0956
5	Main Roads	12	0.0882
6	Secondary Roads	11	0.0809
7	Elevation	10	0.0736
8	Slope	9	0.0662
9	Soil types	8	0.0588
10	Airport	7	0.0515
11	Land use	6	0.044
12	Archaeological sites	5	0.0368
13	Refinery fields	4	0.0294
14	Power lines	3	0.0221
15	Railways	2	0.0147
16	Wind	1	0.0074

The Weighted Linear Combination (WLC) method then calculated the appropriateness index for potential locations using the following formula:

$$Y_i = \sum_{j=1}^{n} W_j \times C_{ij} \quad (8)$$

where n represents the total number of criteria, Y_i is the suitability index, W_j indicates the criterion's relative importance weight, and C_{ij} is the grading value for criterion i [55].

Using the GIS "Map Algebra" tool, the WLC method was applied to generate the suitability index map. The standardized raster layers of each criterion were multiplied by their corresponding weights and subsequently summed to produce the final suitability index.

4. Results and discussion

The suitability index is developed using criterion weights derived from the Analytical Hierarchy Process (AHP) or the Straight Rank Sum (SRS) method, and by integrating both approaches within the GIS environment. These methods were used to quantify the relative importance of siting criteria, where AHP was based on expert judgment through pairwise comparisons, while SRS applied a direct rank-based weighting scheme. The weighted linear combination of the criteria was then used to produce a spatially continuous acceptability index, which was subsequently classified to identify suitable landfill sites. Table 7 presents the criterion weights obtained using both AHP and SRS methods. Some criteria were assigned higher weights under the AHP approach compared to the SRS method. The differences observed between the suitability results derived from the AHP and SRS methodologies reflect their distinct theoretical foundations and implications for regional planning. The AHP method relies on expert judgment and pairwise comparisons, which tend to emphasize environmentally sensitive criteria such as proximity to urban areas, groundwater depth, and surface water protection. Consequently, the AHP-based suitability map presents a more conservative spatial pattern, with a smaller proportion of areas classified as "most suitable". In contrast, the SRS method adopts a linear rank-based weighting scheme that distributes importance more evenly across the selected criteria, resulting in a broader spatial extent of areas classified as high and most suitable. The comparison between these two approaches highlights the complementary strengths of each method and supports the use of both AHP and SRS in parallel. This combined application enhances the robustness of the decision-making process and provides a more balanced framework for regional landfill planning.

A numerical comparison of the derived weights further explains the observed differences between the AHP- and SRS-based suitability maps. For instance, environmentally sensitive criteria such as distance from urban centers and groundwater depth received noticeably higher weights under the AHP method (0.1929 and 0.143, respectively) compared to the SRS method (0.1176 and 0.1029), reflecting the stronger influence of expert judgment in emphasizing environmental protection. Conversely, criteria related to accessibility and physical characteristics, such as elevation and slope, exhibited relatively higher weights under the SRS approach due to its rank-based structure, which distributes importance more evenly across criteria. These numerical differences directly contributed to the more conservative spatial extent of high and most suitable areas in the AHP results, and the broader distribution observed in the SRS-based suitability map, as reflected in Table 8.

Table 7. Weight of criteria according to multi-criteria decision-making techniques (SRS and AHP).

No.	Criteria	AHP	SRS	No.	Criteria	AHP	SRS
1	Urban centres	0.1929	0.1176	9	Soil types	0.0463	0.0588
2	Villages	0.143	0.1103	10	Airport	0.0303	0.0515
3	GW depth	0.143	0.1029	11	Land use	0.0303	0.044
4	Rivers	0.102	0.0956	12	Archaeological sites	0.0203	0.0368
5	Main Roads	0.0704	0.0882	13	Refinery fields	0.0203	0.0294

6	Secondary Roads	0.0704	0.0809	14	Power lines	0.014	0.0221
7	Elevation	0.0463	0.0736	15	Railways	0.014	0.0147
8	Slope	0.0463	0.0662	16	Wind	0.0102	0.0074

The final suitability GIS map is obtained through a weighted overlay process, where each spatial criterion is standardized, weighted, and mathematically combined. This approach enables the integration of heterogeneous spatial datasets while preserving the relative importance of each criterion as determined by the decision-making framework. To facilitate interpretation and decision-making, the continuous suitability index was divided into seven categories. The classification was performed using the natural breaks (Jenks) method to ensure a data-driven separation of suitability classes. Each suitability class encompassed specific spatial extents, quantified as a percentage of the total study region. The classes include unsuitable areas, very low suitability, low suitability, marginally suitable, moderately suitable, high suitability, and most suitable. Fig. 5a and 5b display the suitability maps produced by the AHP and SRS methods, accompanied by Table 8. The lower suitability classes are primarily associated with areas constrained by environmental sensitivity and unfavorable physical conditions, such as proximity to surface water bodies or urban or rural zones. In contrast, areas classified as high and most suitable are generally associated with locations exhibiting favorable combinations of environmental protection, technical feasibility, and accessibility, indicating their higher potential for landfill development under the applied criteria.

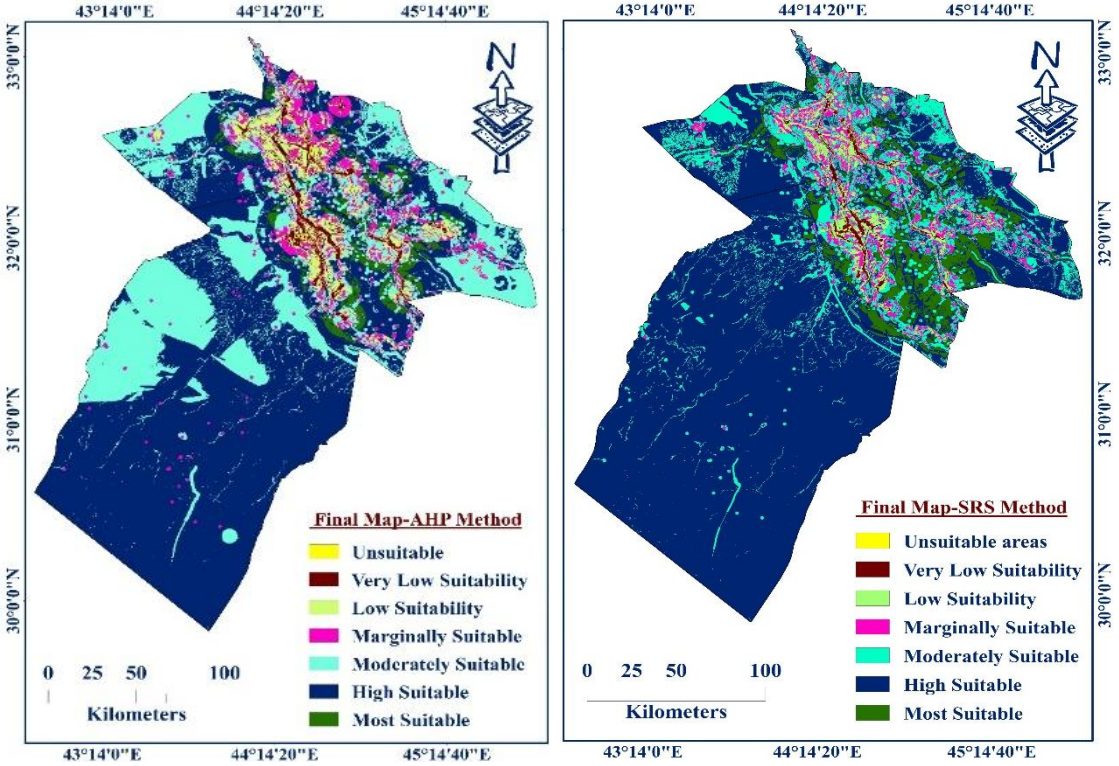

Fig. 5. Suitability final maps for landfill in the Middle Euphrates Region using (a) AHP, (b) SRS.

To enhance the reliability of the generated suitability maps, the distribution of unsuitable and low-suitability areas was qualitatively compared with established environmental and planning constraints, such as rivers, urban settlements, agricultural lands, and shallow groundwater zones. Additionally, the identified high- and most suitable areas were reviewed by domain experts to ensure their practical feasibility within the context of regional planning.

Table 8. The areas and their proportion of landfill maps classes in GIS, using AHP and SRS methods.

No.	Class	AHP method		SRS method	
		Area (km^2)	Proportion (%)	Area (km^2)	Proportion (%)
1	Unsuitable areas	80.91	0.18	10.33	0.02
2	Very Low Suitability	808.15	1.70	347.03	0.79
3	Low Suitability	2130.08	4.50	1527.14	3.22
4	Marginally Suitable	2771.93	5.84	2490.23	5.25
5	Moderately Suitable	13550.89	28.57	7122.65	15.02
6	High Suitable	26750.09	56.40	32902.98	69.38
7	Most Suitable	1334.58	2.81	2999.27	6.32

The area of each suitability class was calculated directly within the GIS environment based on raster cell counting. Following the weighted overlay process, the final suitability maps were reclassified into seven classes, and the number of raster cells belonging

to each class was extracted. The area corresponding to each class was then computed by multiplying the number of cells by the area of a single raster cell. For example, if a suitability class contains N raster cells and each cell represents an area of A km², the total area of that class is calculated as Area = $N \times A$. The same procedure was consistently applied to both AHP- and SRS-based suitability maps, and the resulting areas and proportions are summarized in Table 8. The suitability index was also classified into seven categories to provide sufficient differentiation between unsuitable, marginal, and highly suitable areas while maintaining interpretability for regional planning purposes. This classification scheme is consistent with commonly adopted practices in GIS–MCDM landfill siting studies, allowing decision-makers to clearly distinguish between restricted zones and priority areas for potential development. The class thresholds were derived from the natural breaks in the continuous suitability index values generated by the weighted overlay process, ensuring a data-driven rather than arbitrary classification. The same classification framework was applied to both AHP- and SRS-based suitability maps to enable consistent comparison, and the spatial extent and proportion of each class are reported in Table 8. Model validation was conducted by two main methods: (i) ensuring that the 'most suitable' outputs do not overlap with exclusion zones, such as urban buffers, surface water buffers, and protected or archaeological areas, and (ii) having experts review the proposed candidate sites to confirm their practical feasibility at the regional planning scale.

In the Middle Euphrates region, the projected population for 2040 includes 4,012,025 residents in Babylon, 2,640,548 in Al-Najaf, 2,106,439 in Karbala, and 2,123,903 in Al-Qadisiyah. The anticipated solid waste production in these provinces by that year is calculated about 464,788 tons in Babylon, 290,061 tons in Al-Najaf, 243,583 tons in Karbala, and 224,570 tons in Al-Qadisiyah. Additionally, the total solid waste from 2024 to 2040 is projected to be 6,075,446 tons in Babylon, 3,854,826 tons in Al-Najaf, 3,292,411 tons in Karbala, and 2,935,457 tons in Al-Qadisiyah, based on calculations by Chabuk [19]. The solid waste density at disposal sites in the Middle Euphrates region is assumed to be 700 kg/m³, consistent with recent studies [19, 56, 57]. The total waste volume was therefore estimated as 8,679,209 m³ for Babylon, 5,506,894 m³ for Al-Najaf, 4,703,444 m³ for Karbala, and 4,193,510 m³ for Al-Qadisiyah, respectively. The volumes are obtained by dividing the cumulative solid waste quantity by the waste density.

According to Chabuk [19], the groundwater depth from the surface in the Middle Euphrates region is shallow. As a result, an average groundwater depth of 2 meters has been adopted for the candidate sites identified in the study. Based on this condition, the necessary area to hold the total produced waste from 2024 to 2040 in the study provinces is calculated as 4.34 km² for Babylon, 2.75 km² for Al-Najaf, 2.35 km² for Karbala, and 2.1 km² for Al-Qadisiyah. It should be noted that the assumed waste density and groundwater depth values represent average regional conditions. Therefore, detailed site-specific geotechnical and hydrogeological investigations are required prior to final landfill design and implementation. Based on these considerations, eight candidate landfill sites were proposed for the region, with two sites selected within each province to ensure balanced regional coverage. The selection was based on a combination of high and most suitable classes derived from both AHP and SRS methods, minimum area requirements calculated from projected waste volumes, accessibility considerations, and overall planning feasibility. The proposed sites span areas of 6.1 and 7.4 km² in Babylon, 7.2 and 6.0 km² in Qadisiyah, 7.3 and 6.8 km² in Al-Najaf, and 5.6 and 5.0 km² in Karbala, as illustrated in Fig. 6.

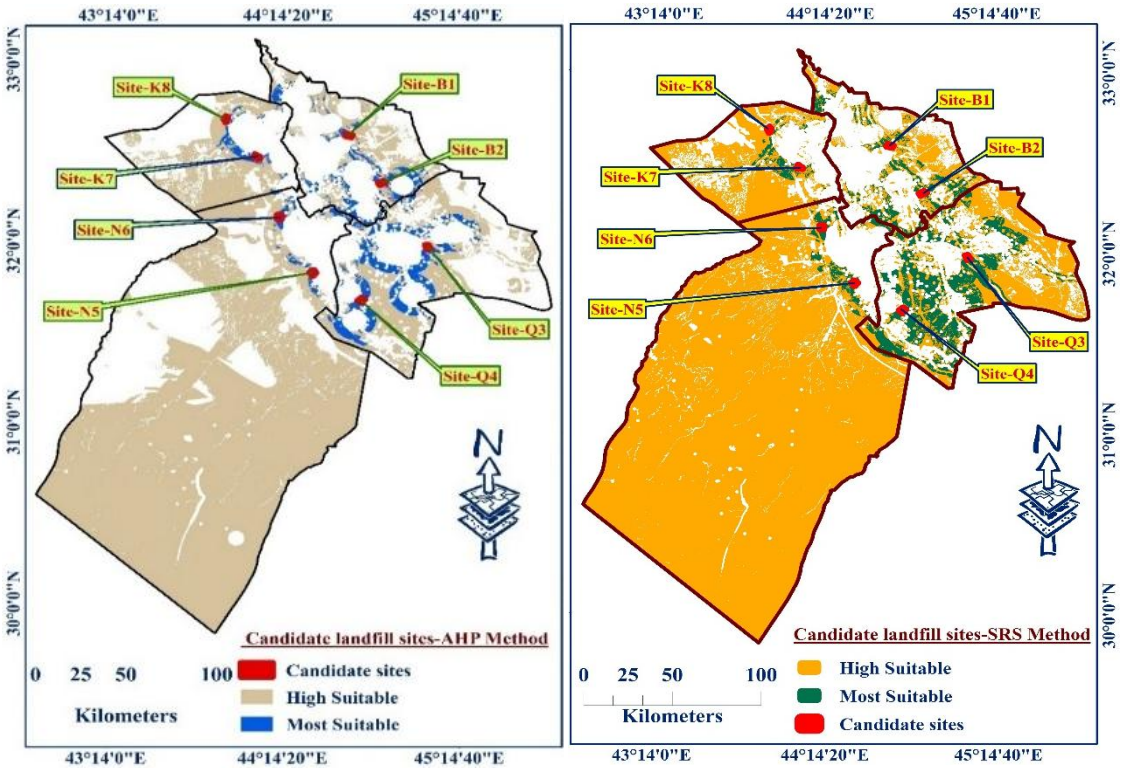

Fig. 6. Candidate landfill sites within the high and most suitable classes using MCDM methods.

Table 9 presents the spatial extent of the identified candidate landfill sites alongside the land area available there to accommodate the total volume of waste generated in the Middle Euphrates provinces over the period of 2024–2040. It should be noted that the calculated landfill area is based on waste volume and assumed landfill geometry, and therefore represents a minimum theoretical

requirement. In practice, the total land area needed for landfill is substantially larger due to the inclusion of other infrastructure and operational facilities. These usually include internal and access roads, parking areas, security zones, administrative buildings, leachate management systems, vehicle washing facilities, and areas reserved for future expansion and environmental protection measures. Consequently, candidate sites with areas only marginally exceeding the calculated disposal requirement may not be sufficient to support long-term landfill operation. However, the sites offering significantly larger areas provide greater operational flexibility, allow for phased development, and improve compliance with environmental and safety regulations. This consideration is particularly important for regional landfill planning, where facilities are expected to serve multiple cities in a large region and accommodate fluctuations in waste generation rates over time. Finally, detailed site-specific investigations, including geotechnical surveys and infrastructure planning, are required to confirm whether the identified candidate sites can realistically meet the waste management needs of the region and the candidate sites have favorable land ownership conditions.

Table 9. Suggested locations and required areas for landfill sites in the study area for the period of 2024 to 2040.

Province	Area km^2	Site symbol	Required area km^2
Babylon	6.1	Site B1	4.34
	7.4	Site B2	
Al-Qadisyiah	6.0	Site Q3	2.10
	7.2	Site Q4	
Al-Najaf	7.3	Site N5	2.75
	6.8	Site N6	
Karbala	5.6	Site K7	2.35
	5.0	Site K8	

Several studies have investigated before landfill siting in different regions of Iraq using GIS-based multi-criteria decision-making (MCDM) approaches. Similar to previous studies the present study employs GIS-based spatial analysis and MCDM techniques to evaluate landfill suitability by considering key environmental and planning constraints relevant under Iraqi conditions. However, this study differs from previous studies by emphasizing on future-oriented planning instead of current conditions and investigating four provinces of Middle Euphrates Region besides integration of regulatory and regional constraints. Former studies focused on a single governorate, usually <3000 km² , often only one administrative unit. For instance, Chabuk et al. [58] evaluated fifteen criteria layers and located ten sites for different district of Babylon Governorate. They looked for small and local landfills for individual districts, while this study adopts a strategic regional landfill siting approach, identifying two large-capacity landfill sites designed to meet the long-term waste management needs up to 2040. Ishaq et al. [59] and Salman and Hamdan [60] each expored landfill siting within limited local areas i.e. Tal Afar and Al-Zubair districts, respectively. Ishaq et al. [59] only coniser six key factors while Salman and Hamdan [60] evaluated nine criteria and suggested one suitable site within the study area considering long-term capacity. Al-Alanbari and Ensaif [61] considered 19 criteria layers including socioeconomic, accessibility, infrastructure, morphology, and hydrology criteria along the Karbala governorate and found ten suitable candidate landfill sites in the local scale.

Iraq lacks unified national regulations specifically governing landfill siting, while the accessibility of reliable spatial and environmental data is limited. As a result, researchers have independently selected decision criteria based on data availability and perceived importance, with the number of criteria varying widely, typically ranging from 6 to 19. Moreover, most existing studies are confined to individual cities or single governorates and are primarily based on current conditions, without incorporating future waste generation or long-term planning considerations. In this context, the present study addresses a critical gap by overcoming data scarcity through data integration and by extending the analysis to a larger regional scale, encompassing four governorates within Iraq's Middle Euphrates Region. By adopting a regional and future-oriented GIS-based MCDM framework, this study represents one of the first efforts to support long-term landfill siting and waste management planning beyond localized case studies in Iraq.

5. Conclusion

Waste disposal facilities in Iraq's Middle Euphrates region aren't meeting environmental and engineering standards. Switching from open dumping to sanitary landfill is considered a crucial first step toward sustainable waste management in Iraq. This transition helps to reduce environmental pollution by controlling leachate and gas emissions, improving public health, and enabling better waste management practices in the region with minimal funding and maximum efficiency. This study aimed to demonstrate the effectiveness of integrating Geographic Information Systems (GIS) with multi-criteria decision making (MCDM) techniques for addressing the complex challenge of municipal solid waste landfill site selection on a larger scale in Iraq's Middle Euphrates region. Efforts are made to plan for future waste management scenarios that accommodate population growth, tourism-related waste production, and evolving waste generation patterns. Also, work is carried out to follow suitable selection procedures while reducing environmental concerns and considering local social problems. To develop a decision-making process, sixteen layers of criteria were added to GIS. The layers, in order of significance, included urban area, villages, groundwater depth, rivers, main highways, secondary roads, elevation, slope, soil types, airports, land use, archaeological sites, power lines, railroads, and wind. For determining the criteria weightings, MCDM utilized the AHP and SRS methods. The weighted linear combination (WLC) process was then applied to create final maps of suitable landfill sites in the Middle Euphrates region by multiplying each criterion weight by its corresponding sub-criterion weights. The results highlight that a substantial proportion of the study area is restricted due to environmental sensitivity and regulatory limitations, underscoring the necessity of science-based planning approaches in waste

management. Eight landfilling sites were identified in the study provinces, with two sites allocated to each province. Based on the final maps generated by the AHP and SRS methods, these sites were chosen within areas classified as highly suitable and most suitable. The area of the selected sites is sufficient to handle all the waste produced from 2024 to 2040 in the Middle Euphrates provinces, when compared to the required area for each province. The main novelty of this study lies in the integrated application of GIS with two distinct weighting approaches (AHP and SRS) at a national planning scale, enabling a transparent comparison between expert-based and rank-based decision-making frameworks. Overall, this research demonstrates that GIS–MCDM frameworks are well suited for supporting sustainable waste management strategies in Iraq. By linking spatial suitability analysis with future waste generation projections and site capacity assessment, the study provides planning-oriented outputs that go beyond conventional landfill siting maps and offer practical decision support for solid waste management in Iraq. Future studies should focus on integrating higher-resolution spatial data, sensitivity and uncertainty analyses, and dynamic urban growth scenarios into a nation wide strategic planning. Expanding this approach to other regions of Iraq would contribute to the development of a unified, science-based national strategy for sanitary landfill planning and environmental protection.

Statements & Declarations

Author contributions

Ammar Rasheed Al-Hamami: Conceptualization, Formal analysis, Writing - Original Draft.

OzeairAbessi: Supervision, Methodology, Data curation , Writing - Review & Editing.

Ali Chabuk: Supervision, Investigation, Validation, Visualization, Writing.

Funding

The authors received no financial support for the research, authorship, and/or publication of this article.

Data availability

The data presented in this study will be available on interested request from the corresponding author.

Declarations

The authors declare no conflict of interest.

References

[1] Shuokr Qarani Aziz, Hamidi Abdul Aziz, Mohammed Jk Bashir, Mohd Suffian Yusoff Appraisal of domestic solid waste generation, components, and the feasibility of recycling in Erbil, Iraq. Waste Management & Research, 2011; 29: 880–887. doi:10.1177/0734242X10387462.

[2] Peyravi, M., Abessi, O., Aghadadashi, S., Jahanshahi, M. Principles of design and operation of landfill sites and leachate treatment (Master Thesis). Babol (IR): Babol Noshirvani University of Technology; 2022 (In Persian).

[3] Femi, F., Oluwole, O. Management of Municipal Solid Waste (PhD Thesis). Lagos (NG): University of Lagos; 2013.

[4] Unnisa, S. A., Rav, S. B. Sustainable Solid Waste Management. 1st ed. Boca Raton (FL): CRC Press; 2012. doi:10.1201/b13116.

[5] Malmir, T., Tojo, Y. Municipal solid waste management in Tehran: Changes during the last 5 years. Waste Management & Research, 2016; 34: 449–456. doi:10.1177/0734242X16632056.

[6] Zurbrugg, C. Urban Solid Waste Management in Low-Income Countries of AsiaHow to Cope with the Garbage Crisis. In: Scientific Committee on Problems of the Environment (SCOPE), Urban Solid Waste Management Review Session; 2002 Nov 1–2; Durban, South Africa. p. 1–13.

[7] Amirsoleymani, Y., Abessi, O., Ebrahimian Ghajari, Y. Evaluation of spatial restriction for the urban sanitary landfill along the Mazandaran province using GIS and analytical hierarchy process. Advanced Environmental Sciences, 2020; 18: 1–20. doi:10.52547/envs.18.4.1.

[8] Al-Anbari, M. A., Thameer, M. Y., Al-Ansari, N. Landfill site selection by weighted overlay technique: case study of Al-Kufa, Iraq. Sustainability, 2018; 10: 999. doi:10.3390/su10040999.

[9] Wang, G., Qin, L., Li, G., Chen, L. Landfill site selection using spatial information technologies and AHP: A case study in Beijing, China. Journal of Environmental Management, 2009; 90: 2414–2421. doi:10.1016/j.jenvman.2008.12.008.

[10] Amirsoleymani, Y., Abessi, O., Ghajari, Y. E. A spatial decision support system for municipal solid waste landfill sites (case study: The Mazandaran Province, Iran). Waste Management & Research, 2022; 40: 940–952. doi:10.1177/0734242X211060610.

[11] Proske, H., Vlcko, J., Rosenbaum, M. S., Dorn, M., Culshaw, M., Marker, B. Special purpose mapping for waste disposal sites. Bulletin of Engineering Geology and the Environment, 2005; 64: 1–54. doi:10.1007/s10064-004-0261-6.

[12] Rezaeisabzevar, Y., Bazargan, A., Zohourian, B. Landfill site selection using multi criteria decision making: Influential factors for comparing locations. Journal of Environmental Sciences, 2020; 93: 170–184. doi:10.1016/j.jes.2020.02.030.

[13] Aksoy, E., San, B. T. Geographical information systems (GIS) and Multi-Criteria Decision Analysis (MCDA) integration for sustainable landfill site selection considering dynamic data source. Bulletin of Engineering Geology and the Environment, 2019; 78: 779–791. doi:10.1007/s10064-017-1135-z.

[14] Elkhrachy, I., Alhamami, A., Alyami, S. H. Landfill site selection using multi-criteria decision analysis, remote sensing data, and geographic information system tools in Najran City, Saudi Arabia. Remote Sensing, 2023; 15: 3754. doi:10.3390/rs15153754.

[15] Saha, P., Roy, M. Identification of municipal solid waste disposal sites for sustainable solid waste management in Cooch Behar Municipality, West Bengal: A RS-GIS based MCDA approach. Waste Management Bulletin, 2024; 2: 127–144. doi:10.1016/j.wmb.2024.07.004.

[16] Sharma, K., Tiwari, R., Wadhwani, A. K., Chaturvedi, S. An integrated GIS-MCDM framework for zoning, ranking and sensitivity analysis of municipal landfill sites. Sustainable and Resilient Infrastructure, 2025; 10: 313–335. doi:10.1080/23789689.2024.2404279.

[17] Chaturvedi, S., Bhatt, N., Shah, V., Jodhani, K. H., Patel, D., Singh, S. K. Landfill site selection in hilly terrains: An integrated RS-GIS approach with AHP and VIKOR. Waste Management Bulletin, 2025; 3: 332–348. doi:10.1016/j.wmb.2025.01.010.

[18] Al-Mamoori, S. K., Al-Maliki, L. A., Hussain, H. M., Al-Ali, M. J. Geotechnical Mapping for Some Chemical Properties of an-Najaf Province Using GIS. Kufa Journal of Engineering, 2018; 9: 92–113.

[19] Chabuk, A. Solid waste landfills in an arid environment: Site selection and design (PhD Thesis). Luleaa (SE): Luleå University of Technology; 2019.

[20] Ghazal, N. K., Hussein, A. K. Accuracy Assessment of Land Use and Land Cover Classification of AL-Najaf Province, Iraq. Journal of Kufa Physics, 2017; 9: 72–79.

[21] Al Khalidy, K., Chabuk, A., Kadhim, M. Measurement of lead pollution in the air of Babylon Governorate, Iraq during year 2010. World Academy of Science, Engineering and Technology, 2012; 62: 826–829.

[22] Iraqi Ministry of Planning. IMP: Records of the Directorate of the Ministry, Internal reports. Baghdad (IQ): Republic of Iraq - Ministry of Planning; 2024.

[23] Abdulredha, M., khaddar, R. A. L., Jordan, D., Hashim, K. The Development of a Waste Management System in Kerbala during Major Pilgrimage Events: Determination of Solid Waste Composition. Procedia Engineering, 2017; 196: 779–784. doi:10.1016/j.proeng.2017.08.007.

[24] Alkhuzaie, M. M., Janna, H. Optimum location for landfills sites based on GIS modeling for Al-Diwaniyah City, Iraq. International Journal of Civil Engineering and Technology, 2018; 9: 941–951.

[25] Shaker, A. S., Mohammed, F. S., Al-Shebani, H. Quantity, quality and cost of household waste in al-diwaniyah governorate. Al-Qadisiyah Journal for Agriculture Sciences, 2021; 11: 78–84. doi:10.33794/qjas.2021.170227.

[26] Zambrano-Monserrate, M. A., Ruano, M. A., Ormeño-Candelario, V. Determinants of municipal solid waste: a global analysis by countries' income level. Environmental Science and Pollution Research, 2021; 28: 62421–62430. doi:10.1007/s11356-021-15167-9.

[27] Al-Anbari, M., Thameer, M., Al-Ansari, N., Knutsson, S. Landfill site selection in Al-Najaf governorate, Iraq. Journal of Civil Engineering and Architecture, 2016; 10: 651–660. doi:10.17265/1934-7359/2016.06.003.

[28] Soils and Soil Conditions in Iraq. Baghdad (IQ): Republic of Iraq - Ministry of Agriculture; 1960.

[29] Isalou, A. A., Zamani, V., Shahmoradi, B., Alizadeh, H. Landfill site selection using integrated fuzzy logic and analytic network process (F-ANP). Environmental Earth Sciences, 2013; 68: 1745–1755. doi:10.1007/s12665-012-1865-y.

[30] A. Effat, H., N. Hegazy, M. Mapping potential landfill sites for North Sinai cities using spatial multicriteria evaluation. The Egyptian Journal of Remote Sensing and Space Science, 2012; 15: 125–133. doi:10.1016/j.ejrs.2012.09.002.

[31] Sener, B. Mapping Potential Landfill Sites for North Sinai Cities (Master Thesis). Ankara (TR): Middle East Technical University; 2004.

[32] Uyan, M. MSW landfill site selection by combining AHP with GIS for Konya, Turkey. Environmental Earth Sciences, 2014; 71: 1629–1639. doi:10.1007/s12665-013-2567-9.

[33] Sadek, S., El-Fadel, M., Freiha, F. Compliance factors within a GIS-based framework for landfill siting. International Journal of Environmental Studies, 2006; 63: 71–86. doi:10.1080/00207230600562213.

[34] Moeinaddini, M., Khorasani, N., Danehkar, A., Darvishsefat, A. A., zienalyan, M. Siting MSW landfill using weighted linear combination and analytical hierarchy process (AHP) methodology in GIS environment (case study: Karaj). Waste Management, 2010; 30: 912–920. doi:10.1016/j.wasman.2010.01.015.

[35] Delgado, O. B., Mendoza, M., Granados, E. L., Geneletti, D. Analysis of land suitability for the siting of inter-municipal landfills in the Cuitzeo Lake Basin, Mexico. Waste Management, 2008; 28: 1137–1146. doi:10.1016/j.wasman.2007.07.002.

[36] Eskandari, M., Homaee, M., Mahmodi, S. An integrated multi criteria approach for landfill siting in a conflicting environmental, economical and socio-cultural area. Waste Management, 2012; 32: 1528–1538. doi:10.1016/j.wasman.2012.03.014.

[37] Yildirim, V. Application of raster-based GIS techniques in the siting of landfills in Trabzon Province, Turkey: a case study. Waste Management & Research, 2012; 30: 949–960. doi:10.1177/0734242X12445656.

[38] Kara, C., Doratli, N. Application of GIS/AHP in siting sanitary landfill: a case study in Northern Cyprus. Waste Management & Research, 2012; 30: 966–980. doi:10.1177/0734242X12453975.

[39] Sharifi, M., Hadidi, M., Vessali, E., Mosstafakhani, P., Taheri, K., Shahoie, S., Khodamoradpour, M. Integrating multi-criteria decision analysis for a GIS-based hazardous waste landfill sitting in Kurdistan Province, western Iran. Waste Management, 2009; 29: 2740–2758. doi:10.1016/j.wasman.2009.04.010.

[40] Demesouka, O. E., Vavatsikos, A. P., Anagnostopoulos, K. P. Suitability analysis for siting MSW landfills and its multicriteria spatial decision support system: Method, implementation and case study. Waste Management, 2013; 33: 1190–1206. doi:10.1016/j.wasman.2013.01.030.

[41] Şener, B., Süzen, M. L., Doyuran, V. Landfill site selection by using geographic information systems. Environmental Geology, 2006; 49: 376–388. doi:10.1007/s00254-005-0075-2.

[42] Ersoy, H., Bulut, F. Spatial and multi-criteria decision analysis-based methodology for landfill site selection in growing urban regions. Waste Management & Research, 2009; 27: 489–500. doi:10.1177/0734242X08098430.

[43] Kontos, T. D., Komilis, D. P., Halvadakis, C. P. Siting MSW landfills on Lesvos island with a GIS-based methodology. Waste Management & Research, 2003; 21: 262–277. doi:10.1177/0734242X0302100310.

[44] Alkaradaghi, K., Ali, S. S., Al-Ansari, N., Laue, J., Chabuk, A. Landfill site selection using MCDM methods and GIS in the Sulaimaniyah Governorate, Iraq. Sustainability, 2019; 11: 4530. doi:10.3390/su11174530.

[45] Thapa, R. B., Murayama, Y. Land evaluation for peri-urban agriculture using analytical hierarchical process and geographic information system techniques: A case study of Hanoi. Land Use Policy, 2008; 25: 225–239. doi:10.1016/j.landusepol.2007.06.004.

[46] Nas, B., Cay, T., Iscan, F., Berktay, A. Selection of MSW landfill site for Konya, Turkey using GIS and multi-criteria evaluation. Environmental Monitoring and Assessment, 2010; 160: 491–500. doi:10.1007/s10661-008-0713-8.

[47] Jassim, S. Z., Goff, J. C. Geology of Iraq. 1st ed. Baghdad (IQ): DOLIN, sro, distributed by Geological Society of London; 2006.

[48] González, A., Kelly, C., Rymszewicz, A. Advancements in web-mapping tools for land use and marine spatial planning. Transactions in GIS, 2020; 24: 253–267. doi:10.1111/tgis.12603.

[49] Rezaei-Moghaddam, K., Karami, E. A multiple criteria evaluation of sustainable agricultural development models using AHP. Environment, Development and Sustainability, 2008; 10: 407–426. doi:10.1007/s10668-006-9072-1.

[50] Saaty, T. L. The Analytic Hierarchy Process: Planning, Priority Setting, Resource Allocation. 1st ed. New York (NY): McGraw-Hill International Book Company; 2008.

[51] Sólnes, J. u. Environmental quality indexing of large industrial development alternatives using AHP. Environmental Impact Assessment Review, 2003; 23: 283–303. doi:10.1016/S0195-9255(03)00004-0.

[52] Alonso, J. A., Lamata, M. T. Consistency in the analytic hierarchy process: a new approach. International journal of uncertainty, fuzziness and knowledge-based systems, 2006; 14: 445–459. doi:10.1142/S0218488506004114.

[53] Coyle, G. Practical strategy: structured tools and techniques. ed. Pearson Education; 2004.

[54] Setiawan, A., Sediyono, E., Moekoe, D. A. Application of AHP method in determining priorities of conversion of unusedland to food land in Minahasa Tenggara. International Journal of Computer Applications, 2014; 89: doi:10.5120/15526-4433.

[55] El Alfy, Z., Elhadary, R., Elashry, A. Integrating GIS and MCDM to deal with landfill site selection. International Journal of Engineering & Technology, 2010; 10: 32–42.

[56] UNEP Solid Waste Management. 2nd ed. New York (NY): United Nations Environment Programme (UNEP); 2005.

[57] Ho, G. International Source Book on Environmentally Sound Technologies (ESTs) for Municipal Solid Waste Management (MSWM). 1st ed. New York (NY): UNEP Division of Technology, Industry and Economics International (UNEP-IETC); 2006.

[58] Chabuk, A., Al-Ansari, N., Hussain, H. M., Laue, J., Hazim, A., Knutsson, S., Pusch, R. Landfill sites selection using MCDM and comparing method of change detection for Babylon Governorate, Iraq. Environmental Science and Pollution Research, 2019; 26: 35325–35339. doi:10.1007/s11356-019-05064-7.

[59] Ishaq, B. Y., Qasim, A. F., Faisal, R. M. Using the GIS application and multi-criteria analysis to determine to optimal site for solid waste landfill in Tal Afar district. Journal of Rafidain Environment, 2025; 2: 31–48. doi:10.33899/jre.v3i2.49932.

[60] Salman, Q., Hamdan, A. Landfill site selection using analytical hierarchy process and GIS: a case study in Al-Zubair district, Basrah, Iraq. Muthanna Journal of Engineering and Technology, 2024; 12: doi:10.52113/3/eng/mjet/2024-12-02/50-61.

[61] Al-Alanbari, M., Ensaif, Y. R. Landfill Site Selection in Karbala Governorate, Iraq. Journal of Engineering and Sustainable Development, 2018; 22: 30–42. doi:10.31272/jeasd.2018.6.4.

Civil Engineering and Applied Solutions

Research Article

journal homepage: ceas.journals.umz.ac.ir

CEAS Civil Engineering and Applied Solutions

Evaluation of Car Following Driver Behavior: A Systematic Review

Mirbahador Yazdani [a], Hadi Shadlouy [a*], Bahram Shirini [a], Omar Faraji [a], Jamshid Nazari [a]

[a] *Faculty of Engineering, Bonab University, Bonab, Iran*

ARTICLE INFO

Keywords:
Car-following behavior
Driver behavior
Traffic safety
Risk assessment

Article history:
Received 21 November 2025
Accepted 23 April 2026
Available online 01 October 2026

ABSTRACT

Investigating car-following driver behavior is essential for increasing traffic safety, optimizing transportation, and developing autonomous vehicle technology. This importance has made studying this behavior in complex traffic situations and in autonomous vehicles a key research topic. The present survey provides a comprehensive overview of driver behavior in car-following with a focus on the period from 2015 to 2025. The search involving all databases combined yielded 3,870 original articles, of which 10 relevant ones were included for detailed qualitative and comparative reading. The survey underscores important behavior variables: time headway, reaction time, braking behavior, and lane-changing behavior with disparate research approaches in driving simulators, naturalistic driving data, and simulation models. Empirical evidence is provided that driver distraction, hostile driving, and high-tech automated systems greatly affect car-following behavior and traffic safety. Additionally, the need for adaptable models is illustrated through the variations across regions and societies, influencing both parameter tuning and the cross-context applicability of car-following models. Sample size variation among studies provides evidence of the importance of combining detailed individual-level data with broader system-level analysis. The review identifies gaps in geographical range, particularly in low- and middle-income countries, and calls for further studies combining naturalistic driving data and customized behavioral models to promote the safety and efficacy of car-following systems worldwide.

1. Introduction

The mobility interaction of a following vehicle in relation to the vehicle directly ahead of it is referred to as car-following behavior [1]. The constant movement within car-following behavior occurs when a driver adjusts their speed, acceleration, or headway based on their reading of the movement of the lead vehicle [2]. Car-following behavior contributes to traffic safety, traffic operations, energy consumption, and overall driving comfort [3]. Safe and consistent time headway is required to prevent rear-end crashes and minimize fuel consumption and emissions [4-6]. Driver attention, perception-reaction time, risk perception, and aggression [7].

In this case, car-following behavior is essential for conducting microscopic traffic modeling based on real driver behavior, and the technology aspect of conducting e-safety work is crucial for Advanced Driver-Assistance Systems (ADAS) and Connected Autonomous Vehicles (CAVs) [8, 9]. The driver's individual characteristics (e.g., age, identification as male, driving experience, risk tolerance, cognitive capability) are crucial in understanding how a driver follows another vehicle [10-14].

The robustness of modeling and predicting car-following behavior will also be impacted by environmental factors (such as road geometry, weather, and traffic density) and vehicle characteristics (such as vehicle size, acceleration, braking systems, and visibility) [15, 16]. Emerging Advanced ADAS and CAVs will introduce new behavioral characteristics (such as following distance, reaction times, and trust in automation) that will alter the driver's expectations and develop new levels of anxiety and uncertainty when

* Corresponding author.
E-mail addresses: hadishadlouy@gmail.com (H. Shadlouy).

https://doi.org/10.22080/ceas.2026.30563.1054
ISSN: 3092-7749/
How to cite this article: Yazdani, M., Shadlouy, H., Shirini, B., Faraji, O., Nazari, J. Evaluation of Car Following Driver Behavior: A Systematic Review. Civil Engineering and Applied Solutions. 2026; 2(4): 60-68. doi:10.22080/ceas.2026.30563.1054.

following a vehicle [17-19]. While driving simulators and controlled experimental conditions offer repeatable, safe environments to study car-following behavior, they do not include many facets of naturalistic driving behavior, leading to the need for context-relevant, multi-faceted approaches to study car-following behavior in various settings and under various conditions [20-25].

The landscape of car-following behavior has changed due to the advent of advanced intelligent transportation technologies like ADAS, CAVs, and Cooperative Adaptive Cruise Control (CACC) [26-28]. Although these technologies increase safety, reduce driver burden while driving, and improve travel efficiency [29], drivers may have varying degrees of trust, flexibility, and situational awareness when interacting with automation and other connected devices/systems [30, 31].

Numerous methods have been used in empirical research to investigate car-following behavior [3, 32]. For instance, McNabb et al. compared how drivers behaved in a "follow-a-friend" scenario with a typical following scenario using a driving simulator [33]. Using the technique of investigating distraction in a platoon, Xu and Lin investigated the impact of distraction propagation. In their experimental study, they discovered that all subsequent drivers may experience a change in gap and a delayed reaction time if the lead driver is distracted [34]. When Goncu et al. used a SUMO simulation to examine car-following behavior in Germany and Turkey, they discovered differences that matched the local traffic culture norms [35].

At present, there are chances to streamline and improve the generalizability of the literature through the construction of a systematic outline that organizes and integrates the outcomes against each of the determinants of the driver's characteristics, scenario, technology use, and cultural background. By organizing, connecting, and comparing studies, we aim to build on this knowledge of car-following behaviors across different contexts and uncover wider behavioral patterns or trends moving forward [36]. Moreover, we aim to provide guidance on the development of future and more inclusive models of car-following behavior [37].

This review categorizes studies based on dimensions, such as driving scenario, type of distraction, and driver characteristics. This review brings together previous studies and highlights less explored aspects of contextual differences in driving behavior, and the changes in technology found within vehicles. This study seeks to create a conceptual framework for future research on the topics of assistance systems, data-driven smart transportation, and modeling techniques that analyze traffic behavior.

Section 2 provides details on the methodology used for the systematic review, including the search strategy and the eligibility requirements. The main conclusions are presented and discussed in Section 3, including where they occurred, how people behaved, what caused them to lose concentration and what helped them, and the most significant findings of the research that was examined. The work is concluded in Section 4, which summarizes the main conclusions, identifies research gaps, and suggests areas for further study.

2. Methodology

In order to fully understand the existing literature on driver behavior when driving behind other vehicles and its traffic safety implications, a systematic review of the literature was conducted. The review aimed at locating, critiquing, and synthesizing relevant.

2.1. Search strategy

Relevant articles were retrieved from Scopus, Web of Science, and IEEE Xplore. The search was performed using the following combination of keywords: ("driver behavior" OR "driving behavior") AND ("following vehicles" OR "car-following" OR "tailgating") AND ("traffic safety" OR "road safety") AND ("risk assessment" OR "reaction time").

A detailed scrutiny of 3,870 published articles related to car-following driver behavior, traffic safety, risk, and reaction time was undertaken with a focus on the period from 2015 to 2025. In accordance with PRISMA guidelines, the screening phase of articles included multiple steps, such as the elimination of duplicate articles, a preliminary scrutiny of article titles and abstracts, and a detailed scrutiny of articles that qualified after abstract scrutiny. Additional criteria that were used towards the elimination of articles included the absence of relevance with respect to car-following driver behavior, inadequate description of methods, inadequate data, and a lack of synchrony with the review period. After a thorough examination of papers pertinent to the review and meeting its publishing deadline, ten articles with the greatest level of rigor and relevance were ultimately shortlisted. A PRISMA flowchart (Fig. 1) graphically depicts the selection of articles as well as the quantity of articles in the scrutiny stage. The final ten papers underwent a thorough analysis with the goal of identifying the most important conclusions and any gaps in driver behavior during car following. The detailed exclusion criteria applied at each screening stage are summarized in Table 1, in accordance with the PRISMA framework.

3. Result and discussion

This systematic review contrasts car-following driver behavior research from various countries, methodologies, and regions [38]. Ten studies were selected, each of which considered various aspects, including time headway, reaction time, lane-changing behavior, braking behavior, and traffic flow stability [39]. The literature was compared primarily using driving simulators and model-based simulation, with some using naturalistic driving data or mixed-method designs [40]. External perturbations like driver distraction, aggressive driving styles, and automated systems were also taken into account. Findings show that such factors can significantly alter car-following behavior, either introduce safety hazards or modify system performance.

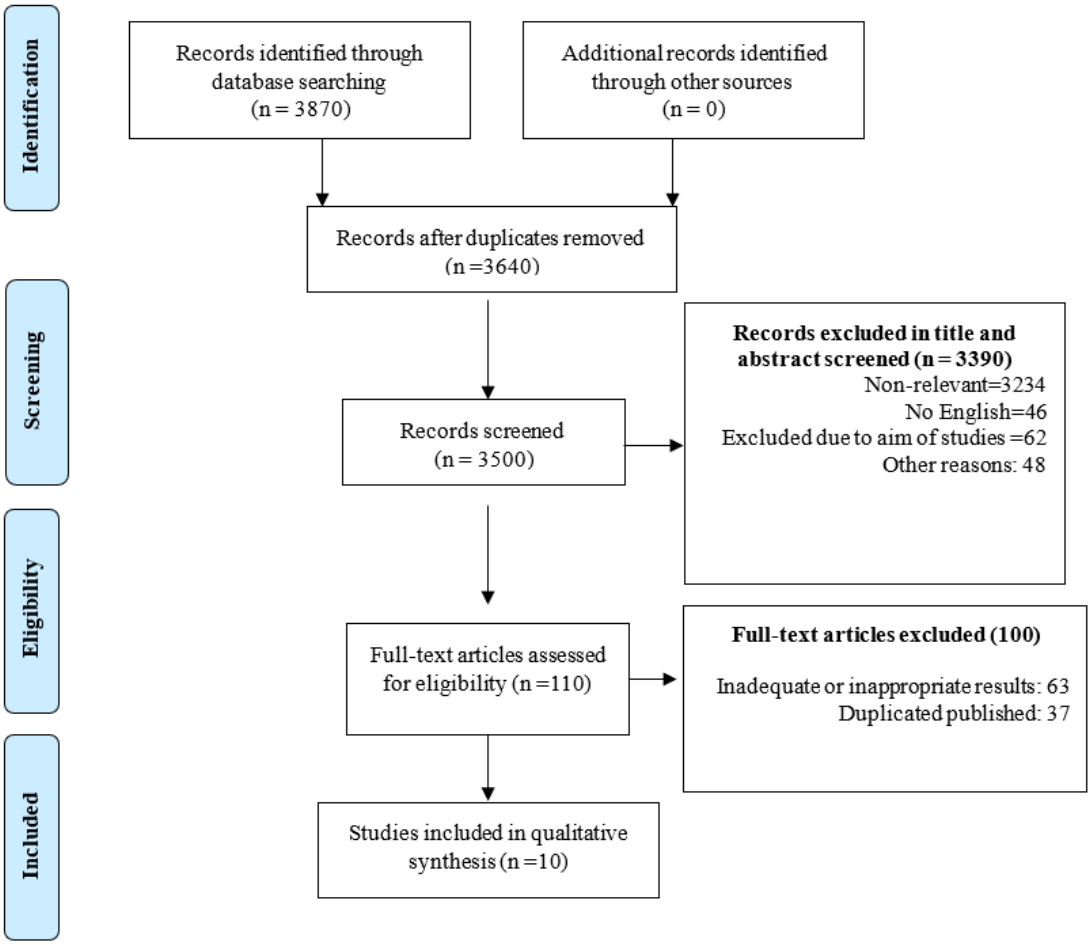

Fig. 1. PRISMA flowchart.

Table 1. Eligibility criteria for article selection before PRISMA-based screening.

Screening stage	Exclusion criterion	Number of excluded records	Explanation
Duplicate removal	Duplicate records	230	Records appearing more than once across databases were removed prior to screening.
Title & abstract screening	Not relevant to car-following behavior	3,234	Studies not directly addressing car-following behavior, driver behavior, or related traffic safety aspects.
Title & abstract screening	Non-English publications	46	Articles not published in English were excluded to ensure consistent interpretation.
Title & abstract screening	Outside study objectives	62	Studies focusing on unrelated traffic topics without behavioral or car-following relevance.
Title & abstract screening	Other reasons	48	Editorials, conference abstracts, commentaries, or papers lacking sufficient scientific content.
Full-text eligibility assessment	Inadequate or inappropriate results	63	Full-text articles lacking empirical results or methodological rigor relevant to car-following behavior.
Full-text eligibility assessment	Duplicate publications	37	Studies reporting overlapping or previously published results were excluded.
Final inclusion	Studies included in qualitative synthesis	10	Studies meeting all inclusion criteria and selected for in-depth qualitative analysis.

Several studies also mentioned the impact of cultural or traffic system differences on the applicability and calibration of car-following models [41, 42]. Each study was presented in detail, including the driving scenario, intervention type, behavioral measures, and key findings (Table 2).

3.1. Geographical distribution and regional focus in car-following behavior research

The studies on car-following behavior reveal global trends and regional variability. The United States (US) contains the largest number of studies, reflecting a large research infrastructure and an emphasis on the research of connected vehicle technologies. Germany, Turkey, India, China, Canada, Japan, and Australia are contributing to the research community in car-following behavior as well, which is important for illustrating real-world behaviors or culturally influenced behavior, and shows the need for cultural and regional calibration of car-following models.

Table 2. Studies summary.

No.	Author(s) and year	Country name	Sample size	Distraction / Intervention	Behavioral variables	Key findings
1	McNabb et al., 2017 [33]	USA	16 drivers	None	Speed, Time Headway, Lane Change	"Follow-a-friend" increases risky behavior
2	Xu & Lin, 2018 [34]	USA	36 (12 platoons)	Cellphone texting	Reaction Time, Headway	Distraction spreads behavioral risk in a platoon
3	Zhou et al., 2023 [43]	USA	72 participants	CAV control settings	Time headway, CF behavior, Lane change	CF behavior affected by CAV control, congestion, and demographics; string-stable CAV preferred
4	Goncu et al., 2022 [35]	Turkey & Germany	Model-based	None	Traffic flow, Throughput	Cultural differences affect CF modeling
5	Adavikottu et al., 2023 [44]	India	58 drivers	Aggression profile	Tailgating, Reaction Delay	Aggressive drivers show higher tailgating & crash risk
6	Fricke et al., 2015 [45]	Germany	40 drivers	System intervention	Brake/steer reaction	Users resist automation unless briefed in advance
7	Ozkan & Ma, 2021 [46]	Canada	Not stated	CAV interaction	Fuel use, Following pattern	CAV improves follower fuel use; varies by driver type
8	Hatazawa et al., 2023 [47]	Japan	Not stated	LSTM modeling	Model accuracy (R^2)	LSTM models benefit from tuning; high personalization potential
9	Rahman et al., 2017 [48]	USA	Model-based	CACC system	Acceleration, String Stability	OVM model offers better comfort/dynamics than IDM
10	Hussain et al., 2025 [49]	Australia (based on institutional affiliations)	61 participants	Speed limit + lead vehicle	Rear-end risk, Headway, Demographics	Female, young, and low-experience drivers = higher crash risk

However, the presence of regionally-informed studies indicates that behavioral tendencies are not universally consistent and that transportation systems or driver assistance technology may not apply or translate cleanly from one region to another. The review encourages a higher proportion of geographically representative studies in the future, especially in low-and-middle income countries with typical driver behavior and relevant regulatory context that may differ markedly from high-income countries. This is necessary for developing adaptive and globally relevant car-following models that will contribute to improved safety and system efficiency in increasingly diverse traffic environments [50].

3.2. Sample size

The studies reviewed for car-following behavior analysis have different sample sizes, which were based on several factors, including experimental groups, models, and the exact number of participants was often not disclosed. The differences in sample size reflect the differences in methodology and served a different research purpose. Even though conducting research with a small sample size permits greater detail in the analysis of individual-level behavior, a smaller sample size will limit generalizing findings to other populations. Traffic bottlenecks and system-level interventions have been the main focus of model-based and simulation-based research. They typically don't, however, offer insights into behavioral analysis at the individual level. Larger and more varied sample sizes are generally better at approximating individual variability in driver attributes (e.g., age, gender, or driving experience) that are directly linked to risk and car-following behavior. In order to improve future repeatability and support more thorough meta-analyses, several researchers failed to disclose the sample size in their study. The aforementioned assessment of car-following behaviors' variations in sample size offers valuable opportunities to investigate both macroscopic traffic system dynamics and microscopic driver behavior [16, 36, 51]. In order to improve the ecological validity of studies that simulate car-following behavior, future research should benefit from bigger, more diversified sample sizes as well as sample sizes collected through naturalistic driving.

3.3. Distraction and intervention factors

Fig. 2 illustrates the effects of different distractions and interventions on driving behavior using the index of Normalized Behavioral Change Index (NBCI) measures. The index measures the variations in the following distances away from a baseline standard of a safe following distance. A positive index score represents greater instability and increased variations in distances, and a negative index score represents stabilizing effects, which improve safe distances. The analysis shows that the main risk factors for behavior are closely linked to aggressive driving and influence from others, which suggests a significant increase in NBCI, around +0.6 to +0.8. Cognitive distractions, like texting while driving, lead to a moderate increase in risk, with an NBCI value of about +0.15. On the other hand, speed control rules and limits from the vehicle in front show a lower but steady risk effect, with an NBCI of about +0.25. On the other side of how things are being implemented, there are technological tools like Cooperative Adaptive Cruise Control (CACC), Connected & Autonomous Vehicles (CAV), and the Long Short-Term Memory (LSTM) Control System. These tools have a negative effect on NBCI, which means they help make driver behavior more stable. The effect ranges from -0.15 to -0.25. This outcome makes it clear how technological tools are capable of effectively decreasing the deviations observed in the safe following distance.

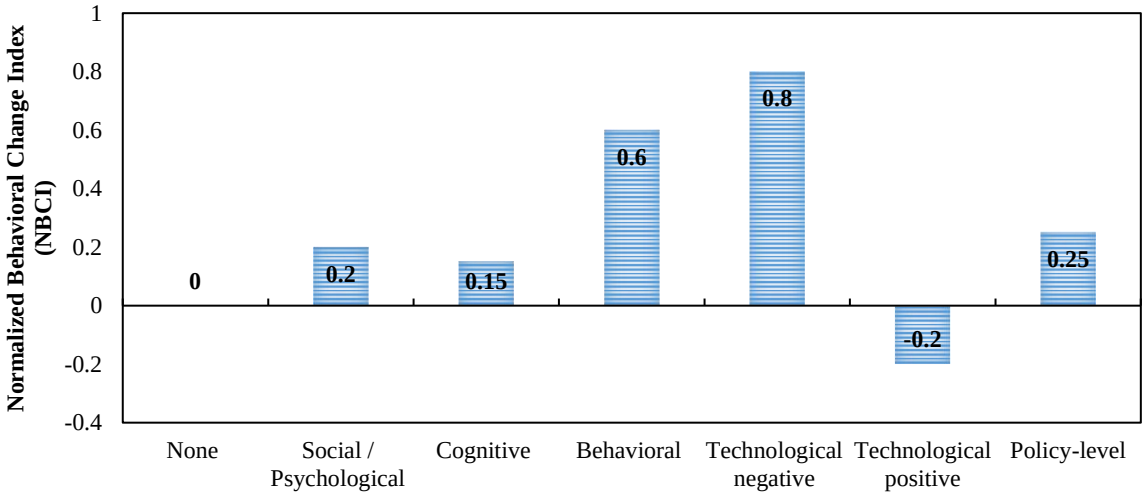

Fig. 2. Normalized Behavioral Change Index (NBCI) across different distraction and intervention types in car-following behavior studies.

3.4. Behavioral variables

Researchers use a variety of behavioral variables in the studies included in this review, such as system-level, driver reaction, and temporally/spatially defined measures. Time headway, gap distance, gap speed, and other factors are both geographically and temporally specified. Researchers are interested in how closely and safely drivers follow lead vehicles in car-following experiments that use these metrics [52]. Reaction time, trajectory adjustment timing, steering inputs, and avoidance behaviors are examples of driver response metrics. These metrics evaluate a driver's ability to react to traffic's dynamic alterations. The efficiency and safety of the wider traffic system are also measured by researchers using system-level and modeling metrics, such as flow, throughput, string stability, and fuel consumption.

The variety of behavioral variables used in the studies in this review highlights the complexity of car-following behavior and illustrates the need for models studying car-following behavior to move towards a holistic understanding that combines micro-level human responses to traffic change with macro-level system performance indicators (Fig. 3). Additionally, some studies include extended variables that can adequately describe events like lane changes, tailgating behavior, and demographic measures of drivers. These extended variables can help provide additional insight into the heterogeneity present within driver populations and indicate that more individualized approaches are likely required in the study of traffic behavior.

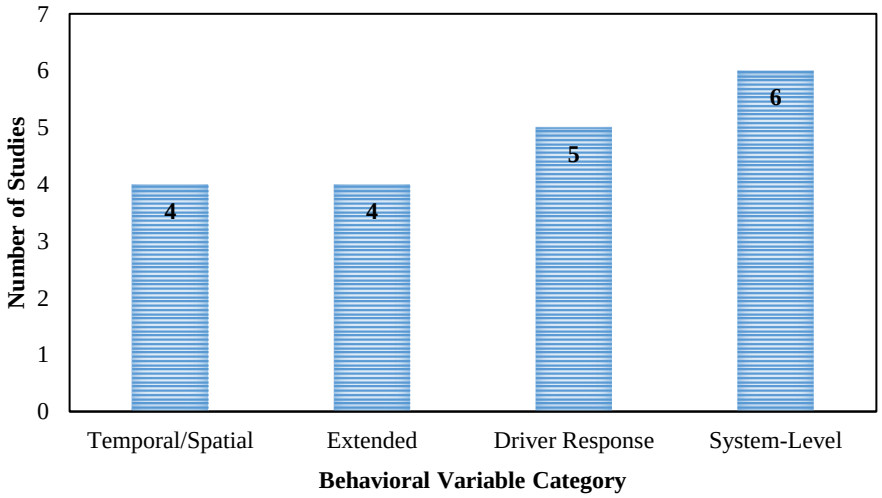

Fig. 3. Study distribution by behavioral variable category.

3.5. Key findings

Behavioral risk factors, driver variability, technological influence, and modeling implications are the four primary categories into which each of the previous studies divides the complex structure of car-following behavior (Fig. 4). Additionally, specific situations described as greater headways are necessary for car-following behaviors; this cluster is known as Behavioral Risk Factors [53, 54]. Driver demographics also play a role, as seen by the increased risk of rear-end crashes for young, female, and inexperienced drivers [55]. Automation and technology solutions have conflicting effects. While CACC improves string stability and comfort, user resistance to automation unless drivers are properly briefed reduces the advantages. These issues are exacerbated by culturally specialized AI, culturally impacted modeling, and customized prediction models. In order to develop culturally acceptable adaptive

driver technologies, it is important to address all of these levels. The research highlights that the effectiveness of the assistance systems is increased when these technologies are tailored to the unique regional features.

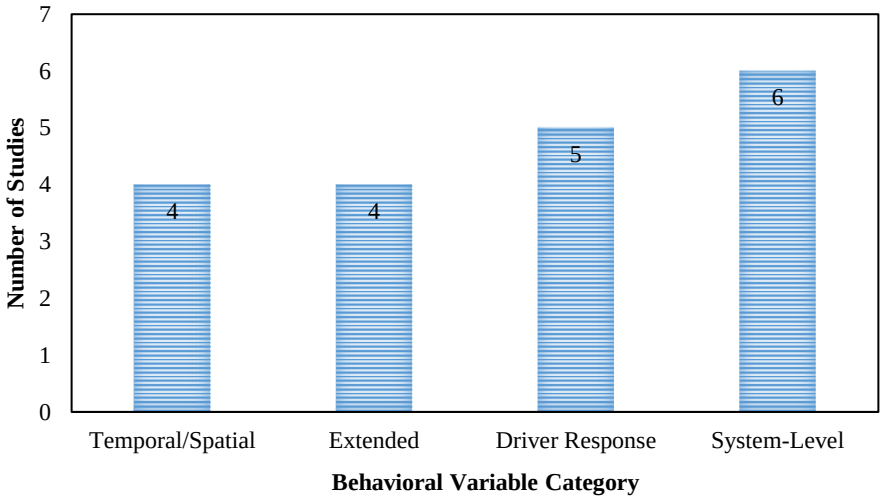

Fig. 4. Number of reviewed studies by category of key findings.

4. Conclusion

This study examines how people drive when they are following another car. It discusses the various factors that can influence this behavior, including the road they are driving on and the technology in the vehicle. It also looks at what other people have discovered about this topic. The following are the main points this study makes about people driving when they are following another car:

- Describes how automated driving features, aggressive driving, and attention-related factors affect car-following behavior.
- Car-following models and driver assistance systems should be applied appropriately to specific situations; this means that these models and systems should be tailored for different contexts and should not be universally applied to all traffic scenarios.
- Car-following models and driver assistance systems need to consider the traffic circumstances; they are not good for every situation; they should be made to fit the context in which they are being used.
- Highlights the consequences for safety analysis, traffic simulation research, and the creation of adaptive driver support systems.
- Determines that in order to enhance external validity, further studies with bigger sample sizes and naturalistic driver observations are required.
- Draws attention to the spatial concentration limitations of current studies and suggests broadening the scope of research.
- Recommends improving car-following models to include both system-level and individual behavioral components.

Statements & Declarations

Author contributions

Mirbahador Yazdani: Investigation, Formal analysis, Data curation, Software, Writing - Original Draft.

Hadi Shadlouy: Project administration, Supervision, Resources, Writing - Review & Editing.

Bahram Shirini: Conceptualization, Methodology, Software, Writing - Review & Editing.

Omar Faraji: Conceptualization, Methodology, Software, Writing - Review & Editing.

Jamshid Nazari: Conceptualization, Methodology, Software, Writing - Review & Editing.

Funding

The authors received no financial support for the research, authorship, and/or publication of this article.

Data availability

The data presented in this study will be available on interested request from the corresponding author.

Declarations

The authors declare no conflict of interest.

References

[1] Han, J., Wang, X., Wang, G. Modeling the car-following behavior with consideration of driver, vehicle, and environment factors: A historical review. Sustainability, 2022; 14: 8179. doi:10.3390/su14138179.

[2] Wang, Y., Zhang, J., Lu, G. Influence of Driving Behaviors on the Stability in Car Following. IEEE Transactions on Intelligent Transportation Systems, 2019; 20: 1081–1098. doi:10.1109/TITS.2018.2837740.

[3] Mohammadi, S., Arvin, R., Khattak, A. J., Chakraborty, S. The role of drivers' social interactions in their driving behavior: Empirical evidence and implications for car-following and traffic flow. Transportation Research Part F: Traffic Psychology and Behaviour, 2021; 80: 203–217. doi:10.1016/j.trf.2021.04.002.

[4] Vaezipour, A., Rakotonirainy, A., Haworth, N. Reviewing In-vehicle Systems to Improve Fuel Efficiency and Road Safety. Procedia Manufacturing, 2015; 3: 3192–3199. doi:10.1016/j.promfg.2015.07.869.

[5] Rajaram, V., Subramanian, S. C. Heavy vehicle collision avoidance control in heterogeneous traffic using varying time headway. Mechatronics, 2018; 50: 328–340. doi:10.1016/j.mechatronics.2017.11.010.

[6] Wu, Y., Abdel-Aty, M., Wang, L., Rahman, M. S. Combined connected vehicles and variable speed limit strategies to reduce rear-end crash risk under fog conditions. Journal of Intelligent Transportation Systems, 2020; 24: 494–513. doi:10.1080/15472450.2019.1634560.

[7] Wu, D., Lee, J. J., Li, Y., Jin, J. Exploring driving behavioral characteristics in pre-, in-, and post-conflict stages based on car-following trajectory data. Ergonomics, 2025; 68: 1025–1042. doi:10.1080/00140139.2024.2388696.

[8] Calvert, S. C., Schakel, W. J., van Arem, B. Evaluation and modelling of the traffic flow effects of truck platooning. Transportation Research Part C: Emerging Technologies, 2019; 105: 1–22. doi:10.1016/j.trc.2019.05.019.

[9] Olstam, J., Johansson, F., Alessandrini, A., Sukennik, P., Lohmiller, J., Friedrich, M. An Approach for Handling Uncertainties Related to Behaviour and Vehicle Mixes in Traffic Simulation Experiments with Automated Vehicles. Journal of Advanced Transportation, 2020; 2020: 8850591. doi:10.1155/2020/8850591.

[10] Tan, D., Tian, W., Wang, C., Chen, L., Xiong, L. Driver distraction behavior recognition for autonomous driving: Approaches, datasets and challenges. IEEE Transactions on Intelligent Vehicles, 2024; 9: 8000 – 8026. doi:10.1109/TIV.2024.3405990.

[11] Mobini Seraji, M. H., Shaffiee Haghshenas, S., Shaffiee Haghshenas, S., Simic, V., Pamucar, D., Guido, G., Astarita, V. A state-of-the-art review on machine learning techniques for driving behavior analysis: clustering and classification approaches. Complex & Intelligent Systems, 2025; 11: 386. doi:10.1007/s40747-025-01988-5.

[12] Witt, M., Kompaß, K., Wang, L., Kates, R., Mai, M., Prokop, G. Driver profiling – Data-based identification of driver behavior dimensions and affecting driver characteristics for multi-agent traffic simulation. Transportation Research Part F: Traffic Psychology and Behaviour, 2019; 64: 361–376. doi:10.1016/j.trf.2019.05.007.

[13] Brown, T. G., Ouimet, M. C., Eldeb, M., Tremblay, J., Vingilis, E., Nadeau, L., Pruessner, J., Bechara, A. The effect of age on the personality and cognitive characteristics of three distinct risky driving offender groups. Personality and Individual Differences, 2017; 113: 48–56. doi:10.1016/j.paid.2017.03.007.

[14] Hulse, L. M., Xie, H., Galea, E. R. Perceptions of autonomous vehicles: Relationships with road users, risk, gender and age. Safety Science, 2018; 102: 1–13. doi:10.1016/j.ssci.2017.10.001.

[15] Hamdar, S. H., Qin, L., Talebpour, A. Weather and road geometry impact on longitudinal driving behavior: Exploratory analysis using an empirically supported acceleration modeling framework. Transportation Research Part C: Emerging Technologies, 2016; 67: 193–213. doi:10.1016/j.trc.2016.01.017.

[16] Munigety, C. R., Mathew, T. V. Towards Behavioral Modeling of Drivers in Mixed Traffic Conditions. Transportation in Developing Economies, 2016; 2: 6. doi:10.1007/s40890-016-0012-y.

[17] Guo, F. Statistical methods for naturalistic driving studies. Annual review of statistics and its application, 2019; 6: 309–328. doi:10.1146/annurev-statistics-030718-105153.

[18] Papantoniou, P., Papadimitriou, E., Yannis, G. Review of driving performance parameters critical for distracted driving research. Transportation Research Procedia, 2017; 25: 1796–1805. doi:10.1016/j.trpro.2017.05.148.

[19] Caffò, A. O., Tinella, L., Lopez, A., Spano, G., Massaro, Y., Lisi, A., Stasolla, F., Catanesi, R., Nardulli, F., Grattagliano, I. The drives for driving simulation: a scientometric analysis and a selective review of reviews on simulated driving research. Frontiers in psychology, 2020; 11: 917. doi:10.3389/fpsyg.2020.00917.

[20] Jiang, R., Hu, M.-B., Zhang, H. M., Gao, Z.-Y., Jia, B., Wu, Q.-S. On some experimental features of car-following behavior and how to model them. Transportation Research Part B: Methodological, 2015; 80: 338–354. doi:10.1016/j.trb.2015.08.003.

[21] Fadhloun, K., Rakha, H. A novel vehicle dynamics and human behavior car-following model: Model development and preliminary testing. International Journal of Transportation Science and Technology, 2020; 9: 14–28. doi:10.1016/j.ijtst.2019.05.004.

[22] Ro, J. W., Roop, P. S., Malik, A., Ranjitkar, P. A formal approach for modeling and simulation of human car-following behavior. IEEE Transactions on Intelligent Transportation Systems, 2017; 19: 639–648. doi:10.1109/TITS.2017.2759273.

[23] Javanbakht, N., Mirbaha, B. Evaluating Drivers' Response to Road Hazard: A Simulation Study. Advances in Civil Engineering, 2024; 2024: 6788857. doi:10.1155/2024/6788857.

[24] Javanbakht, N., Mirbaha, B. A MODEL FOR EVALUATING DRIVERS'MEAN SPEED: USING PSYCHOLOGICAL AND DRIVING SIMULATOR DATA. Numerical Methods in Civil Engineering, 2023; 8: 48–55. doi:10.61186/NMCE.2303.1027.

[25] Javanbakht, N., Mirbaha, B. From Traits to Speed Control: Engineering Insights from a Driving-Simulator Hazard Scenario. Contributions of Science and Technology for Engineering, 2025; doi:10.22080/cste.2025.29839.1075.

[26] Ahmed, H. U., Huang, Y., Lu, P., Bridgelall, R. Technology developments and impacts of connected and autonomous vehicles: An overview. Smart Cities, 2022; 5: 382–404. doi:10.3390/smartcities5010022.

[27] Song, Z., Ding, H. Modeling car-following behavior in heterogeneous traffic mixing human-driven, automated and connected vehicles: considering multitype vehicle interactions. Nonlinear Dynamics, 2023; 111: 11115–11134. doi:10.1007/s11071-023-08377-y.

[28] Ahmed, H. U., Ahmad, S., Yang, X., Lu, P., Huang, Y. Safety and mobility evaluation of cumulative-anticipative car-following model for connected autonomous vehicles. Smart Cities, 2024; 7: 518–540. doi:10.3390/smartcities7010021.

[29] Eskandari Torbaghan, M., Sasidharan, M., Reardon, L., Muchanga-Hvelplund, L. C. W. Understanding the potential of emerging digital technologies for improving road safety. Accident Analysis & Prevention, 2022; 166: 106543. doi:10.1016/j.aap.2021.106543.

[30] Wang, X., Zhang, J., Li, H., He, Z. A mixed traffic car-following behavior model. Physica A: Statistical Mechanics and its Applications, 2023; 632: 129299. doi:10.1016/j.physa.2023.129299.

[31] Ahmed, H. U., Huang, Y., Lu, P. A review of car-following models and modeling tools for human and autonomous-ready driving behaviors in micro-simulation. Smart Cities, 2021; 4: 314–335. doi:10.3390/smartcities4010019

[32] Huang, Y.-X., Jiang, R., Zhang, H. M., Hu, M.-B., Tian, J.-F., Jia, B., Gao, Z.-Y. Experimental study and modeling of car-following behavior under high speed situation. Transportation Research Part C: Emerging Technologies, 2018; 97: 194–215. doi:10.1016/j.trc.2018.10.022.

[33] McNabb, J., Kuzel, M., Gray, R. I'll show you the way: Risky driver behavior when "following a friend". Frontiers in psychology, 2017; 8: 705. doi:10.3389/fpsyg.2017.00705

[34] Xu, J., Lin, Y. Impact of Distracted Drivers on Individual and Group Behavior of Following Vehicles: A Networked Multi-Driver Simulator Study. Transportation Research Record, 2018; 2672: 45–54. doi:10.1177/0361198118794712.

[35] Goncu, S., Erdagi, I. G., Silgu, M. A., Celikoglu, H. B. Analysis on effects of driving behavior on freeway traffic flow: A comparative evaluation of two driver profiles using two car-following models. In: 2022 IEEE Intelligent Vehicles Symposium (IV); 2022; p. 688–693. doi:10.1109/IV51971.2022.9827296

[36] Berthaume, A. L., James, R. M., Hammit, B. E., Foreman, C., Melson, C. L. Variations in Driver Behavior: An Analysis of Car-Following Behavior Heterogeneity as a Function of Road Type and Traffic Condition. Transportation Research Record, 2018; 2672: 31–44. doi:10.1177/0361198118798713.

[37] Negash, N. M., Yang, J. Driver behavior modeling toward autonomous vehicles: Comprehensive review. IEEE Access, 2023; 11: 22788–22821. doi:10.1109/ACCESS.2023.3249144.

[38] Gracian, V. A., Galland, S., Lombard, A., Martinet, T., Gaud, N., Zhao, H., Yasar, A.-U.-H. Behavioral models of drivers in developing countries with an agent-based perspective: a literature review. Autonomous Intelligent Systems, 2024; 4: 5. doi:10.1007/s43684-024-00061-1.

[39] Parashar, S., Zheng, Z., Rakotonirainy, A., Haque, M. M. Reassessing desired time headway as a measure of car-following capability: Definition, quantification, and associated factors. Communications in Transportation Research, 2025; 5: 100169. doi:10.1016/j.commtr.2025.100169.

[40] Mütsch, F., Gremmelmaier, H., Becker, N., Bogdoll, D., Zofka, M. R., Zöllner, J. M. From model-based to data-driven simulation: Challenges and trends in autonomous driving. arXiv preprint arXiv:2305.13960, 2023; doi:10.48550/arXiv.2305.13960

[41] van Hinsbergen, C. P. I. J., Schakel, W. J., Knoop, V. L., van Lint, J. W. C., Hoogendoorn, S. P. A general framework for calibrating and comparing car-following models. Transportmetrica A: Transport Science, 2015; 11: 420–440. doi:10.1080/23249935.2015.1006157.

[42] Zhang, T. T., Jin, P. J., McQuade, S. T., Bayen, A., Piccoli, B. Car-following models: A multidisciplinary review. IEEE Transactions on Intelligent Vehicles, 2024; doi:10.1109/TIV.2024.3409468

[43] Zhou, A., Liu, Y., Tenenboim, E., Agrawal, S., Peeta, S. Car-following behavior of human-driven vehicles in mixed-flow traffic: A driving simulator study. IEEE Transactions on Intelligent Vehicles, 2023; 8: 2661–2673. doi:10.1109/TIV.2023.3257962

[44] Adavikottu, A., Velaga, N. R., Mishra, S. Modelling the effect of aggressive driver behavior on longitudinal performance measures during car-following. Transportation Research Part F: Traffic Psychology and Behaviour, 2023; 92: 176–200. doi:10.1016/j.trf.2022.11.006.

[45] Fricke, N., Griesche, S., Schieben, A., Hesse, T., Baumann, M. Driver behavior following an automatic steering intervention. Accident Analysis & Prevention, 2015; 83: 190–196. doi:10.1016/j.aap.2015.07.018.

[46] Ozkan, M. F., Ma, Y. Modeling Driver Behavior in Car-Following Interactions With Automated and Human-Driven Vehicles and Energy Efficiency Evaluation. IEEE Access, 2021; 9: 64696–64707. doi:10.1109/ACCESS.2021.3075194.

[47] Hatazawa, Y., Hamada, A., Oikawa, S., Hirose, T. Construction of personalized driver model for car-following behavior on highways using LSTM. Journal of Advanced Mechanical Design, Systems, and Manufacturing, 2023; 17: JAMDSM0022–JAMDSM0022. doi:10.1299/jamdsm.2023jamdsm0022.

[48] Rahman, M., Chowdhury, M., Dey, K., Islam, M. R., Khan, T. Evaluation of driver car-following behavior models for cooperative adaptive cruise control systems. Transportation Research Record, 2017; 2622: 84–95. doi:10.3141/2622-08

[49] Hussain, Z., Mohammed, S. S., Dias, C., Hussain, Q., Alhajyaseen, W. K. M. Empirical analysis of car-following behavior: Impacts of driver demographics, leading vehicle types, and speed limits on driver behavior and safety. Transportation Research Part F: Traffic Psychology and Behaviour, 2025; 108: 188–205. doi:10.1016/j.trf.2024.11.022.

[50] Matcha, B. N., Namasivayam, S. N., Hosseini Fouladi, M., Ng, K. C., Sivanesan, S., Eh Noum, S. Y. Simulation Strategies for Mixed Traffic Conditions: A Review of Car-Following Models and Simulation Frameworks. Journal of Engineering, 2020; 2020: 8231930. doi:10.1155/2020/8231930.

[51] Zheng, L., Zhu, C., He, Z., He, T., Liu, S. Empirical validation of vehicle type-dependent car-following heterogeneity from micro- and macro-viewpoints. Transportmetrica B: Transport Dynamics, 2019; 7: 765–787. doi:10.1080/21680566.2018.1517057.

[52] Shi, X., Li, X. Empirical study on car-following characteristics of commercial automated vehicles with different headway settings. Transportation Research Part C: Emerging Technologies, 2021; 128: 103134. doi:10.1016/j.trc.2021.103134.

[53] Gulisano, F., Bella, F. Factors affecting motorcyclists' behavior in car-following condition. Transportation Research Part F: Traffic Psychology and Behaviour, 2021; 82: 1–14. doi:10.1016/j.trf.2021.07.014.

[54] Chen, S., Cheng, K., Yang, J., Zang, X., Luo, Q., Li, J. Driving behavior risk measurement and cluster analysis driven by vehicle trajectory data. Applied Sciences, 2023; 13: 5675. doi:10.3390/app13095675

[55] Rezapur-Shahkolai, F., Taheri, M., Etesamifard, T., Roshanaei, G., Shirahmadi, S. Dimensions of aberrant driving behaviors and their association with road traffic injuries among drivers. PLoS one, 2020; 15: e0238728. doi:10.1371/journal.pone.0238728.

Civil Engineering and Applied Solutions

Research Article

journal homepage: ceas.journals.umz.ac.ir

CEAS Civil Engineering and Applied Solutions

Numerical Analysis of Geocell-Reinforced Foundations under Varying Soil Conditions

Mohammad Javad Hosseinzadeh [a], Mohammad Oliaei [a*]

[a] *Department of Civil and Environmental Engineering, Tarbiat Modares University, Tehran, Iran*

ARTICLE INFO

Keywords:
Soil-reinforcement
Geosynthetic-reinforcement
Geocell
Numerical modelling

Article history:
Received 28 October 2025
Accepted 14 December 2025
Available online 01 October 2026

ABSTRACT

Soil behavior plays a critical role in the stability and performance of civil engineering infrastructures, often requiring reinforcement to enhance tensile strength and resistance to various load conditions. Geosynthetic materials, particularly geocells, have emerged as efficient reinforcement systems that significantly improve the mechanical behavior of soil. The purpose of this study is to evaluate the influence of soil strength parameters on the performance of geocell-reinforced foundations. A three-dimensional numerical model was developed using ABAQUS to simulate the mechanical response of a geocell-reinforced soil foundation. The model was validated against benchmark experimental and numerical data reported in previous studies to ensure reliability. The research employed a parametric analysis approach, varying key soil parameters, including the modulus of elasticity, internal friction angle, and specific gravity, to assess their effects on bearing capacity and settlement behavior. The results revealed that soils with higher modulus of elasticity, greater internal friction angle, and higher specific gravity demonstrated improved load-bearing performance and reduced settlement. Among these factors, the internal friction angle exerted the most pronounced impact, leading to substantial improvements in bearing pressure when the soil was reinforced with geocells. These findings highlight the importance of optimizing soil strength parameters in the design of geocell-reinforced foundations and provide a validated numerical framework for predicting their behavior under diverse loading conditions.

1. Introduction

Geotechnical engineering, a major branch of civil engineering, focuses on developing advanced and sustainable techniques to improve the strength, stability, and overall performance of soil in construction projects. Since soil forms the primary foundation for most civil infrastructure, its mechanical properties directly influence structural reliability. However, natural soils often lack sufficient tensile strength and stiffness to withstand applied loads, particularly when subjected to tensile or shear stresses. This inherent weakness has encouraged researchers and engineers to develop soil reinforcement strategies aimed at enhancing bearing capacity and reducing deformation under service conditions. Among the various reinforcement methods, geosynthetic materials have gained increasing attention for their versatility, cost-effectiveness, and environmental adaptability. Geosynthetics encompass a broad range of products, including geotextiles, geogrids, geomembranes, and geocells, that interact with soil to enhance its structural performance. Among these, geocells, also known as cellular confinement systems, have emerged as a superior form of reinforcement due to their unique three-dimensional honeycomb structure. When filled with soil or aggregate, geocells confine the infill material laterally, substantially improving load distribution and restricting vertical displacement.

The primary reason for the widespread adoption of geocells lies in their confinement mechanism, which significantly enhances the composite action between the geocell and the surrounding soil. This interaction leads to notable improvements in stiffness,

* Corresponding author.
E-mail addresses: m.olyaei@modares.ac.ir (M. Oliaei).

https://doi.org/10.22080/ceas.2025.30358.1051
ISSN: 3092-7749/
How to cite this article: Hosseinzadeh, M. J., Oliaei, M. Numerical Analysis of Geocell-Reinforced Foundations under Varying Soil Conditions. Civil Engineering and Applied Solutions. 2026; 2(4): 69-78. doi:10.22080/ceas.2025.30358.1051.

bearing capacity, and load transfer efficiency. Compared to unreinforced soil, geocell-reinforced soil exhibits reduced settlement and deformation, making it suitable for numerous civil engineering applications such as foundation beds, slope stabilization, road pavements, retaining walls, and erosion control. Fig. 1 illustrates the typical structure and mechanism of geocell reinforcement.

Fig. 1. Geocell reinforcement.

Several researchers have investigated the mechanical behavior of geocell-reinforced soils under various loading conditions. Sitharam and Hegde [1] demonstrated that geocell inclusion redistributes applied loads over a wider area, thereby reducing vertical stresses near the surface. Their study emphasized that geocell layers promote lateral load distribution, resulting in shallower stress transmission zones. Further research indicated that geocell reinforcement can significantly reduce fatigue failure and rutting in pavement structures [2]. Similarly, Banerjee et al. [3] observed that the inclusion of geocells reduces rut depth and local stress concentration, with performance strongly influenced by the height and geometry of the geocell layer. As shown in Fig. 2, geocells provide lateral confinement to soil via their three-dimensional structure. Vertical confinement is achieved through friction between the infill and cell walls, and the geocell-reinforced base acts as a mattress to restrict upward soil movement outside the area [4].

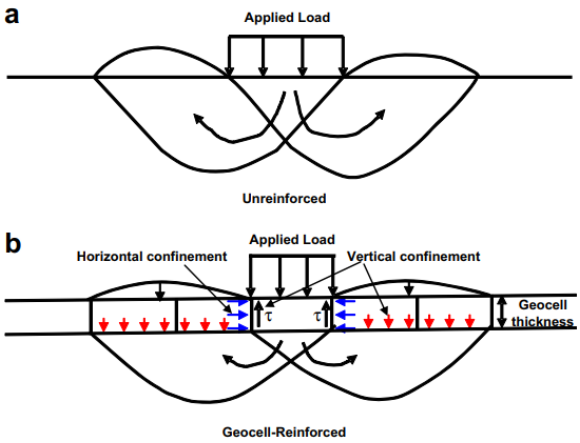

Fig. 2. Effect of geocell on stress distribution [4].

The mechanical advantages of geocell systems have been validated through numerous experimental and numerical studies. For example, Pokharel et al. [4] investigated how geocell shape, height, and infill properties influence the load-bearing behavior of single geocell-reinforced foundations. Their findings confirmed that the inclusion of geocells enhances soil confinement, leading to higher bearing capacities. Dash et al. [5, 6] conducted large-scale experiments on sand beds reinforced with geocell mattresses, revealing that reinforcement could increase the bearing capacity of sand up to eightfold. Likewise, Sireesh et al. [7] analyzed the effect of a geocell–sand mattress placed over a clay layer with voids, showing that settlement decreased markedly while bearing capacity improved.

To gain a deeper understanding of the complex behavior of geocell-reinforced foundations, advanced numerical techniques such as the Finite Element Method (FEM) and Finite Difference Method (FDM) have been employed. Hegde and Sitharam [8] and Mehdipour et al. [9] developed finite element models that represented geocell layers as equivalent stiffened soil zones, simplifying the confinement effect into an "equivalent modulus" framework. While these models improved computational efficiency, they lacked the precision required to capture the actual 3D mechanics and interface friction between the soil and the geocell walls. To address this limitation, Hegde and Sitharam [8] proposed a more realistic multi-cell numerical model incorporating the true curvature and shape of the geocell walls.

Recent developments in constitutive soil modeling have further expanded numerical capabilities. Heidarzadeh [10] evaluated the modified Cam-Clay constitutive model in FLAC and demonstrated how refined plasticity formulations can improve the representation of soil behavior under stress paths relevant to geocell–soil systems. The generalized plasticity constitutive model

proposed by Heidarzadeh and Oliaei [11] and the extended constitutive framework developed by Heidarzadeh et al. [12] highlight the importance of accurate soil characterization for reliable simulation outcomes. Additionally, Heidarzadeh and Kamgar [13] emphasized the necessity of incorporating steady-state concepts into numerical predictions of soil deformation, reinforcing the need for advanced constitutive models when analyzing soil–reinforcement interaction.

Further contributions from other researchers have expanded the modeling capabilities for geocell-reinforced systems. Hegde et al. [14] compared the performance of PLAXIS and ABAQUS in simulating reinforced foundations, concluding that FLAC3D provides superior element formulations for large-deformation analysis. Oliaei and Kouzegaran [15, 16] applied FLAC3D to evaluate geocell effects in both foundations and road base layers, confirming substantial improvements in stiffness and load distribution. Song et al. [17] studied geocell-reinforced retaining walls and demonstrated that reinforcement enhances base stiffness and durability while allowing thinner base layers. Ari and Misir [18] performed a comparative numerical investigation on shell foundations supported by geocell-reinforced soil, reporting a 70% reduction in settlement. Additionally, Juneja and Sharma [19] examined geometric parameters to determine optimal design configurations, concluding that a geocell layer height of 1.5B located at 0.1B depth yields optimal results. Evirgen et al. [20] combined numerical and experimental analyses using PLAXIS to confirm that geocells enhance both load-carrying capacity and deformation resistance of base layers.

Although extensive research has been conducted on geocell reinforcement, predicting the precise behavior of geocell-reinforced foundations remains a major challenge. The inherent three-dimensional geometry of the geocell, complex soil–structure interactions, and variability in soil properties all contribute to modeling difficulties. Simplified analytical and empirical methods often fail to represent these interactions with sufficient fidelity, underscoring the need for more robust, physics-based numerical models.

In the present study, a three-dimensional numerical model of a geocell-reinforced foundation bed was developed using ABAQUS software to provide a realistic representation of soil–geocell interaction. The model was validated against the benchmark results reported by Hegde and Sitharam [8] to ensure computational accuracy and physical reliability. The study focuses on assessing the influence of three key soil strength parameters, modulus of elasticity, internal friction angle, and unit weight, on the performance of geocell-reinforced foundations. By comparing the relative impact of these parameters, this work aims to identify the most critical soil characteristics affecting bearing capacity and settlement behavior.

The findings of this research provide valuable insights into the interaction mechanisms between geocell reinforcement and soil properties, contributing to improved design approaches for reinforced foundations. Moreover, the validated numerical framework developed herein serves as a reliable tool for predicting the performance of geocell-reinforced systems under varying soil and loading conditions, thereby advancing both theoretical understanding and practical applications in geotechnical engineering.

2. Numerical analysis

A three-dimensional numerical model was developed using the ABAQUS finite element software to evaluate the performance of geocell-reinforced foundations and to study the influence of various soil parameters on their bearing capacity. The research design involved two primary stages: validation of the numerical model and subsequent parametric analysis. To ensure the model's reliability, a reference study conducted by Hegde and Sitharam [8] was first replicated. Once the simulation results showed satisfactory agreement with their findings, the model was modified to investigate the effects of key parameters on the behavior of the reinforced foundation.

2.1. Validation model

Hegde and Sitharam [8] conducted numerical simulations by modeling the true three-dimensional honeycomb geometry of geocells using the FLAC3D software. In their study, a test tank was prepared with dimensions of 900 mm in length and width and 600 mm in height, as illustrated in Fig. 3. The foundation soil consisted of poorly graded sand (SP), whose physical and mechanical properties are presented in Table 1. The geocell layer was fabricated from polyethylene with cell dimensions of 250 × 210 mm and a strip thickness of 1.5 mm. Loading was applied to the reinforced soil through a square steel plate representing the foundation footing.

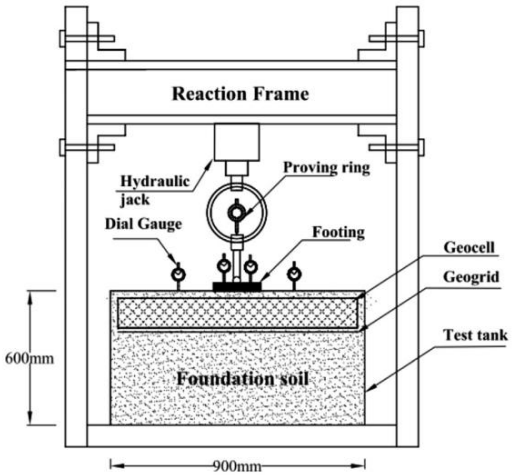

Fig. 3. Schematic view of the test setup [8].

Table 1. Properties of soil and geocell.

Parameter	Value	Parameter	Value
Sand		Geocell	
Elastic modulus (MPa)	15	Elastic modulus (MPa)	275
Poisson's ratio	0.3	Poisson's ratio	0.45
Cohesion (kPa)	0	Unit weight (kN/m^3)	9.5
Friction angle (deg.)	36		
Unit weight (kN/m^3)	20		

The researchers performed both two-dimensional and three-dimensional numerical analyses using FLAC. The two-dimensional analysis utilized the equivalent composite approach, which simplifies the reinforced zone but introduces certain uncertainties. In contrast, the three-dimensional model represented only a quarter of the test tank by applying symmetry conditions to reduce computational cost. The modeled domain measured 0.45 × 0.45 × 0.6 m, and the corresponding reinforced foundation configuration is presented in Fig. 4.

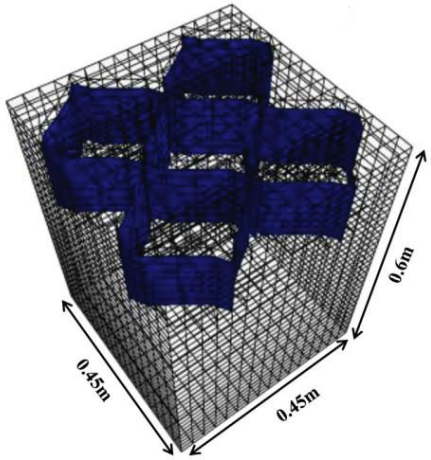

Fig. 4. FLAC 3D model for geocell reinforced foundation [8].

In the present study, a comparable three-dimensional model was constructed in ABAQUS to validate and extend the earlier findings. The geometric dimensions and material parameters from the reference study were adopted, with the geocell reinforcement placed at the top of the soil layer. The soil was modeled using the Mohr-Coulomb yield criterion to capture the nonlinear behavior under loading, whereas the geocell layer was represented by a linear elastic material model.

The simulation procedure consisted of two main steps. In the first step, a gravity load was applied to establish the initial in-situ stress conditions. In the second step, a vertical displacement of 50 mm was applied over a loading area measuring 100 × 100 mm, located at the corner of the model. The boundary conditions are explicitly defined as follows:

- Bottom boundary: Fully fixed (U1 = U2 = U3 = 0).
- Two lateral faces: Restrained against horizontal movement (U1 = 0 or U2 = 0), while allowing vertical displacement.
- Two perpendicular faces: Symmetry applied to simulate one-quarter of the full domain.
- Symmetry justification: Stress contours confirmed that deformation patterns remained symmetric.

The geometry and boundary setup of the model are depicted in Fig. 5.

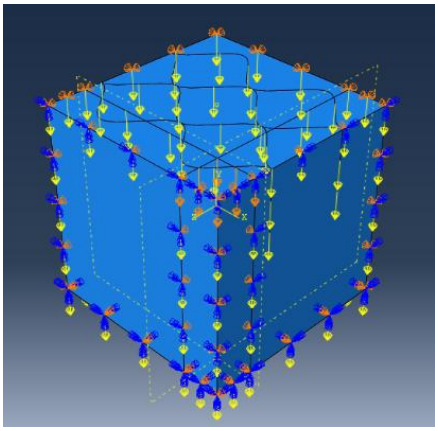

Fig. 5. Model with loading and boundary conditions.

The element type of soil was C3D8R (8-node linear brick, reduced integration, hourglass control) and for geocell M3D4R membrane elements (consistent with geocell behavior).Mesh convergence achieved when further refinement caused < 2% change in bearing capacity. The interaction between the geocell and the surrounding soil was modeled using the Embedded Region constraint. The geocell acted as the embedded region and the soil as the host region. This allows full kinematic compatibility without manually defining frictional contacts, consistent with validated geocell modeling literature.

NLGEOM was set to OFF, because settlements were small compared to model dimensions and enabling large deformation did not influence the load–settlement trends.The comparison between the results obtained from the present model and those reported by Hegde et al. is presented in Fig. 6. Minor differences may arise due to numerical differences between FLAC3D and ABAQUS, or parameters not explicitly specified by the original authors. Following successful validation, the model was subsequently modified to analyze the influence of soil properties and geocell characteristics on bearing capacity and settlement behavior.

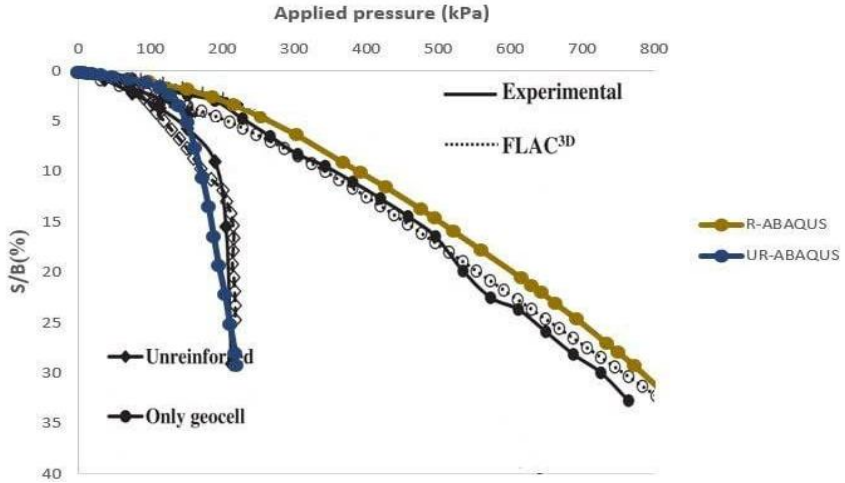

Fig. 6. Comparison of results with the verification article.

2.2. Numerical model

In this section, the details of the developed numerical model are presented. The model dimensions were slightly adjusted to 0.5 × 0.5 × 0.5 m. To examine the influence of soil strength parameters on the performance of geocell-reinforced foundation beds, a total of 48 simulation cases were created with varying soil properties to generate a consistent and comprehensive dataset. The soil parameters were selected based on an extensive review of soil mechanics and geotechnical engineering literature. The soil type used in this study corresponds to medium sand, characterized by a relative density ranging between 35 and 65 percent, as reported in standard references. The main soil properties adopted for the analysis are summarized in Table 2. Four different values were assigned for the elastic modulus and internal friction angle, while two values were used for the unit weight. A cohesion value of 10 kPa was assumed to simplify the numerical modeling process. All other model components and boundary conditions remained consistent with those used in the validation model.

Table 2. Numerical model soil parameters.

Parameter	Value
Elastic modulus (MPa)	30, 35, 40, 45
Poisson's ratio	0.3
Cohesion (kPa)	10
Friction angle (deg.)	30, 33, 36, 39
Unit weight (kN/m^3)	15, 16, 17

3. Results

This study investigates the effect of three soil parameters on the behavior of geocell-reinforced foundation beds. It discusses the effect of reinforcement, examines the impact of each parameter, and compares their relative influence.

3.1. Bearing capacity

Bearing capacity is one of the most critical performance indicators in foundation engineering. In this study, geocell-reinforced foundation beds were analyzed to highlight the effectiveness of this type of reinforcement in improving load-bearing performance. The bearing capacity ratio (BCR) is defined as the ratio between the bearing capacity of the reinforced foundation and that of the unreinforced foundation. The computed values for both reinforced and unreinforced bearing capacities, along with the corresponding BCR values, are presented in Table 3. The soil identification code used in the table consists of four components: "MS" denotes medium-density sand; "U" followed by a number indicates the unit weight in kilonewtons per cubic meter; "E" represents the elastic modulus; and the number following "F" specifies the internal friction angle in degrees.

Table 3. Bearing capacities and BCR.

Soil Code	qr (kPa)	qu (kPa)	BCR	Soil Code	qr (kPa)	qu (kPa)	BCR	Soil Code	qr (kPa)	qu (kPa)	BCR
MSU15E30F30	1120	495	2.26	MSU16E30F30	1130	505	2.24	MSU17E30F30	1135	510	2.23
MSU15E35F30	1130	500	2.26	MSU16E35F30	1135	510	2.23	MSU17E35F30	1140	520	2.19
MSU15E40F30	1135	510	2.23	MSU16E40F30	1145	520	2.20	MSU17E40F30	1155	525	2.20
MSU15E45F30	1145	520	2.20	MSU16E45F30	1150	525	2.19	MSU17E45F30	1155	535	2.16
MSU15E30F33	1415	690	2.05	MSU16E30F33	1420	695	2.04	MSU17E30F33	1425	705	2.02
MSU15E35F33	1420	700	2.03	MSU16E35F33	1425	705	2.02	MSU17E35F33	1430	715	2.00
MSU15E40F33	1425	705	2.02	MSU16E40F33	1430	710	2.01	MSU17E40F33	1440	720	2.00
MSU15E45F33	1430	710	2.01	MSU16E45F33	1435	720	1.99	MSU17E45F33	1440	730	1.97
MSU15E30F36	1740	985	1.77	MSU16E30F36	1755	995	1.76	MSU17E30F36	1760	1000	1.76
MSU15E35F36	1750	995	1.76	MSU16E35F36	1760	1005	1.75	MSU17E35F36	1765	1010	1.75
MSU15E40F36	1755	1000	1.76	MSU16E40F36	1765	1015	1.74	MSU17E40F36	1770	1020	1.74
MSU15E45F36	1770	1010	1.75	MSU16E45F36	1780	1020	1.75	MSU17E45F36	1785	1030	1.73
MSU15E30F39	2415	1445	1.67	MSU16E30F39	2420	1455	1.66	MSU17E30F39	2425	1460	1.66
MSU15E35F39	2420	1450	1.67	MSU16E35F39	2425	1465	1.66	MSU17E35F39	2430	1470	1.65
MSU15E40F39	2430	1460	1.66	MSU16E40F39	2430	1470	1.65	MSU17E40F39	2435	1475	1.65
MSU15E45F39	2435	1470	1.66	MSU16E45F39	2445	1480	1.65	MSU17E45F39	2455	1490	1.65

To ensure that the observed increases in bearing capacity were associated with realistic load-transfer mechanisms, the vertical stress contours, von Mises stress distribution, and plastic strain zones beneath the footing were examined for representative cases. In both reinforced and unreinforced soils, the stress bulbs developed in patterns consistent with classical bearing capacity theory. The presence of the geocell produced a wider, shallower stress distribution, confirming proper confinement and shear mobilization.

Three groups of soil samples were analyzed, each consisting of 16 variations with different values of unit weight, elastic modulus, and internal friction angle. Within each group, the soil strength increased progressively with the sample number. Consequently, the bearing pressure ratio (BPR) exhibited a gradual decrease, indicating a reduced influence of the geocell reinforcement as the soil became stronger. This trend is illustrated in Fig. 7. The observed improvement due to geocell reinforcement remained consistent across all 48 simulations. Although the magnitude of improvement decreased with increasing soil strength, the qualitative behavior, higher bearing capacity and reduced settlement in reinforced cases, was consistent throughout the entire parameter range.

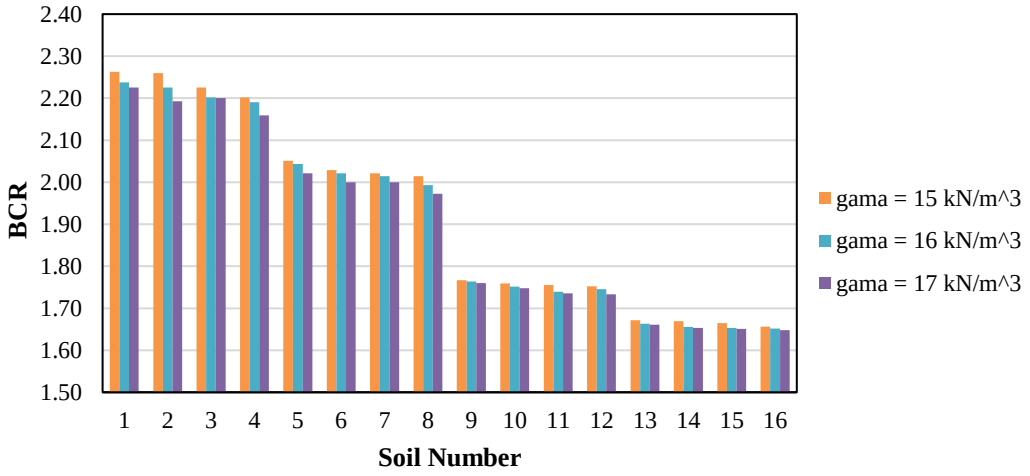

Fig. 7. BCR for different soil samples.

3.2. Effect of soil elastic modulus

The elastic modulus of a material reflects its stiffness and deformation response under applied loads and is a critical parameter in the design and analysis of foundations, slope stability, and retaining structures. It serves as one of the principal input variables in both finite element modeling and the Mohr-Coulomb failure criterion for simulating soil behavior. In this study, four elastic modulus values, 30, 35, 40, and 45 MPa, were selected for the numerical model to evaluate their effect on bearing capacity. The remaining soil parameters for these four cases are listed in Table 4. As illustrated in Fig. 8, an increase in the elastic modulus led to higher bearing pressures in both reinforced and unreinforced models. In the figure, the curves labeled with the letter “R” represent the reinforced versions of the corresponding samples.

Table 4. Soil parameters for samples 1-4.

Unit weight (kN/m^3)	Poisson's ratio	Soil code	Elastic modulus (MPa)
15	0.3	MSU15E30F30	30
Friction angle	**Cohesion (kPa)**	MSU15E35F30	35
30	10	MSU15E40F30	40
		MSU15E45F30	45

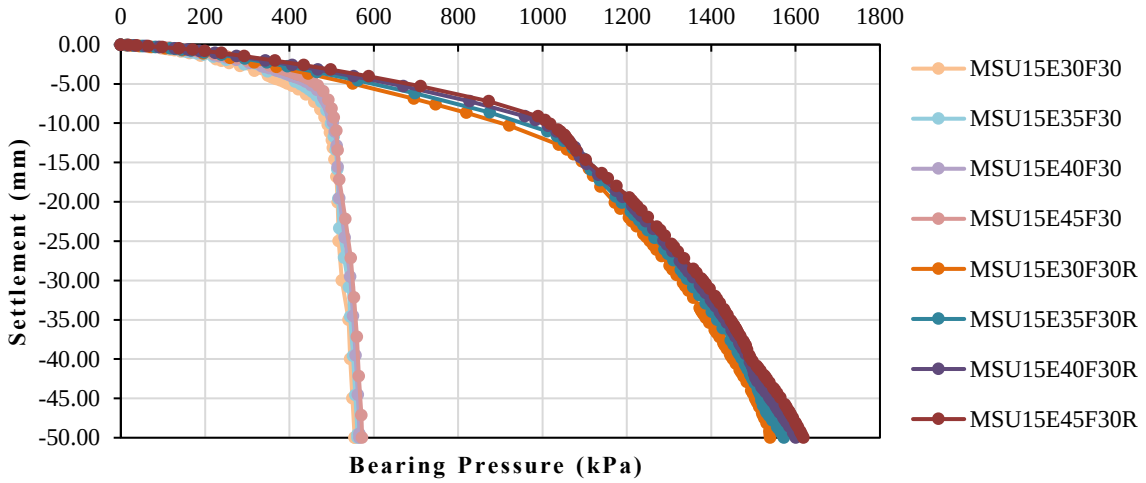

Fig. 8. Effect of soil elastic modulus on settlement.

The moderate influence of elastic modulus on bearing capacity indicates that stiffness governs the deformation response but does not significantly change the failure mechanism. The geocell provides lateral confinement, so increases in E produce diminishing returns once the soil stiffness exceeds the confinement stiffness provided by the geocell layer.

An increase of only 5 MPa in the soil's elastic modulus was found to enhance the bearing capacity of the foundation. On average, this improvement amounted to 0.46 percent in the reinforced samples and 1.03 percent in the unreinforced samples. However, as the internal friction angle of the soil increased, the influence of the elastic modulus on bearing capacity became less significant. Fig. 9 illustrates the average percentage increase in bearing capacity resulting from a 5 MPa increment in the soil's elastic modulus for both reinforced and unreinforced conditions.

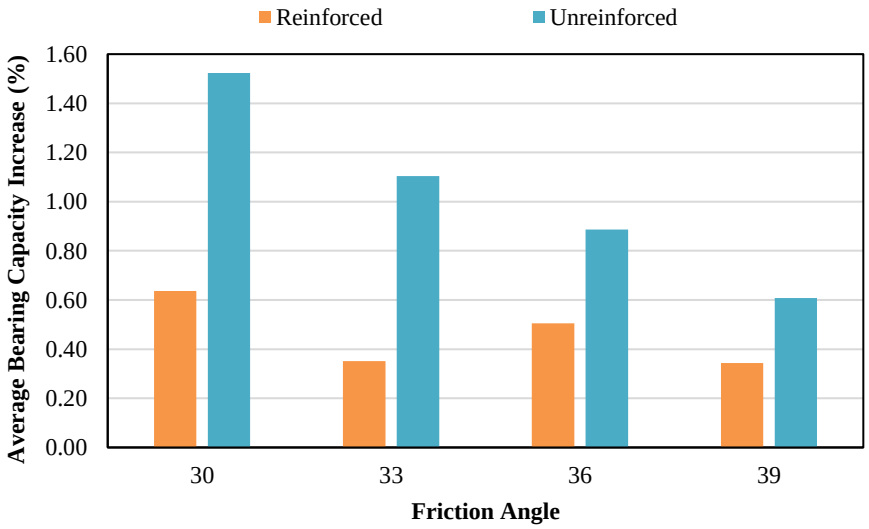

Fig. 9. Effect of elastic modulus on increasing bearing capacity.

3.3. Effect of soil friction angle

The internal friction angle is a key parameter representing the shear strength of soil. Based on the Mohr-Coulomb failure criterion, it defines the soil's resistance to shear deformation and failure. In this study, four friction angle values, 30, 33, 36, and 39 degrees, were assigned to the numerical model to examine their influence on the bearing capacity of the foundation. The remaining soil properties for these cases are provided in Table 5. Fig. 10 presents a comparison of the results for these soil models, illustrating the effect of increasing the friction angle on the foundation's bearing pressure. In the figure, curves labeled with the letter "R" correspond to the reinforced samples.

Table 5. Soil parameters for samples 44, 48, 52, 56.

Unit weight (kN/m^3)	Poisson's ratio	Soil code	Elastic modulus (MPa)
15	0.3	MSU15E30F30	30
Friction angle	**Cohesion (kPa)**	MSU15E30F33	33
30	10	MSU15E30F36	36
		MSU15E30F39	39

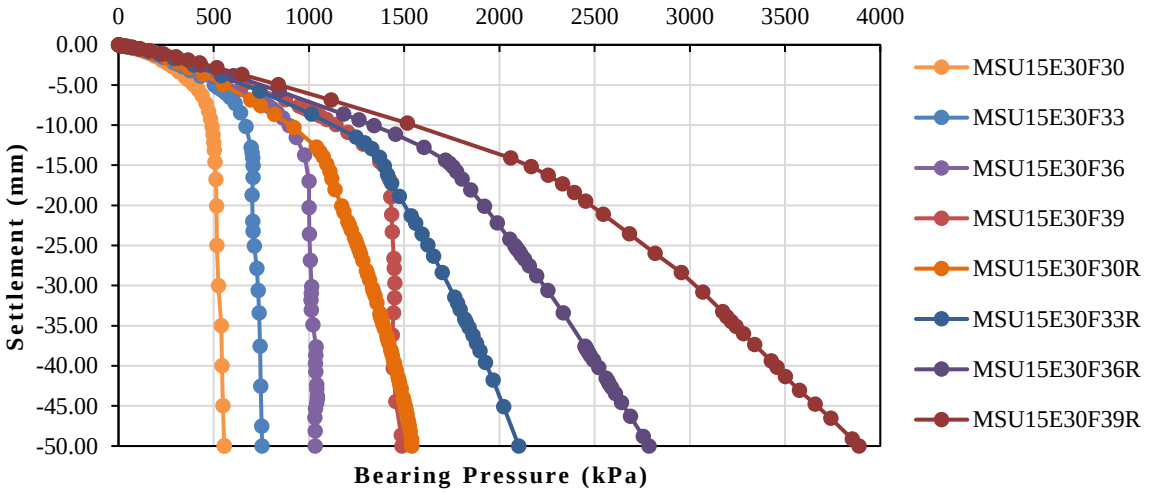

Fig. 10. Effect of friction angle on settlement.

An increase of only three degrees in the soil's friction angle was found to raise the foundation's bearing capacity by as much as 45 percent. For geocell-reinforced foundations, soils with higher elastic modulus exhibited a smaller improvement when the friction angle was increased. Moreover, the higher the initial friction angle of the soil, the greater the relative impact of this three-degree increment, as summarized in Table 6. The strong sensitivity to friction angle highlights that geocell systems perform best when combined with soils capable of mobilizing high shear resistance. In practice, this suggests that selecting granular infill with high φ, or improving in-situ soils through compaction or stabilization, can significantly enhance the performance of geocell-reinforced foundations. In reinforced cases with higher φ, the contribution of the geocell becomes more efficiency-driven rather than capacity-driven, because the soil itself controls the shear failure mechanism.

Table 6. Comparison of change in friction angle.

Angle change	Average bearing capacity increase (%)
30 to 33	31.5
33 to 36	32.8
36 to 39	41.7

3.4. Effect of soil unit weight

The unit weight of soil is a crucial property in geotechnical engineering. It represents the weight of the soil material contained within a given volume. Three different unit weights with values of 15, 16 and 17 were assigned to the soils with different parameters. Fig. 11 shows that raising the soil's unit weight can have a small increase in the bearing capacity of the foundation.

The results highlight that soil friction angle exerts the dominant control on the performance of geocell-reinforced foundations. This suggests that in practice, geocell systems should be optimized primarily through site-specific shear strength improvement and selection of suitable granular infill, while elastic modulus plays a secondary role. The minimal sensitivity to unit weight indicates that for confined and reinforced foundation beds, shear strength parameters (φ, c) dominate load-bearing mechanisms, while density plays only a secondary role. This aligns with the fact that confinement suppresses the effect of self-weight on failure surface formation.

4. Conclusions

This study investigated the influence of three key soil strength parameters, elastic modulus, internal friction angle, and unit weight, on the bearing capacity and settlement performance of geocell-reinforced foundation beds. A total of 48 three-dimensional numerical simulations were conducted in ABAQUS, using a validated FE model benchmarked against Hegde and Sitharam [8]. The results lead to the following conclusions:

- Geocell reinforcement significantly enhances bearing capacity, especially in weak soils where the confinement effect compensates for insufficient stiffness. The bearing capacity ratio (BCR) ranged from 1.65 to 2.26, confirming the strong contribution of lateral confinement and improved shear mobilization. As soil strength increased, the relative improvement

declined, but reinforcement effectiveness remained consistent across all parameter combinations.

- All three soil parameters, elastic modulus, friction angle, and unit weight, positively contributed to bearing capacity and settlement reduction. However, their influence was not equal. The internal friction angle showed the strongest effect: a 3° increase raised bearing capacity by up to 45%, underscoring the central role of shear resistance in geocell–soil interaction.
- The elastic modulus had a moderate effect on bearing capacity. Increasing E by 5 MPa produced average improvements of 0.46% in reinforced and 1.03% in unreinforced soils. However, as friction angle increased, the influence of elastic modulus diminished, indicating that stiffness affects deformation more than ultimate shear-controlled failure.
- Unit weight had the least influence among the studied parameters. The small improvements observed indicate that in confined reinforced beds, strength parameters (φ, E) play a far more dominant role than density in governing load-carrying behavior.
- Based on the comparative assessment, the internal friction angle is the most influential parameter for enhancing the performance of geocell-reinforced foundations. Higher φ not only raises shear strength but also increases the efficiency of geocell confinement, creating a stiffer composite zone and improved stress redistribution.

Overall, the study confirms that geocell reinforcement provides a highly effective and practical solution for improving the bearing capacity of shallow foundations, particularly in weak or lightly compacted soils.

The validated numerical model offers a reliable framework for predicting the behavior of reinforced foundations under variable soil conditions.

Future work should incorporate more advanced constitutive models (e.g., generalized plasticity or state-dependent formulations), evaluate cyclic or dynamic loading, and consider the explicit influence of geocell geometry and material stiffness to improve field-scale applicability and design optimization.

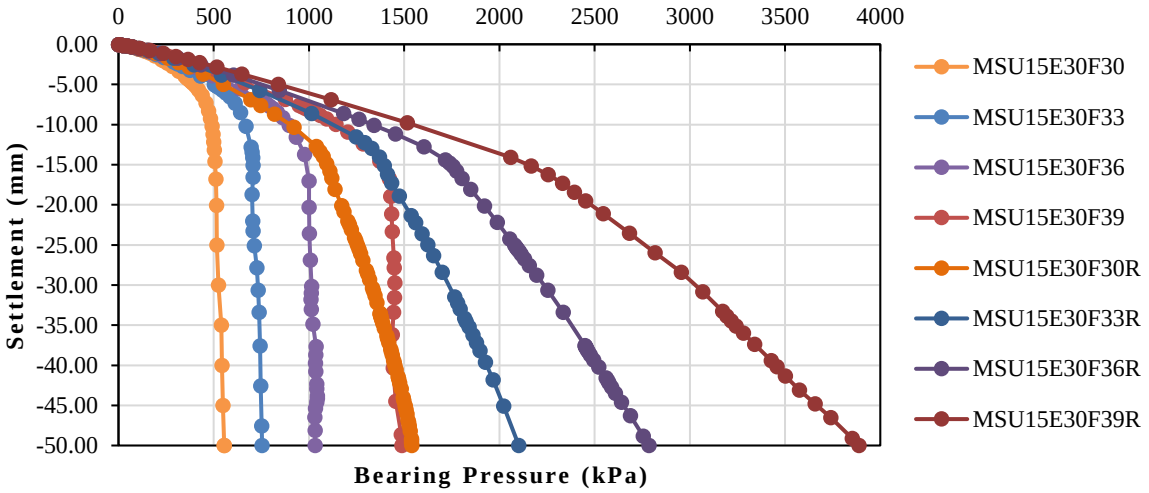

Fig. 11. Effect of unit weight on settlement.

Statements & Declarations

Author contributions

Mohammad Javad Hosseinzadeh: Investigation, Formal analysis, Data curation, Software, Writing - Original Draft.

Mohammad Oliaei: Project administration, Supervision, Resources, Writing - Review & Editing.

Funding

The authors received no financial support for the research, authorship, and/or publication of this article.

Data availability

The data presented in this study will be available on interested request from the corresponding author.

Declarations

The authors declare no conflict of interest.

References

[1] Sitharam, T. G., Hegde, A. Design and construction of geocell foundation to support the embankment on settled red mud. Geotextiles and Geomembranes, 2013; 41: 55–63. doi:10.1016/j.geotexmem.2013.08.005.

[2] Ghanizadeh, A. R., Ghaderi, F., Tavassoti, P. Numerical investigation of the performance of geocell-reinforced granular base in inverted pavement systems using nonlinear finite element modeling. Canadian Journal of Civil Engineering, 2022; 50: 395–407. doi:10.1139/cjce-2022-0282.

[3] Banerjee, S., Manna, B., Shahu, J. T. Experimental investigation of the geometry of geocell on the performance of flexible pavement under repeated loading. Geotextiles and Geomembranes, 2024; 52: 654–670. doi:10.1016/j.geotexmem.2024.03.007.

[4] Pokharel, S. K., Han, J., Leshchinsky, D., Parsons, R. L., Halahmi, I. Investigation of factors influencing behavior of single geocell-reinforced bases under static loading. Geotextiles and Geomembranes, 2010; 28: 570–578. doi:10.1016/j.geotexmem.2010.06.002.

[5] Dash, S., Rajagopal, K., Krishnaswamy, N. Performance of different geosynthetic reinforcement materials in sand foundations. Geosynthetics International, 2004; 11: 35–42. doi:10.1680/gein.2004.11.1.35.

[6] Dash, S. K., Krishnaswamy, N. R., Rajagopal, K. Bearing capacity of strip footings supported on geocell-reinforced sand. Geotextiles and Geomembranes, 2001; 19: 235–256. doi:10.1016/S0266-1144(01)00006-1.

[7] Sireesh, S., Sitharam, T. G., Dash, S. K. Bearing capacity of circular footing on geocell–sand mattress overlying clay bed with void. Geotextiles and Geomembranes, 2009; 27: 89–98. doi:10.1016/j.geotexmem.2008.09.005.

[8] Hegde, A., Sitharam, T. G. 3-Dimensional numerical modelling of geocell reinforced sand beds. Geotextiles and Geomembranes, 2015; 43: 171–181. doi:10.1016/j.geotexmem.2014.11.009.

[9] Mehdipour, I., Ghazavi, M., Moayed, R. Z. Numerical study on stability analysis of geocell reinforced slopes by considering the bending effect. Geotextiles and Geomembranes, 2013; 37: 23–34. doi:10.1016/j.geotexmem.2013.01.001.

[10] Heidarzadeh, H. Evaluation of modified Cam-Clay constitutive model in FLAC and its development by FISH programming. European Journal of Environmental and Civil Engineering, 2021; 25: 226–244. doi:10.1080/19648189.2018.1521752.

[11] Heidarzadeh, H., Oliaei, M. An Efficient Generalized Plasticity Constitutive Model with Minimal Complexity and Required Parameters. KSCE Journal of Civil Engineering, 2018; 22: 1109–1120. doi:10.1007/s12205-017-1037-4.

[12] Heidarzadeh, H., Oliaei, M., Komakpanah, A. A Developed Constitutive Model for Sand and Clay under Monotonic and Cyclic Loadings. International Journal of Geomechanics, 2023; 23: 04023133. doi:10.1061/IJGNAI.GMENG-8334.

[13] Heidarzadeh, H., Kamgar, R. Necessity of applying the concept of the steady state on the numerical analyses of excavation issues: laboratory, field and numerical investigations. Geomechanics and Geoengineering, 2022; 17: 413–425. doi:10.1080/17486025.2020.1755466.

[14] Hegde, A., Shivdev, S., Sitharam, T. Numerical simulation of geocell reinforced foundation beds: a comparative study using PLAXIS 3D and FLAC 3D. In: Indian geotechnical conference, IGC; 2016 Dec 1–2; Chennai, India. p.

[15] Kouzegaran, S., Oliaei, M. Numerical Analysis of the Cellular Geosynthetics Performance in Unpaved Roads and Influencing Factors. Transportation Infrastructure Geotechnology, 2025; 12: 108. doi:10.1007/s40515-024-00500-9.

[16] Oliaei, M., Kouzegaran, S. Efficiency of cellular geosynthetics for foundation reinforcement. Geotextiles and Geomembranes, 2017; 45: 11–22. doi:10.1016/j.geotexmem.2016.11.001.

[17] Song, F., Liu, H., Ma, L., Hu, H. Numerical analysis of geocell-reinforced retaining wall failure modes. Geotextiles and Geomembranes, 2018; 46: 284–296. doi:10.1016/j.geotexmem.2018.01.004.

[18] Ari, A., Misir, G. Three-dimensional numerical analysis of geocell reinforced shell foundations. Geotextiles and Geomembranes, 2021; 49: 963–975. doi:10.1016/j.geotexmem.2021.01.006.

[19] Juneja, G., Sharma, R. K. Numerical investigation of square footing positioned on geocell reinforced sand by using abaqus software. Civil and Environmental Engineering Reports, 2022; 32: 154–173. doi:10.2478/ceer-2022-0024.

[20] Evirgen, B., Kara, H. O., Ucun, M. S., Gültekin, A. A., Tos, M., Öztürk, V. The effect of the geometrical properties of geocell reinforcements between a two-layered road structure under overload conditions. Case Studies in Construction Materials, 2024; 20: e02793. doi:10.1016/j.cscm.2023.e02793.